# Multi-species detection using Infrared Multi-mode Absorption Spectroscopy

A thesis submitted for the degree of Doctor of Philosophy

**Henry Northern**


Worcester College, University of Oxford

Michaelmas Term 2013

# Multi-species detection using Infrared Multi-mode Absorption Spectroscopy

Henry Northern, Worcester College

A thesis submitted in partial fulfilment of the requirement for the degree of Doctor of Philosophy of the University of Oxford

Michaelmas Term, 2013

## *Abstract*

This thesis reports work extending the scope of a recently developed gas sensing technique, multi-mode absorption spectroscopy (MUMAS). The ability of MUMAS to simultaneously detect multiple species from a mixture is demonstrated for the first time. The technique is subsequently extended to mid-infrared wavelengths, realising large gains in sensitivity.

A solid-state, multi-mode laser has been developed to provide a high-performance comb source for use with MUMAS. This in-house constructed, diode-pumped, Er/Yb:glass laser operates on 10 longitudinal modes, separated by 18 GHz and centred close to 1565 nm. The extensive development and prototyping work leading to this final laser design is described.

Multi-species detection with MUMAS is reported for the first time, thus demonstrating the ability of this technique to perform multi-gas sensing using a single laser and simple detection scheme. The previously described Er/Yb multi-mode laser was used to record MUMAS signals from a sample containing CO, $C_2H_2$, and $N_2O$. The components of the mixture were detected simultaneously by identifying multiple transitions in each of the species. Temperature- and pressure-dependent modelled spectral fits to the data were used to determine the partial pressures of each species in the mixture with an uncertainty better than $\pm 2\%$.

Multi-mode radiation has been successfully generated at 3.3 $\mu$m using quasi phase matched difference frequency generation (QPM-DFG). A mid-infrared laser comb was produced by optically mixing the near-infrared, multi-mode comb produced by the previously developed Er/Yb:glass laser with the single-mode output of a Nd:YAG laser operating at 1064 nm. This multi-frequency laser source was characterised to verify performance, and subsequently used to perform proof-of-principle MUMAS measurements on the strong transitions found in this spectral region. Spectra were recorded of $NH_3$ and $CH_4$ both individually and as components of a mixture. A minimum detection level for this system was determined to be 4.3 $\mu$bar m$^{-1}$ for $CH_4$, a sensitivity increase of 300 over similar measurements performed in the near-IR.

# *Acknowledgements*

I would like to express my gratitude to the following:

Professor Ewart for providing the opportunity for me to undertake this research, and for his patience, excellent supervision, advice, and support throughout.

Dr. Ben Williams for his assistance, in particular for helpful advice in the analysis of data, and also for his tireless reading of drafts of this thesis.

Dr. Michelle Hamilton for her supervision, advice and guidance during this project.

The EPSRC and the Oxford Physics Department for financial support.

Dr. Grant Ritchie and Professor Gus Hancock for valuable advice, and for the loan of equipment and materials.

Dr. Damien Weidman for sharing his expertise with QCLs, and for use of his laboratories at RAL.

Simon Moulder, Rob Harris and Matthew Newport for assistance in the Clarendon laboratory workshops.

Members of the Ewart group, past and present for help, advice and company.

The residents of Manor Farm, rodent and otherwise for company and friendship. My friends for putting up with my (more than usual) lack of correspondence.

My parents for their support. Finally to Connie for her love and patience.

# Contents

# Chapter 1

# Introduction

The detection and measurement of gas parameters, particularly composition, is of vital importance to the modern world. Atmospheric pollution, and in particular the release of greenhouse gases is the cause of profound global impacts not least anthropogenic climate change [1]. There is therefore a need to not just measure the current levels of pollutants in the atmosphere, but also to monitor processes that release such compounds, for example combustion, to reduce the production of these chemicals.

There are many other situations that require the properties of gases to be measured, or trace amounts of gases to be detected: industrial processes often occur in the gas phase, or involve gaseous feedstocks or products; gas leaks, particularly in the petrochemical industries can have safety implications; the presence of trace components in exhaled breath has potential for medical diagnostics [2–4]. Thus, there is a need to accurately measure the concentration, and in some cases other parameters such as temperature and pressure, of the species that make up the many gases found in these applications.

Many methods are currently in use for gas detection and analysis [3, 5]. In some situations the primary methods are based on sampling for off-line laboratory analysis. This typically results in accurate measurements, with good reliability, however it is

expensive and precludes real-time data. Alternatively, low cost, deployable single-species sensors based on chemical or electrochemical effects can be used. Such devices often present a good method for simple detection requirements, where the concentration of a single species needs to be monitored over a small range (typically, concentration variation of less than a factor of 10).

There is an ever increasing desire to monitor both a wider range of species and more species simultaneously, in applications where real-time monitoring with low cost sensors are useful, such as ensuring compliance with expanding emissions regulations, controlling more complex industrial processes, or detecting atmospheric pollution. When performed with existing chemical and electrochemical sensors this requires a battery of different devices, all with attendant calibration and maintenence requirements, and cost. In addition when used in these complex environments these simple detectors are subject to inaccuracies due to zero-drift, cross-response, and poisoning by non-target molecules.

This has led to the development of optical gas sensing methods that are, in principle, capable of detecting multiple species simultaneously. Optical absorption provides a simple, general method to perform concentration measurements, simplifying the detection of multiple species. In addition, a direct measurement of a molecule's physical properties is performed, providing resilience to drift and a degree of freedom from calibration. Gas sensors based on optical absorption can provide the high-accuracy and specificity of laboratory based analysis, while having the benefits of making real-time measurements performed with an *in-situ* sensor.

The invention of diode lasers in the 1960s, and the subsequent rapid development of these devices for telecommunications has provided a convenient radiation source for these measurements. Tuneable diode laser absorption spectroscopy (TDLAS) has developed into the dominant technique for high precision, *in-situ* gas sensing, and when combined with signal enhancement techniques provides greater sensitivity, selectivity and accuracy

than other optical techniques. However, the limited scanning range inherent to diode lasers typically restricts any particular device to measuring the absorption caused by a single, isolated molecular transition, precluding the detection of multiple species.

Thus, there is a need to develop new optical sensing methods based on improved radiation sources or improved detection schemes to allow optical multi-species detection.

## 1.1 Introduction to MUMAS

Multi-mode absorption spectroscopy (MUMAS) [6–10] is a novel laser spectroscopy technique that combines high spectral resolution with broad spectral coverage. In contrast to conventional laser absorption spectroscopy that utilises single frequency radiation, MUMAS uses a comb of longitudinal modes produced by a short cavity laser. These modes provide an evenly spaced, sharply defined set of frequencies that collectively cover a large bandwidth.

To perform MUMAS, the output of a multi-mode laser is directed through the gas under investigation. The length of the laser cavity is modulated, simultaneously scanning the modes across a frequency corresponding to one mode spacing. Absorption occurs as individual modes come into resonance with gas transitions, leading to a reduction in the total intensity transmitted through the gas sample. The resulting MUMAS spectrum or "fingerprint" contains information about both the probed gas sample and the probing multi-mode laser. To measure the sample's properties a modelled spectrum is fitted to the data. In this way MUMAS allows absorption measurements to be recorded with a single laser across a spectral region much broader than the single mode scanning range of that laser. In contrast to other multi-transition sensing methods such as multiplexed diode laser measurements or broadband spectroscopy, MUMAS provides a simple and direct approach to acquiring high resolution spectral information on multiple transitions

spread over an extended spectral range by using a single laser and a simple detection scheme.

## 1.2 Overview of this thesis

This thesis reports work undertaken to develop the MUMAS technique, with three main aims: to produce a high-quality multi-mode source for use with MUMAS, to use this laser to demonstrate the ability of the MUMAS technique to perform multi-species detection, and to extend the MUMAS technque to longer wavelengths, thereby achieving greater detection sensitivity.

Chapter 2 describes the motivation for developing MUMAS, and the context into which MUMAS fits. It discusses the need for gas sensing, and the use of laser techniques as the means to perform measurement of concentration, composition, pressure and temperature. Multi-transition sensing is introduced as a method for a single sensor to monitor the concentration of multiple species simultaneously, or to precisely measure the temperature of a single species. A selection of spectroscopic methods that may be used to achieve multi-transition sensing are critically reviewed, before MUMAS is introduced as an alternative. Previous published work on MUMAS is discussed allowing the current work to be introduced in context.

Chapter 3 describes the MUMAS technique that forms the basis of all work reported here. The chapter starts by presenting the mechanism by which MUMAS works, before explaining the necessity for modelling the form of MUMAS spectra. The steps required to produce a modelled spectrum are then described, firstly at a conceptual level before then describing the considerations that need to be accounted for in developing computer code to carry out this simulation. Finally, the properties required of a multi-mode laser source for use in MUMAS are discussed, and the effect of these properties on the form of

a MUMAS spectrum are considered.

The process of developing an improved multi-mode laser for use with MUMAS is described in Chapter 4. Firstly, the reasons for developing this laser are discussed, and the performance requirements identified. The extensive development and prototyping work undertaken to produce a laser optimised for use for near-infrared MUMAS is described in terms of improving several key properties of the laser. Lastly, a final design is introduced and its design and performance described.

Chapter 5 reports the first demonstration of multi-species detection using MUMAS. The Er/Yb:glass micro-cavity laser, developed in work reported in the previous chapter, is used to detect three molecular species from within a mixture composed of these gases and additional non-absorbing components. The apparatus and procedure used to perform this gas sensing is described, and the fitting procedure that allows the MUMAS model to be used to make quantitative measurements of gas concentration is explained.

In Chapter 6 the first application of MUMAS to mid-infrared wavelengths is reported. This chapter starts by discussing the attraction of this spectral region for high sensitivity spectroscopy before moving on to review the mid-IR radiation sources currently used for spectroscopy. The design, construction and characterisation of a mid-IR multi-mode radiation source is then described, before this system is used to perform proof-of-principle absorption studies.

The future direction of the MUMAS project is discussed in chapter 7. Firstly, the potential for improvements to the detection limit of the current results are discussed. A comparison is made between the sensitivity achieved with the experimental near-IR spectrometer, reported in Chapter 5 and the experimental mid-IR spectrometer reported in Chapter 6. This suggests where the future focus of the technique should lie. The changes that would be required to extend the technique to atmospheric pressure sensing are also discussed.

# Chapter 2

# Background

## 2.1 Introduction

This chapter explains the motivation for developing MUMAS and its place in the context of alternative techniques for gas sensing. It starts by looking at why laser techniques are suited to the measurement of concentration, composition, pressure and temperature in a variety of environments and the mechanisms by which these measurements are made, before discussing the benefits of making a simultaneous measurement of multiple molecular transitions. Several spectroscopic methods capable of making such multi-transition measurements are surveyed before the MUMAS technique is introduced. The relative merits of these techniques are briefly discussed. Previous published work on MUMAS is reviewed and the current work introduced in this context.

## 2.2 Optical gas sensing

The detection of gases and measurement of parameters, particularly concentration, has many applications across a wide range of scientific and commercial fields. Early industrial deployment of gas sensors was largely limited to applications related to safety –

monitoring of toxic or flammable gases – and pollution control, particularly in the process and petrochemical industries [3]. This sensing requirement was driven by tightening legislation in these areas, and as such was often seen as an unwelcome but unavoidable cost [5]. However, as the sophistication and complexity of these industrial processes has increased there has been a growing use of gas analysis as a vital tool in process control and quality assurance, through concentration measurements of feed stocks, key intermediate species and products, which may be varying on short timescales [2]. There are also many non-industrial uses for gas monitoring, such as atmospheric science, where variations in the concentration of trace species may shed light on fundamental reactions pathways [11, 12]; environmental monitoring, where knowledge of the concentration and spatial profiles of pollutants is vital for regulation and control of harmful emissions [13]; and even medical diagnostics, where trace species such as urea, acetone and hydrocarbons present in exhaled breath may be linked to conditions as diverse as *h.pylori* infection, diabetes and lung cancer [4, 14–16].

Traditionally, much quantitative detection of gases was carried out through sampling and later laboratory analysis using techniques such as gas chromatography or mass spectroscopy. These methods require expensive equipment and the off-line nature of the analysis precludes obtaining real-time data. Alternatively, low-cost, robust sensors such as pellistors, or gas sensors based on electro-chemical or semiconductor devices could be deployed for the detection of individual species. Gas detection using these sensors is characterised by the variety of different technologies required to detect different species [5]. While there are some cases that these sensors are particularly well suited to – for example pellistors are well suited to detection of flammable gases close to the lower explosive limit – in general these devices have several drawbacks. Pellistors and semiconductor sensors can both suffer from zero-drift issues and may cross-respond to non-target molecules. Electrochemical sensors typically show greater sensitivity and selectivity, however, have

limited lifetimes. All of these types of detectors require particular operating conditions and may become poisoned by exposure to particular non-target species, causing permanent damage, or be inhibited by exposure to high levels of target molecules [3].

In contrast, optical sensors based on absorption effects provide a direct method to perform quantitative gas detection. Laser absorption spectroscopy allows targeting of individual molecular transitions lending the technique high selectivity and a well designed sensor based on this technology can exhibit zero response to non-targeted species. Optical sensors can perform *in-situ* measurements with fast response times allowing true on-line detection of rapidly changing properties (often on the order of milliseconds [17]). The non-invasive and stand-off nature of optical absorption measurements permits application to harsh and dangerous environments [18], and to systems – such as flames – that may be perturbed by the physical imposition of a sensor or sampling tube [19, 20]. The sensing method utilised in these sensors makes a direct measurement of molecular properties and as such is resistant to drift; the ability to measure light intensity incident and transmitted by a sample allows for self-referencing leading to the possibility of calibration-free sensing.

These optical sensors fill an important gap between expensive and slow sampling with off-line analysis using laboratory equipment, and *in-situ* measurement with low cost sensors that may suffer from inferior performance and restrictions on operating conditions. In addition, the universal nature of the detection method employed in optical absorption sensors opens the possibility of extending the sensor to multi-species detection without the integration of multiple discrete sensors, each based on disparate technologies and requiring individual calibration procedures.

## 2.3 Laser absorption spectroscopy

Laser absorption spectroscopy is a widely used technique with very general applicability. This technique measures the frequency-dependent attenuation of electro-magnetic radiation passed through a medium, and from this infers the properties of that medium. For the simplified case of a hypothetical molecule having two isolated stationary states this resonant absorption arises from the electric field of the radiation interacting with a dipole moment of the molecule as it oscillates at the same frequency as the radiation field, resulting in the removal of a photon from the light field and the coupled excitation of a single molecule from the lower to upper state.

In practice, a monochromatic beam of light from a laser operating on a single longitudinal mode is passed through a medium – typically a sample in a gas cell – with the incident and transmitted beam intensity being monitored (Figure 2.1). The frequency of the radiation is scanned over a region of interest and the consequent transmission signal recorded. The frequency-dependent attenuation of the sample can then be linked to the properties of the medium by the Beer-Lambert law [21]:

$$I(\nu) = I_0(\nu)\, e^{-\sigma(\nu)CL} \tag{2.1}$$

where $I_0(\nu)$ is the incident intensity, $\sigma(\nu)$ the absorption cross-section, $C$ the concentration of absorber and $L$ the pathlength of propagation through the medium. The exponent $(\sigma(\nu)\, C\, L)$ is traditionally referred to as the absorbance.

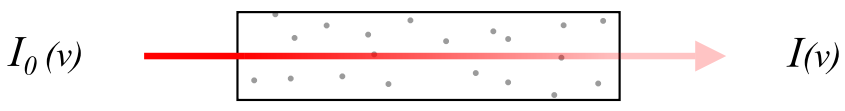


**Figure 2.1:** Schematic diagram of a simple direct absorption measurement.

Real molecules have many energy levels and thus molecular spectra exhibit absorption at many different frequencies – termed absorption lines – corresponding to the many transitions possible. In all but the most simple case of a single isolated transition the cross-section used to determine attenuation therefore must be calculated using the sum of all the frequency dependent probabilities for transitions close to the laser frequency.

### 2.3.1 Line Strength

The strength of a given absorption line can be characterised by its integrated linestrength, $S$:

$$S = \int_0^\infty \sigma(\nu)\, d\nu\,. \tag{2.2}$$

For the transition between two isolated molecular energy states, $i$ and $j$, with equal degeneracy, this line strength is determined by the initial population densities of the states ($N_i$ and $N_j$), and the transition probability [22, 23]. This can be expressed:

$$S_{ij} = \frac{h\nu}{c} B_{ij} (N_j - N_i) \tag{2.3}$$

where $B_{ij}$ is the Einstein coefficient of stimulated emission, given by:

$$B_{ij} = \left[\frac{8\pi^3}{(4\pi\epsilon_0)3h^2}\right] |\mu_{ij}|^2\,, \tag{2.4}$$

and $\epsilon_0$ is the permittivity of free space, $h$ the Planck constant. The transition dipole moment $\mu_{ij}$ describes the quantum mechanical probability of a particular transition occurring and is itself given by:

$$\mu_{if} = \int \psi_i^* \vec{\mu}\, \psi_f\, d\tau\,. \tag{2.5}$$

Assuming thermal equilibrium, the initial population densities, $N_i$ and $N_j$, are determined by the Boltzmann distribution. The absolute number of molecules in state $i$, at temperature $T$ is given by

$$N_i = \frac{N}{Q_i}(2J_i + 1)e^{-E_i/k_BT} \tag{2.6}$$

where $J$ is the rotational quantum number of state $i$ and $k_B$ the Boltzmann constant. The total population $N$ is divided by the partition function $Q_i$ to give the absolute population in state $i$. The partition function is defined:

$$Q_i = \sum_i (2J_i + 1)e^{-E_i/k_BT}\,. \tag{2.7}$$

### 2.3.2 Line broadening

Molecular absorption lines exhibit a finite spectral width, a result of not just instrumental effects but also fundamental physical properties of the medium. Several different processes within the medium lead to the broadening of transitions observed in laser absorption spectroscopy but these can be identified as belonging to two distinct classes, resulting in two different characteristic lineshapes. Mechanisms that cause all molecules within the sample to affect the linewidth in the same way are referred to as *homogeneous* and result in a Lorentzian profile, those that cause an effect that varies from one molecule to another are described as *inhomogeneous* and result in a Gaussian profile [22].

*Natural broadening* provides a Lorentzian contribution to the lineshape of even a single molecule at rest. This effect arises from the Uncertainty Principle, which defines a reciprocal relationship between lifetime and energy uncertainty for a state, and results in a broadening of the transition energy due to the finite lifetime of energy levels within a molecule. In the case of absorption spectroscopy, the principal decay mechanism is the

spontaneous emission of a photon from the excited state, and so the linewidth is related to the Einstein $A$-coefficient, and thus has a $\nu^3$ dependence. This means that the natural linewidth of transitions found in the visible and UV is much greater than those in the infrared region; the contribution of natural broadening to the overall linewidth is usually only observed for infra-red spectroscopy when other mechanisms are removed, such as by employing a Doppler-free method at low pressure.

The largest contribution to the linewidth in ro-vibrational spectra of low pressure gases is usually caused by *Doppler broadening*. This inhomogeneous effect results in a Gaussian line profile and arises due to the thermal motion of individual molecules within a sample. A moving body experiences radiation of a different frequency than that measured in a stationary reference frame, an effect known as *Doppler-shift*, and hence in a sample containing many molecules moving in random directions with a distribution of speeds, radiation is absorbed over a finite frequency range. The frequency of radiation absorbed by a molecule moving with velocity, $v_a$ – defined as positive towards the radiation source – is related to the resonance transition frequency, $\nu_0$ by

$$\nu_a = \frac{\nu_0}{1 - \frac{v_a}{c}} \,. \tag{2.8}$$

Applying a Maxwell-Boltzmann distribution to the molecular velocities results in the broadening of a spectral line to a full width at half maximum given by [22]

$$\Delta\nu_{Dopp} = \frac{\nu}{c}\left(\frac{8k_B T \ln 2}{m}\right)^{\frac{1}{2}} \tag{2.9}$$

where $k_B$ is Boltzmann's constant, $T$ the sample temperature and $m$ the mass of the particles. Thus the Doppler broadened width of a transition is proportional to the square root of temperature. Doppler broadening is an inhomogeneous effect and results in a

Gaussian line shape of the form

$$g_G(\nu - \nu_0) = \frac{c}{\nu_0}\sqrt{\frac{m}{2\pi k_B T}}\ \exp\left(\frac{-4\ln 2\,(\nu-\nu_0)^2}{\Delta\nu_{dopp}^2}\right). \tag{2.10}$$

At higher pressures another broadening mechanism provides a contribution to the overall lineshape. *Pressure broadening* arises from collisions between molecules which can lead to perturbation of the molecular wavefunction. One way that this can lead to spectral broadening is via phase changing collisions, where the presence of a nearby molecule's electric field causes phase jumps in the oscillation of the molecular dipole, thus affecting its interaction with a light field. Pressure broadening is a homogeneous effect and results in a Lorentzian line profile of the form

$$g_L(\nu - \nu_0) = \frac{1}{2\pi}\left[\frac{\Delta\nu_L}{(\nu-\nu_0)^2 + \left(\frac{\Delta\nu_L}{2}\right)}\right] \tag{2.11}$$

where $\Delta\nu_L$ is the broadened width that results from a combination of all lifetime effects (i.e. natural and collisional induced processes):

$$\Delta\nu_L = A_{ij} + \frac{2}{\tau_{collision}} \tag{2.12}$$

and the mean time between phase changing collisions, $\tau_{collision}$, is given by kinetic theory as

$$\frac{1}{\tau_{collision}} = \frac{\sigma_Q P}{\sqrt{\pi\mu k_B T/8}} \tag{2.13}$$

where $\sigma_Q$ is the collisional cross-section, and $\mu$ the reduced mass. The pressure broadened linewidth is thus proportional to pressure and inversely proportional to temperature.

At atmospheric pressures, the dominant contribution to linewidth is due to these collisional effects, while at pressures below a few mbar, almost all broadening is due to

Doppler effects. At intermediate pressures both effects are significant and the observed lineshape is a combination of both Doppler and collisional effects. This profile can be described by the Voigt function, a convolution between Gaussian and Lorentzian lineshapes, which is given by:

$$g_V = \frac{2y}{\Delta\nu_G \pi}\sqrt{\frac{\ln 2}{\pi}} \int_{-\infty}^{\infty} \frac{e^{t^2}}{y^2 + (x-t)^2}\, dt\,. \tag{2.14}$$

Within this equation,

$$x = \sqrt{\ln 2}\ \frac{2\,(\nu - \nu_0)}{\Delta\nu_G} \qquad \text{and} \qquad y = \sqrt{\ln 2}\left(\frac{\Delta\nu_L}{\Delta\nu_G}\right)$$

where $\Delta\nu_L$ and $\Delta\nu_G$ represent the full width at half maximum of the Lorentzian and Gaussian components respectively. Generation of Voigt profiles for spectral modelling is usually done with the use of an approximation such as that discussed in Section 3.3.4.

### 2.3.3 Tuneable diode laser absorption spectroscopy

Diode lasers were first demonstrated in the 1960s [24] and it was not long before these devices were employed as sources of monochromatic light for spectroscopy. Much development work has since been directed towards these devices, principally for use in telecommunications in the near-infrared region (especially around 1.5 $\mu$m) where both the optimum transmission window for silica optical fibres and the operational wavelength of erbium fibre-amplifiers are found. Consequently compact, robust devices that operate at room temperature and produce stable, narrow linewidth, single-mode* radiation are now available as commodity items.

The near-infrared region is also very attractive for spectroscopy due to the density of

*In this thesis the terms "single-mode" and "multi-mode" typically refer to the number of longitudinal cavity modes a laser system operates on – *i.e.* a single-mode laser emits single colour, narrow bandwidth output. The transverse properties are not prescribed.

overtone and combination transitions found here arising from many common molecules, and as such tuneable diode laser absorption spectroscopy (TDLAS) is now a mature technique and increasingly being deployed in gas sensors [5]. TDLAS usually scans the output from a narrow linewidth, single-mode diode laser over an isolated absorption line of the species under investigation. To achieve high selectivity, analysis is typically carried out at reduced pressure and a multi-pass arrangement is often used to increase absorption. TDLAS is a very general technique, the main requirement being that the molecule should have an infrared line-spectrum which is resolvable at the Doppler limit; in practice this includes most molecules with 5 or fewer atoms, and many others [5].

TDLAS allows specific and selective detection of one species free from interferences from contaminating species in the sample, with sensitivity good enough for trace gas monitoring. Unlike some chemical sensors it is not susceptible to poisoning and provides a direct measurement of concentration [5]. As well as being used for species detection, TDLAS can provide data on spectral lineshapes. Thermodynamic parameters such as temperature, pressure and mass flow can be extracted from these lineshapes through the effects of Doppler broadening, pressure broadening and Doppler frequency shift, respectively [25].

TDLAS can be performed in a direct absorption configuration, where the intensity of the monochromatic laser beam is recorded both before and after passing through a sample, and an absorption signal calculated as the laser is swept in frequency. However, it is more common to employ a modulation-based detection scheme such as wavelength modulation spectroscopy (WMS). In WMS the laser output frequency is swept across a transition in the same manner, however, an additional high frequency wavelength modulation (kHz) is imposed on the laser output. A lock-in amplifier is then used to detect the component of the amplitude modulation oscillating at the same high frequency. This amplitude modulation is a result of laser radiation encountering a molecular absorption transition,

and so provides a measure of the absorption strength.

Modulation spectroscopy takes advantage of a key property of diode lasers – the ease with which they can be modulated at high frequencies through injection current modulation – and uses this to bring two main benefits over direct absorption measurements. Firstly, in contrast to direct absorption where the signal is measured as a small change on a large signal (typically a change of $10^{-2}$ — $10^{-5}$), WMS produces a zero-baseline signal, reducing the potential for measurement drift. Secondly, modulation allows the signal to be recorded at a frequency at which laser noise is significantly reduced, thus improving one of the two main limitations to sensitivity [5, 21]. As a result, sensitivity improvements of 10 — 100 times can be achieved over an equivalent direct absorption experiment, allowing detection of absorption features on the $10^{-5}$ — $10^{-6}$ scale in the best cases. Instruments based on modulation spectroscopy have been reported with minimum detection limits of parts per trillion by volume (pptv) [26, 27].

The other main limitation to the sensitivity of TDLAS carried out in the NIR is linked to the strength of the transitions found in this region. The absorption lines measured by TDLAS in the near-IR arise due to overtone or combinational ro-vibrational transitions, and thus typically have line strengths $10^2$ — $10^5$ times weaker that the fundamental vibrational transitions found in the mid-IR region, limiting the magnitude of the absorption signals recorded. One method to circumvent this limitation is to change the wavelength of the probe laser to match that of these stronger, fundamental transitions. This can be done by shifting the wavelength of a source with a non-linear optical technique such as difference frequency generation, or by generating radiation directly in the mid-IR with sources such as Pb-salt diode lasers or modern quantum well sources such as quantum cascade lasers (QCLs). Gas sensing in the mid-IR region is further discussed in Chapter 6.

Another method of increasing absorption signal is by increasing the optical density of

the gas sample, typically by increasing the pathlength that the measurement is carried out over. This can be achieved either with a multi-pass cell, which typically can achieve a pathlength of 10 — 100 m, or more dramatic increase can be made with an optical cavity, which can achieve pathlengths up to several kilometers in a small table-top device.

Cavity enhanced spectroscopy techniques are well suited to sensitive trace gas detection [28]. Several different schemes have been proposed and explored, with cavity ring down spectroscopy (CRDS) and cavity enhanced absorption spectroscopy (CEAS, also known as integrated cavity output spectroscopy, ICOS) both receiving much attention. These techniques monitor the intra-cavity absorption of radiation by a target molecule but the manner in which this is done varies. CRDS injects light into an optical cavity – ideally exciting a single cavity mode – and then monitors the decay in intensity of this radiation in the time domain. The decay constant then provides the measure of absorption. In this way it avoids the difficulty of detecting a small change on a large signal inherent to other absorption techniques and thus achieves great sensitivity.

In contrast, CEAS directly measures the total, time integrated intensity of radiation transmitted by a cavity. To do this the cavity is irradiated continuously leading to sequential excitation of many cavity modes. To prevent the imposition of cavity fringe spectrum on the molecular absorption spectrum, the cavity modes must be "blurred out" leaving a flat transmission spectrum as a function of laser wavelength. This can be experimentally achieved by partially mis-aligning the cavity or by rapidly changing the cavity length through mechanical vibrations or some other means. CEAS provides a large increase in sensitivity over simple absorption spectroscopy but typically does not achieve the same extremes of sensitivity as CRDS. The advantage of CEAS, however, lies in the relative simplicity of the experimental set-up, the less demanding speed of the associated electronics and the greater resilience to mechanical vibrations. As such, when combined with compact radiation sources such as diode lasers it has the potential for use

in robust and compact high-sensitivity trace gas sensors.

## 2.4 Multi-transition detection

Tuneable diode laser spectroscopy has advanced greatly in the past few decades and for many applications it is now seen as the "gold standard" for the selective detection of single gaseous species. However, in many cases the simultaneous detection of multiple absorption transitions is required, either for the measurement of the concentrations of multiple gases, or for multi-parameter measurements of a single species. This is more difficult to achieve with TDLAS due to the short continuous tuning range inherent to most diode lasers.

The ability to simultaneously monitor the concentrations of multiple species is particularly sought after, and is applicable to many fields. Multi-species detection is important for environmental monitoring, where often it is necessary to monitor the evolution of the concentration of multiple trace species to form a complete understanding of atmospheric pollution [29, 30]. There are applications to combustion, where the monitoring of the exhaust gases can provide insight into the physical processes occurring and help elucidate the many chemical pathways operating [18, 19, 31, 32]. Laser diagnostics can also be applied to the control of combustion processes [33], in particular the monitoring of CO and $CO_2$ concentration in exhaust gases can allow closed-loop control to maximise completeness of combustion, leading to gains in efficiency [34, 35]. Spectroscopic breath analysis is a new frontier for medical diagnostics and the concentrations of increasing numbers of trace species in exhaled breath are being recognised as markers for particular diseases. Therefore there is a need for instruments able to perform rapid, highly-sensitive, multi-species analysis of breath in a clinical setting [36].

Multi-transition absorption spectroscopy is also useful for temperature measurement.

Laser-based thermometry is a valuable technique for many applications due its ability to remotely measure the temperature – as experienced by the molecules themselves – in a chosen probe volume, which may be positioned in a harsh or inaccessible environment. Many methods have been developed to perform these measurements utilising different physical mechanisms [37–39], however, a very simple procedure is to measure the intensity of two transitions with absorption spectroscopy [40, 41]. The strength of these lines is determined by the population of their ground state, amongst other factors, and it can be shown that for a given pair of lines the intensity ratio, $R$, is purely a function of temperature (see equation 2.15) [29].

$$R = \frac{S_1(T_{ref}).g(\nu - \nu_1)}{S_2(T_{ref}).g(\nu - \nu_2)} \exp\left[-\left(\frac{1}{k_B}\right)(E_1'' - E_2'')\left(\frac{1}{T} - \frac{1}{T_{ref}}\right)\right]. \tag{2.15}$$

The temperature sensitivity and precision of such a measurement is dependent on the energy difference between the ground states. Therefore, careful choice of the pair of transitions allows this "thermometer" to be tuned to provide maximal sensitivity in a chosen temperature range, and the relative nature of this measurement provides some immunity to fluctuations in laser power or sample concentration. Thus, population measurements can provide a much higher precision than is possible by measuring the lineshape of a single transition. This method for remote, non-invasive thermometry has particular application to combustion processes where temperature is often the most important parameter and precise, time-resolved measurement is desired for understanding of chemical pathways and optimisation of efficiency [31].

It might be hoped that these multi-transition measurements could be carried out with diode lasers, however, these devices suffer from intrinsic limitations to their continuous scanning range due to their gain properties and structure, and also as a result of wavelength selective elements incorporated into their design. This drawback particularly badly effects

the types of diode laser most commonly used for single-transition measurement – DFB and DBR lasers. These lasers achieve single mode operation through holographic imprinting of a Bragg grating (DFB) or a Bragg reflector (DBR) into the active medium. This structure provides a spectral output characterised by a single, narrow frequency but limits the tuning range due to the small change in grating spacing that can be achieved through methods such as temperature modulation. Therefore there is a need for alternative detection methods based either on novel laser sources or different forms of spectroscopy. A selection of the currently existing methods is reviewed below, before a new technique that forms the basis of this thesis – multi-mode absorption spectroscopy – is introduced.

## 2.5 Selected multi-species detection techniques

### 2.5.1 Multi-transition TDLAS

The TDLAS technique can be extended to allow a broader spectral range to be probed. The simplest method to achieve this is to replace the DFB or DBR laser with a device that has a greater continuous tuning range, such as an external cavity diode laser (EC-DL) or a vertical cavity surface emitting laser (VCSEL). These devices differ from the other designs in the mechanism by which single frequency operation is achieved. EC-DLs use a diffraction grating as the wavelength selective element; this is placed outside the active medium and forms an external resonator (see Figure 2.2) [42]. Frequency tuning is effected through grating (or mirror) rotation, and a continuous scanning range of $\sim$100 GHz is possible. While EC-DLs often have good spectral properties for high-resolution spectroscopy they still exhibit a limited tuning range and their non-monolithic structure makes them more expensive to construct and more sensitive to vibration, thereby making them less attractive for deployment in a gas sensor.

The structure of VCSEL differs fundamentally from that of other diode lasers. Con-

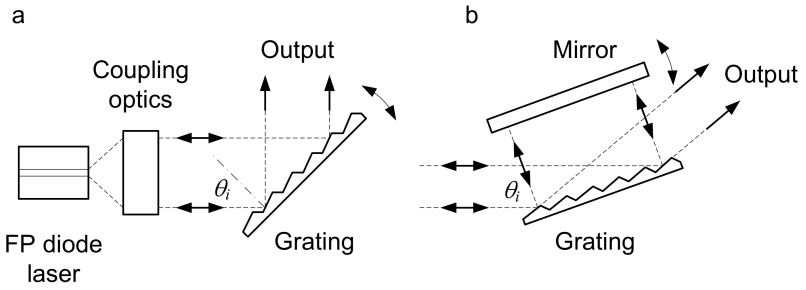


**Figure 2.2:** The a diagram of the two common EC-DL structures. **(a)** Littrow configuration [43]. **(b)** Littman configuration [44]. The laser cavity is formed between one face of the gain medium and the adjustable mirror or grating itself. Wavelength selection is achieved through reflection of the first-order diffracted light back into the cavity. Diagram from [45].

ventional diode laser emit radiation from the edge of their active layer, along the axis of a cavity formed in the plane of this layer. In contrast, VCSELs emit light from a surface perpendicular to this plane. A very short cavity is formed (length on the order of 1 $\mu$m) by constructing multi-layer dielectric coated reflectors above and below the active layer; the free spectral range is correspondingly large, often larger than the gain bandwidth of the laser, removing the need for additional wavelength selective elements. This allows wider continuous tuning ranges (typically 200 GHz), however VCSELs often suffer from low output powers and have only been developed in a few restricted wavelength ranges, which until recently were restricted to wavelengths below 1 $\mu$m. [46].

An alternative to tuning a single laser over a greater range is to simultaneously record spectra from multiple lasers, each tuned to the wavelength of a transition of interest. To ensure that these spectra are recorded over the same optical path, it is important to combine all the beams before passing through the sample and then to separate the signals to allow multi-channel detection, processes known a multiplexing and de-multiplexing. There are several possible methods to achieve this; reported

schemes include time-division-multiplexing [30], wavelength-division-multiplexing [40] and frequency-modulation-multiplexing [47]. These methods are particularly applicable to the monitoring of widely separated transitions (see, for example [40]) but require multiple lasers, multiple detectors and potentially expensive multiplex equipment.

More recently new forms of diode lasers have been proposed with the aim of achieving tuning over a much broader range. External cavity devices based on MEMS (microelectromechanical) technology allow for very short cavity lengths and thus mode-hop free tuning over wide spectral regions (up to 50 nm) [48]. Alternative monolithic designs such as modulated Y-branch diodes make use of the Vernier effect between the fringes formed by two gratings to provide a wide tuning range [49, 50]. Yet another design, the digital super-mode distributed Bragg reflector has recently been used for spectroscopy with promising results [51]. Devices such as these are starting to mature due to interest in their application to wavelength division multiplexed telecommunications, and there is hope that these lasers will reach the cost, compactness and performance characteristics of modern DFB lasers.

### 2.5.2 Broadband measurements

One method to achieve a greater spectral coverage is to perform optical measurements with broadband radiation; such measurements circumvent the tunability limitations of diode lasers and allow spectral information to be recorded over a broad spectral region simultaneously. There are many different broadband measurement techniques, using a wide selection of radiation sources, however, these can be classified into two broad classes depending on the detection scheme employed.

Non-dispersive techniques (normally referred to as non-dispersive infrared, NDIR) pass radiation from a broadband source through a sample and monitor the intensity transmitted in two wide spectral windows, selected by filters. One of these windows is

chosen to contain an absorption band of the target molecule (the signal channel), the other is chosen to correspond to a region free from target or interfering absorptions (the reference channel). A measure of target species concentration can then be made from the ratio of the measured intensity in the the active and reference channels. In reality this is a first order approximation as it only holds for small absorbance and if any source output intensity fluctuations affect both detection windows in the same way.

The NDIR technique has one principal advantage over other optical sensing techniques for deployment in a sensor – it may be implemented with extremely simple and mature technology leading to simple, cheap and reliable devices [3]. Incandescent sources, such as microbulbs are typically used, teamed with thermal detectors, and together this combination allows the technique to access the mid-infrared region, providing strong absorptions. However, such sources typically suffer from poor noise characteristics and have very limited electronic modulation frequencies proscribing the use of modulation techniques. The result is cheap robust sensors, capable of long periods of unattended operation, with moderate minimum detection levels – down to the order of parts per million by volume in the best cases. These sensors do not have the ability to perform selective measurements and multi-species detection requires multiple sources and detectors, the wavelengths of each being carefully chosen to avoid cross-response to other targets or interfering molecules, but where this is possible the additional complexity is not prohibitive due to the simplicity of the technique. A widely deployed example is the Li-Cor open path $CO_2/H_2O$ analyser which operates in the 4.2 $\mu$m measurement band [52].

In contrast, dispersive techniques analyse the spectral profile of broadband radiation with some form of wavelength-selective detection equipment. These systems are capable of recording spectrally resolved measurements over a broad wavelength range allowing true multi-species detection, however, this comes at the price of additional complexity

and with it increased bulk and expense. Traditional, large, lab-based spectrophotometers typically use the radiation emitted from a selection of emission lamps and either grating-based monochromators or a dispersive spectrometer coupled to a detector array to record a broadband absorption spectrum. Simpler, more compact versions of these devices have been developed using light sources such as super-luminescent light emitting diodes [53, 54]. These are more suitable for deployment, however the poor spectral brightness inherent to these sources often limits detection sensitivity. Modern coherent broadband sources such as supercontiniuum light sources based on photonic crystal fibre technology have improved this, although at additional expense [55]. The spectral resolution limitations inherent to the dispersion schemes employed in these sensors typically makes them more suitable to monitor broadband absorbers, where their restricted resolution does not overly impair the selectivity of the technique.

### 2.5.3 Correlation spectroscopy

A novel gas detection scheme has recently been developed that achieves wide spectral coverage using a conventional multi-mode diode laser with the aid of temporal correlation methods that utilise the random fluctuations common to such lasers [56, 57]. This technique, named gas correlation spectroscopy (TEGACOS) is similar to the more established optical correlation techniques which use a broadband source (COSPEC) but uses an unstabilised Fabry-Perot multi-mode diode laser. The narrow linewidth of this laser source lends this method some of the sensitivity and selectivity benefits of TDLAS while maintaining the simplicity and robustness of COSPEC.

Gas correlation spectroscopy employs a dual-beam detection scheme whereby the output of a single diode laser is split in two with half directed through a sample of unknown gas and the remainder through a reference cell containing a well characterised sample of the target gas. The diode laser wavelength is tuned across absorption structures

in the target gas by changing the laser temperature or current, and the intensity recorded from both channels simultaneously. In addition the integrated photodiode is monitored and used to calibrate these signals for laser power variations. The recorded signals may then contain gas absorption "imprints", arising from the target or other molecules, as well as fluctuations in intensity caused by optical fringes or laser fluctuations due to mode competition or mode hops. An analysis of the correlation between the two channels allows the discernment of signals that arise from absorptions due to the target molecule from other signals. The ratio between the magnitude of the correlated components of the signals gives the target gas concentration.

This scheme is functional for any combination of gas absorption signals obtained with a diode laser exhibiting arbitrary frequency shifts, intensity variations or mode-hops and was first demonstrated with the A-band $b^1\Sigma_g^+ - X^3\Sigma_g^-$ of molecular oxygen [56]. An AlGaAs Fabry-Perot diode laser emitting multiple longitudinal modes centred around 757 nm and covering ∼2 nm was used to detect 6 oxygen transitions. Concentration measurements of oxygen were performed by comparison to the accurately known concentration in the reference cell. The technique may be extended to the detection of multiple gases through the use of multiple reference samples, each with a dedicated detector and such a system was reported by Lou and co-workers in 2010 [58]. Modulation techniques such as WMS can be used in conjunction with gas correlation spectroscopy to increase the signal-to-noise ratio and thus increase the sensitivity of the technique [59].

Unlike TDLAS, this technique does not provide information on individual absorption lines, in fact a detailed spectral knowledge is not required. The major drawback of this technique is the intrinsic requirement for a reference cell containing the target gas at precisely the same temperature and pressure as the unknown sample. This limits applications to non-dynamic samples with well known thermodynamic parameters. Gas correlation spectroscopy has not been shown to have the high sensitivity of TDLAS,

however, it is a technique that can provide broader spectral coverage while being simpler to implement, with lower requirements on the quality of the equipment required; it is suitable for gas sensing applications that require moderate sensitivity (down to high ppm) but benefit from the robustness and lower equipment costs this technique can provide.

### 2.5.4 Frequency comb spectroscopy

The advent of optical frequency combs (OFCs) generated by femtosecond laser systems in the last few years has provided a new option for multi-transition spectroscopy with much potential. These high precision light sources combine the attractive properties of extremely wide spectral coverage with the very high spectral resolution provided by each comb element. Spectroscopists have been quick to apply this new tool to both precision spectroscopy and to highly-sensitive multi-species detection in the gas phase, and have developed a variety of absorption and detection schemes in an attempt to best employ these new light sources [60–65].

#### Frequency comb generation

Optical frequency comb synthesisers (OFCSs) are based upon mode-locked femtosecond lasers and produce an optical frequency comb through the interference of periodic femtosecond pulses in a temporally coherent pulse train. A mode-locked laser, for example a Kerr-lens-mode-locked Ti:Sapphire laser, emits a periodic train of short pulses. This can be considered to be the result of a pulse circulating within the laser cavity with width $\Delta t_{env}$ and carrier frequency $\omega_c$. The temporal separation of the emitted pulses is then given by the laser cavity round-trip time, $\Delta t_{rep} = 2L_c/v_g$, where $L_c$ is the cavity length and $v_g$ the mean group velocity [66]; this is illustrated in Figure 2.3(a).

A train of identical pulses, separated by a fixed interval, may be obtained from a

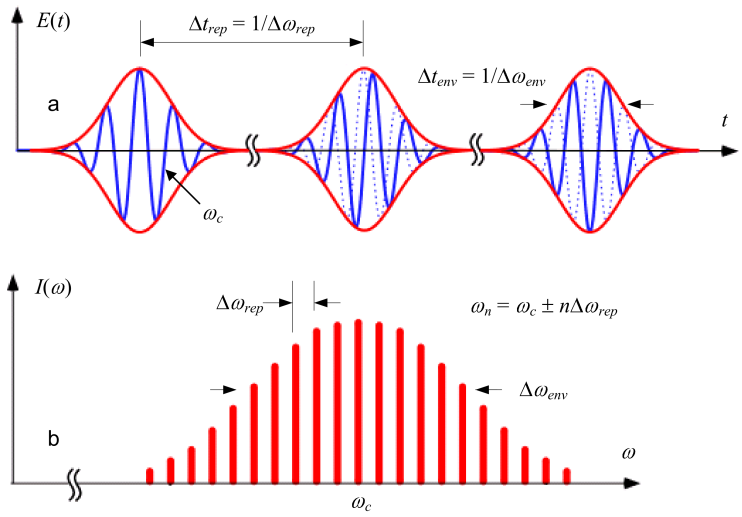


**Figure 2.3:** Optical frequency comb generation. **(a)** The time domain description of a train of extremely short (fs) pulses emitted by a mode-locked femtosecond laser. **(b)** The corresponding frequency domain spectrum consists of a comb of extremely narrow modes. The time and frequency domain descriptions are linked by a Fourier relationship. Diagram from [45].

Fourier series. The electric field $E(t)$ outside the laser may be written as

$$E(t) = Re[A(t)\exp(-i\omega_c t)] \tag{2.16}$$

$$= Re\left[\sum_n A_n \exp(-i(\omega_c + n\Delta\omega_{rep}))\right] \tag{2.17}$$

where $A_n$ are the Fourier components of $A(t)$. The frequency spectrum of the pulses thus corresponds to a comb of regularly spaced frequencies with separation equal to the repetition frequency $\Delta\omega_{rep} = 1/\Delta t_{rep}$. Figure 2.3(b) shows the frequency spectrum of the pulse train in (a). The frequency of each mode can be written

$$\omega_n = \omega_c \pm n\Delta\omega_{rep} \tag{2.18}$$

with $n$ being a large integer, the magnitude of which is determined by the comb bandwidth. The repetition frequency can be determined with high accuracy using a fast photodiode and so the absolute frequencies of each mode can be known very accurately (better than one part in $10^{15}$ [67]). The spectral width of the comb is determined by the duration of the individual pulses which typically is around 1 — 10 fs giving the comb a bandwidth, $\Delta\omega_{env} = 1/\Delta t_{env}$, of 100 — 1000 THz. The direct correspondence between the temporal properties of the pulse train and the spectral properties of the OFC allows for the generation of high precision combs that can be tailored to a particular application.

In reality the pulses are not quite identical, and a phase difference is often observed in the carrier oscillation from one pulse to the next (as shown in Figure 2.3(a)). This is a result of the different velocity with which the pulse envelope ($A(t)$) and the carrier propagate within the cavity, a result of dispersion. The difference between these group and phase velocities, $v_g$ and $v_p$ respectively, leads to the carrier shifting with respect to the pulse envelope by a certain phase angle on each round trip; this phase difference is named the carrier-envelope offset (CEO). The absolute frequencies of the components of the frequency comb are thus shifted by a CEO frequency $\omega_o$ and now given by

$$\omega_n = \omega_c \pm n\Delta\omega_{rep} + \omega_o \,. \tag{2.19}$$

It is possible to stabilise the OFCS to give a constant or zero value for $\omega_o$ with a feedback system that monitors beat signals between different frequencies within the comb and controls the dispersive properties of the laser cavity. By stabilising $\omega_o$ and $\omega_{rep}$ to a frequency standard (such as the GPS signal, or an optical frequency clock) it is possible to know the mode frequency of the OFC very accurately and to produce combs with extremely narrow linewidths (even below 1 Hz in the best cases).

Titanium sapphire femtosecond lasers have been used to produce optical frequency

combs spanning large sections of the visible and near-IR region ($\sim$ 600 — 1000 nm). However, the ultrashort pulses and high spectral brightness of OFCSs enable efficient non-linear optical generation of combs in other frequency region through the use of methods such as difference frequency generation (DFG) and with optical parametric oscillators (OPOs). This allows frequency combs to be generated in regions more suited for spectroscopy such as the mid-infrared. Optical frequency combs can be generated directly in the near-IR with sources such as Er or Yb-doped fibre lasers or broadband oscillators based on $Cr^{2+}$:ZeSe gain media.

**Spectroscopy with frequency combs**

Optical frequency combs are considered to have great potential as tools for spectroscopy as they provide the unique combination of high spectral resolution with broad spectral coverage, in addition to producing radiation in regions that can be difficult to reach with conventional laser sources [68]. OFCs have principally been applied to spectroscopy in one of two ways. To date the majority of applications have used the precise frequency scale provided by an OFC to measure, in an extremely accurate manner, the frequency of a CW laser used to probe atomic or molecular transitions. In such methods the OFC provides a "frequency-ruler" to which the laser used to perform spectroscopy can be calibrated allowing spectra to be recorded with accurate, absolute frequency scales. This technique has found applications in the comparison of atomic frequency standards [67, 69], measurement of physical constants [70], and the investigation of the functional form of pressure-broadened line profiles [62, 71].

Of more interest to multi-species detection is the application of femtosecond combs to probe molecular transitions directly, a technique known as direct frequency comb spectroscopy (DFCS). DFCS can use the entire bandwidth of an optical frequency comb to perform absorption spectroscopy with maximum resolution determined by the

comb mode width, which can be sub-Hertz, and the results are virtually equivalent to simultaneous measurement with many thousand narrow linewidth lasers. OFCs have additional advantages as light sources for spectroscopy: the very high spectral brightness of such radiation (much higher than from a thermal source) improves the signal to noise ratio experienced by detectors. In addition some schemes allow the use of lock-in detection, and as the source repetition rate is very high (100 MHz — 1 GHz) compared to usual modulation rates used in spectroscopy (kHz) this substantially reduces low-frequency noise [68]. The signal produced by DFC spectrometers, and thus the sensitivity of the instrument for trace gas detection, can be dramatically increased by coupling the frequency comb into a high finesse optical cavity, providing an increase of absorption pathlength [72]. OFCs are well suited to such coupling as the comb structure can be matched to the ladder of cavity modes allowing for high transmission.

The DFCS technique has much potential for multi-species detection, however, the intrinsically parallel measurement presents the challenge of designing a detection scheme capable of resolving the comb modes. As such many different spectrometer designs have been reported, employing different methods to provide spectral discrimination. The simplest form of femtosecond comb spectroscopy, however, does not require external frequency dispersion. Fluorescence detection relies on the frequency selection provided by molecular transitions to select individual comb modes. In this approach the frequency comb illuminates a sample and the fluorescence from excited states is detected whilst the comb is scanned to bring individual comb modes into resonance with different transitions. The large number of modes in the laser comb make this method difficult for complex systems, however, due to the production of complex spectra.

Techniques with more general applicability include those making use of high-resolution spectrometers to allow individual frequency components in the comb to be distinguished after they have interacted with the sample. A simple grating spectrometer can be used

to disperse spectra over a large bandwidth (tens of nm) for recording on a multi-element photo-detector, however, the spectral resolution achievable with such systems is not sufficient to resolve the comb modes. Fabry-Perot etalons provide much higher resolution but their limited free spectral range (FSR) limits the achievable bandwidth due to the appearance of overlapping orders. Therefore systems have been reported using two orthogonal spectral dispersers, such as a grating and a virtually-imaged phased array (VIPA), to provide 2D spatial separation of comb modes and thus allowing high-resolution trace gas detection to be performed. Such a system was reported by Diddams *et al.* in 2007 [60] who used a Ti:sapphire laser comb with mode spacing 1 GHz (pre-filtered by a Fabry-Perot cavity to 3 GHz) to detect transitions of molecular iodine around 633 nm with a bandwidth of 6 THz. The overall spectral resolution achieved in this system was 1.2 GHz allowing monitoring of the intensity of individual comb frequencies and spectra were recorded with millisecond time resolution. This technique is known as *molecular fingerprinting*. An alternative approach uses an optical cavity, with FSR slightly detuned from the comb mode spacing to select comb modes by the Vernier effect. This method may then be combined with frequency dispersion to provide additional discrimination. Thorpe and co-workers reported a spectrometer designed to analyse human breath for medical diagnostics using this technique [61, 73].

An alternative detection scheme for DFCS is Fourier transform spectroscopy, implemented either with a scanning Michelson interferometer [64, 65, 74] or the interference of two femtosecond laser combs of slightly different $\omega_{rep}$ [63, 75]. These methods provide high spectral resolution over a wider bandwidth than can be achieved with dispersive techniques. In particular, dual-comb DFCS (also known as coherent multi-heterodyne spectroscopy) allows broadband spectra to be recorded with a time resolution of the order of microseconds [63]. This technique uses one optical frequency comb to probe a gas sample, before combining this with an independent comb to create a heterodyne

signal which is recorded with a high-speed photodetector. This process down-converts the optical combs to produce a radiofrequency spectrum, providing a better method than high resolution spectrometers of resolving individual comb modes, particularly for systems with narrow mode spacing [68]. However, to achieve the full potential of this technique in terms of spectral resolution, extremely fine control of the difference between repetition rates of the two lasers is required.

To summarise, frequency comb spectroscopy has already led to significant advances in the measurement of physical constants and the development of new frequency standards based on optical atomic clocks, and has recently started to be applied to the measurements of molecular systems and samples. Comb-assisted spectroscopy has been used to measure lineshape parameters and molecular energy structures, but it is the application of these combs directly to spectroscopy that is of interest for trace gas detection. Direct frequency comb spectroscopy, used in conjuction with a high finesse optical cavity allows spectra to be recorded with simultaneously broad spectral coverage, high resolution, high sensitivity and short time resolution and so would seem to be ideal for the detection of multiple trace species. However, the sheer complexity of the equipment needed to build a cavity enhanced DFCS spectrometer, and the precision needed to be maintained to achieve optimum performance, makes this technique difficult to deploy for field measurements and will preclude its use as a technique for an industrial gas sensor for the foreseeable future.

## 2.6 MUMAS for multi-species detection

A novel approach to the spectroscopy of multiple transitions that simultaneously achieves wide spectral coverage and high spectral resolution has recently been developed [6–9, 45]. This technique, multi-mode absorption spectroscopy (MUMAS), uses a comb of

longitudinal modes from a short cavity laser which are simultaneously scanned over a frequency range corresponding to the mode spacing. Absorption of light from any mode of the comb is detected by the consequent reduction in total transmitted intensity and a modelled fit to the data allows identification and quantitative detection of absorbers. For well-behaved multimode lasers the technique of MUMAS offers a simple and direct approach to acquiring spectral information on multiple transitions spread across an extended spectral range.

MUMAS thus provides a viable alternative to multiplexing methods involving multiple lasers and multiple detectors, whilst only requiring one laser and a simple detection scheme. In contrast to gas correlation spectroscopy, MUMAS does not require reference samples and can detect species at unknown pressure and temperature, and unlike broadband spectroscopy MUMAS does not require complex dispersive detection schemes. The principle of MUMAS is described in the next chapter.

### 2.6.1 Review of previous MUMAS work

The first demonstration of MUMAS was reported in 2008. A multi-mode Fabry-Perot diode laser, operating around around 760 nm was used to detect transitions in the A-band $b^1\Sigma_g^+ - X^3\Sigma_g^-$ of molecular oxygen [6]. This same system was subsequently used to demonstrate the ability of MUMAS to perform concentration and temperature measurements through the simultaneous detection of multiple transitions. The pressure and temperature of oxygen samples was measured over a range of conditions, in independent procedures, and both sets of measurements were found to have a precision better than $\pm 2$ % [7]. The sensitivity enhancement techniques of cavity enhanced absorption spectroscopy (CEAS) and wavelength modulation spectroscopy (WMS) were later applied to this system, both individually and together, to yield an improvement to the signal to noise ratio of this system and thus demonstrating the applicability of these techniques to MUMAS [9].

MUMAS measurements using an Er/Yb:glass micro-cavity laser were also reported in 2008, demonstrating the generality of the MUMAS technique to application with different laser sources [8]. In this work several transitions from the $\nu_1 + \nu_3$ combination band of acetylene were detected around 1.53 $\mu$m.

This thesis reports work with the aim of extending the MUMAS technique both to the detection of multiple species and to gas sensing in the mid-infrared spectral region. An improved multi-mode Er/Yb:glass laser has been developed (see Chapter 4), and this source has been used to detect multiple gaseous species from within a gas mixture. This work is discussed in Chapter 5. The same Er/Yb laser has also been used to generate a mid-infrared multi-mode comb through difference frequency generation. This frequency-shifted comb was used for multi-species detection, and showed increased sensitivity due to the strength of the transitions in this region (Chapter 6).

## 2.7 Summary

This chapter has described the context into which multi-mode absorption spectroscopy fits and the motivation for developing this technique. Firstly, optical sensing techniques were introduced as a method to perform measurements of concentration, pressure and temperature of gas samples, with particular reference to the use of these techniques in sensors deployed for "field" measurements. The physical principles behind absorption spectroscopy have been briefly surveyed and TDLAS has been introduced as the principal method by which selective measurements are currently performed.

The focus then moved to performing measurements of multiple transitions simultaneously, to allow both the determination of multiple properties of a single species, and the determination of a single property in many species. A selection of existing multi-transition detection methods have been discussed: TDLAS with multiplexed diode lasers

and with wavelength-agile sources, broadband spectroscopy, gas correlation spectroscopy, and femtosecond comb spectroscopy; the benefits of, and problems with, these methods have been considered.

Finally, multi-mode absorption spectroscopy has been introduced as a novel method to perform multi-transition sensing. This is the technique used for the experimental work reported in this thesis.

# Chapter 3

# The MUMAS technique

## 3.1 Introduction

This chapter describes the multi-mode absorption spectroscopy (MUMAS) technique that is the basis of all the work reported in this thesis. The chapter starts by explaining the principle by which MUMAS operates, and the way in which spectra are recorded. The general shape of a MUMAS signal is discussed, and the factors that determine its specific form considered; it is seen that these factors arise both from properties of the gas sample and those of the multi-mode laser.

To perform a measurement on a sample with MUMAS it is necessary to fit a modelled spectrum to the experimental data. The steps required to produce this modelled MUMAS spectrum are also described and the method by which these are carried out in practice is explained. A computer model was previously written to produce this theoretical spectrum but in the course of this work it was found necessary to extensively rewrite this simulation; the reasons behind this and particular considerations required to produce a stable, efficient model are discussed.

Finally, the laser source used for MUMAS is discussed. The properties required of

this source and their effect on the recorded spectrum are explained.

## 3.2 Theory of operation

Multi-mode absorption spectroscopy is an absorption spectroscopy technique that uses the interaction between multi-longitudinal-mode laser radiation and molecular absorption transitions to probe molecular species in a gaseous sample.

The operating principle of MUMAS is illustrated in Figure 3.1(a), a diagram showing a comb of several laser modes (shown in blue) overlying a set of absorption transitions (in red). The laser comb comprises radiation at a number of distinct, well defined frequencies, spaced by equal frequency gaps, termed the mode spacing, $\Delta\nu_{space}$. The individual molecular transitions, each of finite width, of known strength, and at precisely known frequency, together form the spectral transmission profile of the gas sample.

To record a MUMAS spectrum the laser modes are scanned together across a frequency range given by the mode spacing. As individual laser modes come into resonance with molecular transitions radiation is absorbed, causing a reduction in the total intensity transmitted through a gas sample. The MUMAS technique observes these dips in the intensity of radiation transmitted through a sample, and uses this spectral measurement together with known properties of the incident laser radiation to infer information about the gas sample. The observed transmission pattern provides a unique, characteristic signature for the absorption of a particular laser output by a particular set of transitions and hence can be described as a "MUMAS fingerprint".

During MUMAS, the laser modes only need to be scanned across a frequency equivalent to one mode spacing. Each mode "sweeps-out" the frequency region between its own starting position and that of the adjacent mode, and so the entire spectral window corresponding to the output bandwidth of the multi-mode laser is probed. Therefore, a

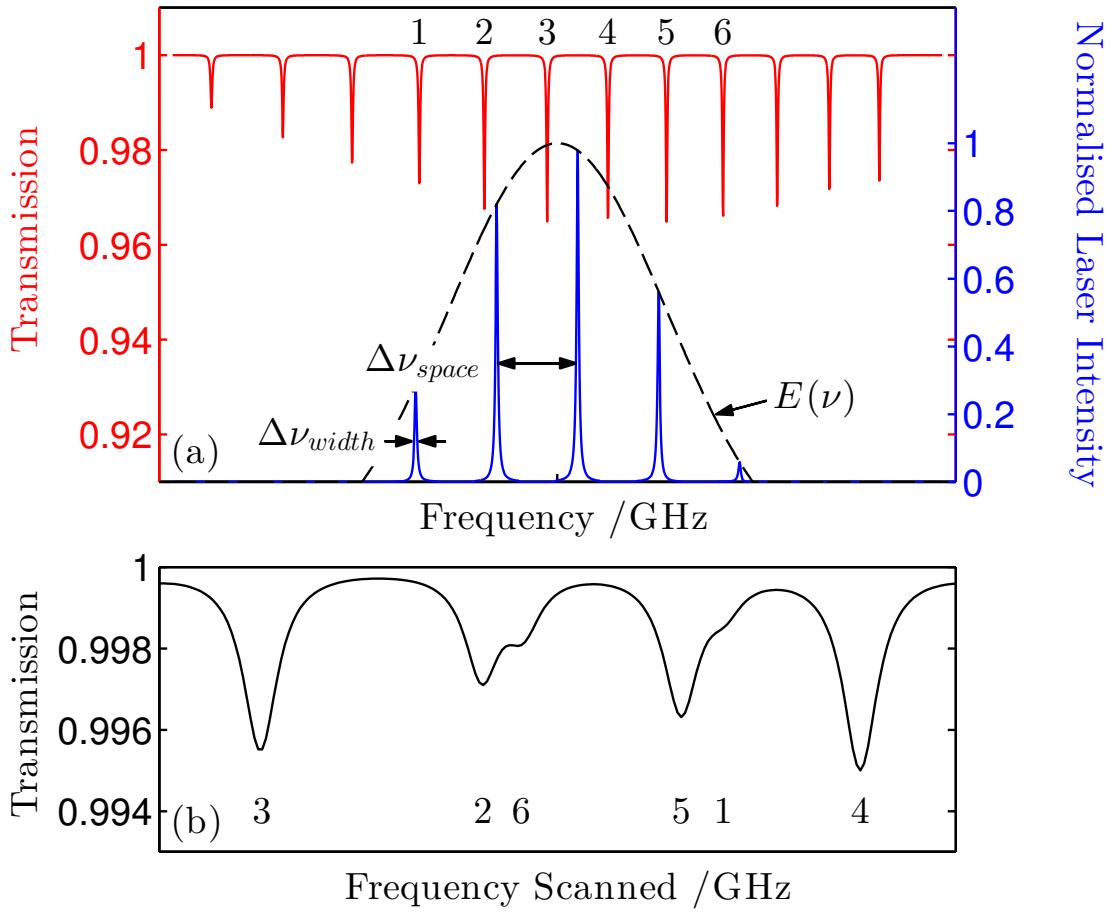


**Figure 3.1:** A diagram illustrating the principle of MUMAS. **(a)** A comb of laser modes (blue) is shown overlying molecular absorption features (red). Key properties of the comb are labelled and the six transitions that interact with the laser comb are labelled 1 — 6. To record a MUMAS spectrum such as that shown in **(b)** the laser modes are scanned over a frequency range equal to one mode spacing. It can be seen that all 6 transitions contribute to the MUMAS spectrum but the order which they appear has been mixed up.

MUMAS spectrum generated using $n$ modes is equivalent to the weighted superposition of a set of $n$-individual absorption spectra, each the result of a single laser mode.

The measured transmission pattern is placed on a scale that corresponds to the frequency scanned by the laser modes, and each absorption feature appears at a position determined by its location relative to the starting and finishing position of the scanning laser mode. Unlike typical absorption spectra, this relative frequency scale cannot then be placed on an absolute frequency or wavelength scale as it contains contributions from several distinct spectral regions.

An example of such a transmission trace is shown in Figure 3.1(b). This MUMAS spectrum contains several absorption "dips" corresponding to the same number of molecular absorptions that interacted with the laser comb. However, from the labelling of these features it is clear that the order they appear in the MUMAS trace is determined by the order that they interacted with a laser mode rather than their spectral position. The MUMAS signature contains the information from the molecular transmission spectrum, but this information has been encoded by the multi-mode laser probing it.

The form of a MUMAS spectrum is therefore dependent upon both the spectral properties of the laser output and details of the gas sample. The key parameters of the laser spectrum are labelled in Figure 3.1 and include the mode spacing, $\Delta\nu_{space}$, the individual mode linewidth, $\Delta\nu_{width}$, and the intensity envelope of the laser comb, $E(\nu)$. This intensity envelope function determines the central frequency of the comb, $\nu_{centre}$, the spectral range covered by laser $\Delta\nu_{bandwidth}$, and the number of modes, $n$. The precise starting frequencies of the laser modes dictate the order absorption features appear in the fingerprint.

Several properties of the gas sample influence the form of a MUMAS trace, arising from both the inherent properties of the absorber molecules present in the sample and the conditions of the bulk gas. Each species of absorber molecule in the gas sample will

add a unique set of absorption transitions to the output spectrum, and each of these transitions has an associated spectral position, set of temperature and pressure dependent broadening coefficients, and temperature dependent line strength factors. The position, lineshape and depth of the absorption "dips" in the MUMAS spectrum therefore encode information on the identity of absorbers and the pressure and temperature conditions experienced by these molecules. The MUMAS spectrum thus contains information on composition, pressure and temperature of the gas sample.

## 3.3 Modelling of MUMAS

A MUMAS signature contains encoded information about the pressure, temperature and composition of the measured gas sample. To extract this information, and thus perform a measurement on an experimental system with MUMAS, it is necessary to generate a modelled spectrum for the expected experimental conditions and then to allow a fitting algorithm to adjust the input parameters of this model to give the best fit to the measured data. The parameters of this best fit are then taken as the experimental measurement.

The modelling of MUMAS is illustrated in Figure 3.2 and can conceptually be thought to consist of three steps: firstly, the spectral transmission of the gas sample is calculated taking into account transitions from any absorbing species present. In this example, the modelled transmission spectrum of a sample of 20 mbar of $N_2O$ buffered up to a total pressure of 0.1 bar with air is shown in red. Then, the output spectrum of the multimode laser is numerically simulated, here shown in blue. Finally the interaction between the simulated laser comb and molecules in the gas sample is considered to model the expected MUMAS transmission spectrum. The modelled spectrum for this system is shown in black.

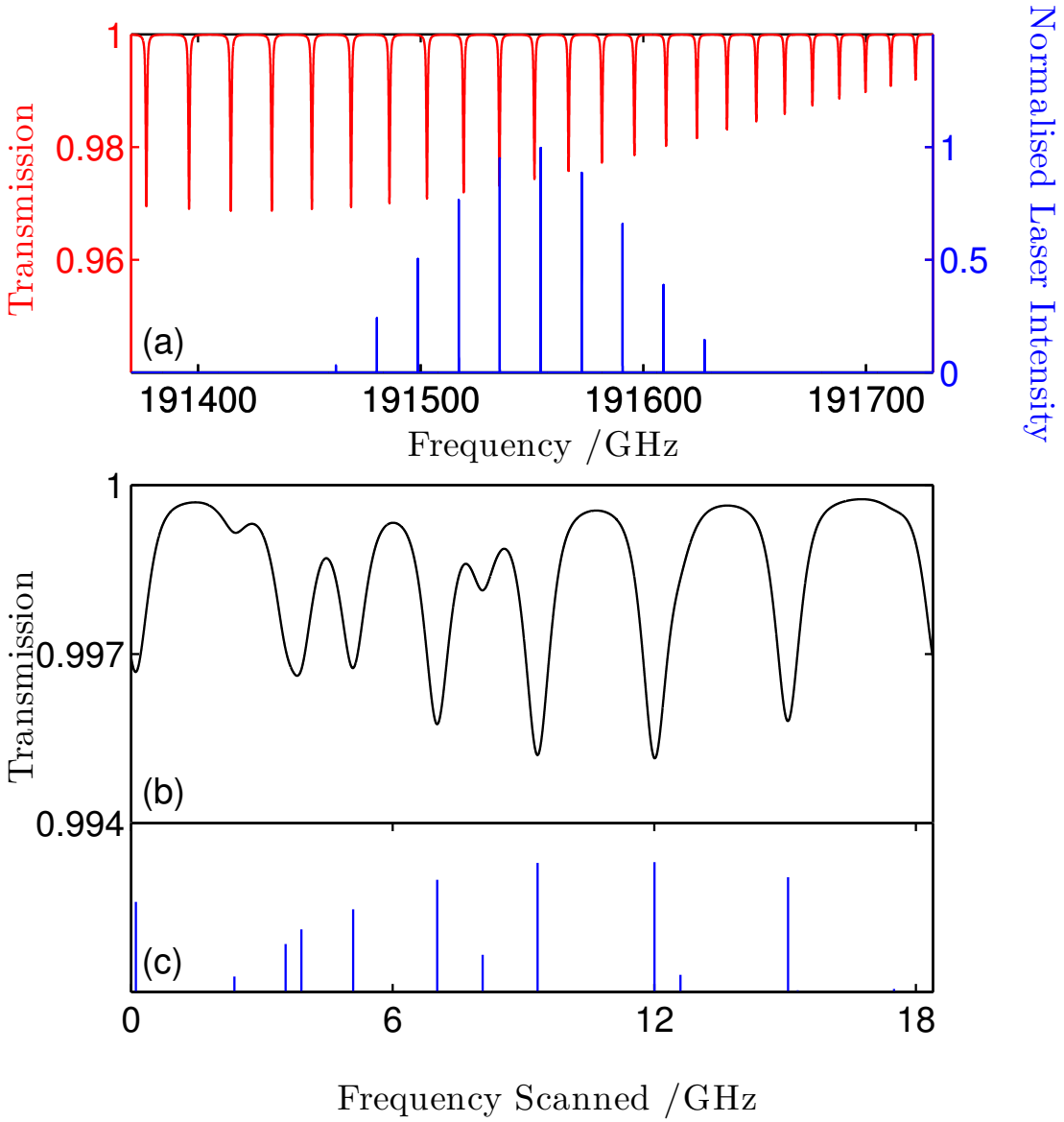


**Figure 3.2:** An overview of the stages of modelling a MUMAS spectrum. **(a)** shows a modelled laser comb (blue, lower) overlying a set of doppler and pressure broadened $N_2O$ transitions (red, top). It should be noted that although the laser modes appear as lines they are plotted with widths typical of the Er/Yb:glass micro-cavity laser used in the work reported later in this thesis. **(b)** shows the MUMAS spectrum for this system. This is calculated by scanning the laser comb over one mode spacing and considering its interaction with the molecular absorptions. The absorption dips in the MUMAS trace appear in an unconventional order (that is different to that on a frequency axis) due to the multi-mode scanning. There is a one to one correspondence between transitions and dips in the MUMAS trace however, as illustrated by the spectral assignments in **(c)** where each vertical line corresponds to a transition in the modelled species.

A computer model was written to carry out this numerical simulation for previous work [6, 45]. This model has been almost entirely rewritten to implement several improvements in the course of the work reported here. These changes principally relate to modifying the model to ensure it continued to produce correct results as properties of the multimode lasers changed beyond original specifications, extending the model to allow simulation of multi-species MUMAS traces, reducing the computational time required to run the model, and making the model more modular enabling more flexible usage.

The model is written in the MATLAB® programming language and accepts input parameters describing properties of the laser and gas sample. It uses these together with information describing molecular transitions extracted from spectral database files to produce a simulated MUMAS trace for the chosen conditions. The modelling is carried out only over a spectral region slightly wider than the bandwidth of the laser comb to produce an accurate representation of the real system while minimising the computation time.

For simplicity the discussion below describes the modelling calculations as operations on continuous functions, however, in reality this is a discrete numerical simulation. Vectors describing the properties of the system are subjected to discrete operations and hence the simulation has an in-built resolution limit, which must be considered and set to a suitable value.

### 3.3.1 Gas sample transmission modelling

The modelling process starts by searching a spectral database such as HITRAN [76] for transitions that fall within a window defined by the output bandwidth of the multi-mode laser. Data describing the position, strength and broadening coefficients for each of these transitions is then imported.

To model the MUMAS spectrum at an arbitrary temperature, $T$, it is necessary to

re-weight the line strength factors. This is to allow for the difference in populations determined by the Maxwell-Boltzman distribution, assuming thermal equilibrium, experienced at this temperature compared to that at which the database was compiled. This re-weighting is performed using the equation

$$S_{if}(T) = S_{if}(T_{ref})\frac{Q\left(T_{ref}\right)}{Q(T)}\frac{\exp\left(\frac{-hcE_i}{k_BT}\right)}{\exp\left(\frac{-hcE_i}{k_BT_{ref}}\right)}\frac{\left(1-\exp(\frac{-hc\tilde{\nu}_{if}}{k_BT})\right)}{\left(1-\exp(\frac{-hc\tilde{\nu}_{if}}{k_BT_{ref}})\right)} \tag{3.1}$$

which describes the line strength of a transition between a lower state, $i$, and upper state, $f$, as a function of temperature, $T$. For the HITRAN database the line centres ($\tilde{\nu}_{if}$) and energy of the lower states ($E_i$) are reported in wavenumbers and the reference temperature, $T_{ref}$, is 296 K [77]. Values for the total partition sum, $Q$, are also provided by HITRAN.

This re-weighting of the line strength factors provides adequate accuracy for temperatures close to room temperature, however, at very high temperatures transitions not present in this database may become important, for example those arising from "hot bands" (transitions having initial vibrational states lying above the ground state). This may necessitate the use of a database compiled for high temperatures, such as HITEMP [77].

Once spectroscopic parameters for each transition have been obtained, the absorption arising from each transition needs to be calculated. This process takes into account the number density of the molecule in question, the absorption pathlength and the absorption cross-section, $n$, $l$ and $\sigma_{if}$, respectively. The absorption cross-section, $\sigma_{if}$, is obtained by multiplying the line strength factor by a lineshape function to represent the effects of transition broadening.

$$\sigma_{if} = S_{if} \cdot g_V\left(\nu - \nu_0\right) . \tag{3.2}$$

These lineshapes are modelled as a Voigt function, $g_V(\nu - \nu_0)$, to represent the effect of the two dominant forms of broadening: Doppler broadening and pressure broadening. These processes were described in Section 2.3.2. The pressure broadening comprises two components, self broadening and foreign gas broadening, which are calculated separately and combined to produce the overall profile. The reduction in transmission through the sample arising from each transition can be described using

$$T_{if}(\nu) = \exp\left( -\sigma_{if} \cdot n \cdot l \right) \tag{3.3}$$

and total spectral transmission of the gas sample, $T(\nu)$, is calculated by combining the broadened absorption profile from all transitions,

$$T(\nu) = \sum_{if} T_{if}(\nu) \,. \tag{3.4}$$

### 3.3.2 Laser comb modelling

The laser output is modelled as a comb of equally spaced modes, each of unit height and with an extremely narrow Lorentzian profile. A Lorentzian profile was chosen to represent the laser line profile because it is believed to accurately represent the form of these modes (see Section 4.3.3) and also for reasons of computational simplicity. In practice, for the lasers used in the work reported here, the function used to represent the laser modes has little effect on the model output as the laser linewidth is orders of magnitude narrower than that of the absorption transitions measured.

The necessity of knowing the precise starting frequency of these modes (within a fraction of one mode spacing), a property extremely sensitive to cavity length, is avoided by including a cross-correlation of the model output against experimental data in the fitting algorithm. This takes advantage of the fact that a set of modes sweep out the entire

range of the envelope function over a scan, and hence arbitrary starting positions can be chosen for the modelled modes provided that the position of the envelope function itself is correct. Differences in these starting positions will lead only to MUMAS spectra differing through a cyclic shift of features. This is described in more detail in Section 5.3.2.

The envelope function that describes the distribution of intensity in the laser comb can be arbitrarily chosen. In previous work, where the form of the comb was determined by an external interference filter, an Airy function was used [6]. In the work reported here the comb envelope is an inherent property of the Er/Yb:glass micro-cavity laser used as the multi-mode source. In this case, a particular function – the result of subtracting a constant from a Gaussian profile – was empirically found to produce a good representation of the envelope shape.

The modelled comb, $L(\nu)$, is thus produced by multiplying the ladder of unit-height cavity modes, $C(\nu)$, by an envelope function, $E(\nu)$, to give a modelled laser output with the correct spectral profile.

$$L(\nu) = C(\nu) \cdot E(\nu) \tag{3.5}$$

### 3.3.3 Generating the MUMAS spectrum

A modelled MUMAS spectrum, $M(s)$, is generated by simulating the interaction of the laser comb with the gas sample. To do this the system is considered throughout the laser scan and the total intensity in the laser comb is calculated both before ($I_0$) and after ($I$) passing through the gas sample. The ratio of these intensities as a function of scanned frequency gives the modelled MUMAS trace. This process can be expressed as

$$M(s) = \frac{I(s)}{I_0(s)} = \frac{\int_{\nu_1}^{\nu_2} L(\nu, s) \cdot T(\nu) \cdot d\nu}{\int_{\nu_1}^{\nu_2} L(\nu, s) \cdot d\nu} \tag{3.6}$$

$$= \frac{\int_{\nu_1}^{\nu_2} C(\nu, s) \cdot E(\nu) \cdot T(\nu) \cdot d\nu}{\int_{\nu_1}^{\nu_2} C(\nu, s) \cdot E(\nu) \cdot d\nu} \tag{3.7}$$

where the variable $s$ refers to the frequency the laser modes are scanned over. The limits, $\nu_1$ and $\nu_2$, extend a little wider than the envelope limits. An example of a modelled MUMAS spectrum is shown in Figure 3.2.

### 3.3.4 Computational considerations

During the process of fitting the model to experimental data it is necessary to run the MUMAS model many times, and thus the computational efficiency of the model should be maximised to allow this fitting process to complete in a reasonable time. To achieve this goal, the numerical approach employed in the MATLAB code departs from the explanation given above, as will be described in the following section.

#### Reducing unnecessary modelling

The MUMAS model forms a module of computer code, written as a master function and a collection of sub-functions. The master function runs once per iteration of the model, and calls respective sub-functions to perform each part of the modelling process, such as: importing molecular transition parameters, adjusting the line strength parameters for differing temperatures, calculating the linewidth of each absorption, simulating the laser modes and applying the comb envelope function.

Typical usage of the MUMAS model involves the master function being called many times by a fitting algorithm, with small changes to one or more of the input parameters. Under these circumstances, many sub-calculations do not need to be repeated from one run to the next, for example if a parameter affecting the laser is changed the transmission spectrum of the gas sample need not be re-calculated. The master function contains logic to determine whether each calculation is necessary, and if not, reduces computational load by using a previously stored value. Therefore each call to the master function may only consist of a subset of the stages described above.

### Approximation of Voigt profiles

Spectral lineshapes for each transition are modelled as Voigt profiles. These could be calculated through the numerical convolution of Lorentzian and Gaussian profiles, however, these line profiles can be generated much more efficiently, and without significant error, through the use of an empirical Voigt approximation. The approximation chosen was first published by Whiting [78] and developed by Olivero and Longbothum [79]. It is reported in Brassington [21] in the form:

$$\begin{aligned}\sigma_\nu(\nu) = \sigma_\nu(\nu_0)\big\{&(1-x)\exp(-0.693y^2) + x/(1+y^2) \\ &+0.016(1-x)x[\exp(0.0841y^{2.25}) - 1/(1+0.210y^{2.25})]\big\}\end{aligned} \tag{3.8}$$

where $x = \gamma_L/\gamma_V$, and $y = |\nu - \nu_0|/\gamma_V$. $\gamma_V$ is the Voigt profile HWHM given approximately by:

$$\gamma_V = 0.5346\gamma_L + (0.2166\gamma_L^2 + \gamma_D^2)^{\frac{1}{2}} \tag{3.9}$$

and $\sigma_V(\nu_0)$ the cross-section at line centre is given by:

$$\sigma_V(\nu_0) = S/[2\gamma_V(1.065 + 0.447x + 0.058x^2)] \tag{3.10}$$

### Array representation of the laser scan

The way in which the model calculates the scan of the laser modes to generate a MUMAS trace has been changed from the original model. The original model calculated the MUMAS trace by describing the laser comb as a 1D row vector, $L(\nu)$, of length $n_{laser}$, which was represented at each of $n_{scan}$ points during its scan as a separate row in a 2D array, $\mathbf{L}$. This array was multiplied in an element-wise manner with an array, $\mathbf{T}$, of the same dimensions, which comprised identical rows, each equal to the vector describing the spectral transmission of the gas sample, $T(\nu)$. The resultant array was then summed

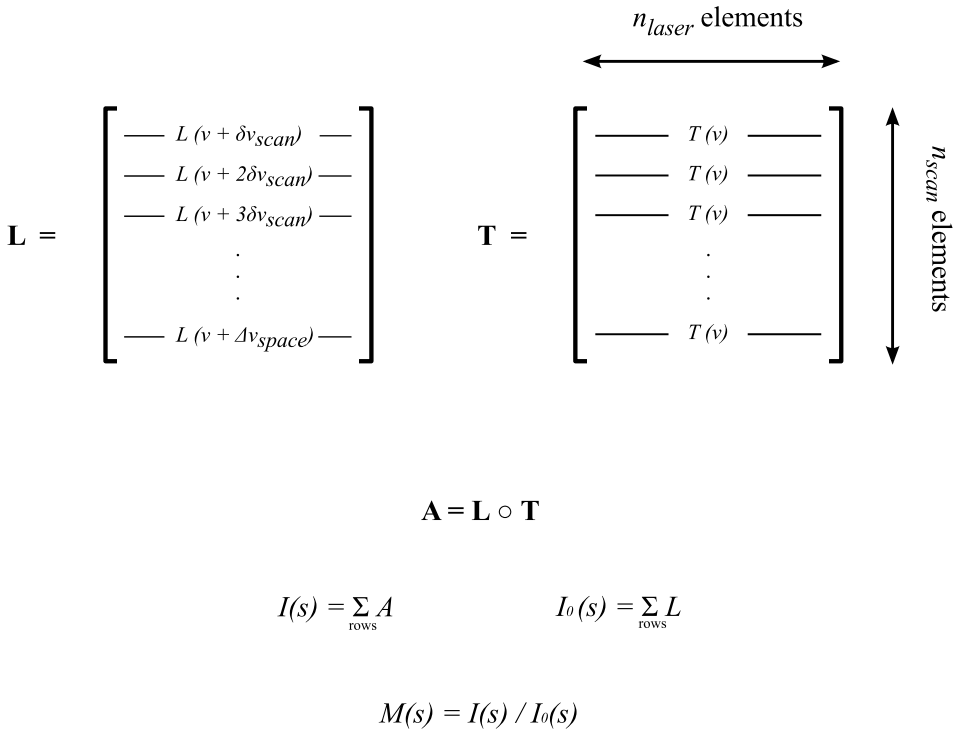


**Figure 3.3:** An illustration of the computation of a MUMAS spectrum with the previous model. The ∘ symbol represents an element-wise product. A full description of the process can be found in the main text.

along its rows to generate the total transmission signal at each point in the scan, $I\,(s)$, and divided by an $I_0\,(s)$ vector produced in a similar manner, to finally produce the simulated MUMAS trace. This process is illustrated in Figure 3.3.

This method is computationally simpler than a loop-wise implementation in MATLAB, however, it requires a large amount of computer memory to store large intermediate arrays (of dimensions $n_{laser}$ by $n_{scan}$). To accurately represent the laser comb the spectral resolution parameter, $\delta\nu_{laser}$, needs to be approximately ten times smaller than the mode linewidth, meaning that $n_{laser} \approx 5\Delta\nu_{env}/\delta\nu_{laser} = 50\Delta\nu_{env}/\Delta\nu_{width}$ (the factor 5 refers to the width of the modelling window in units of $\Delta\nu_{env}$ and is chosen to allow accurate modelling without excess calculation). The original model also calculates the

MUMAS spectrum to the same spectral resolution, i.e. $\delta\nu_{scan} = \delta\nu_{laser}$, hence producing a simulated MUMAS trace of length $n_{scan} = \Delta\nu_{space}/\delta\nu_{scan} = 10\Delta\nu_{space}/\Delta\nu_{width}$.

This model was written to accurately simulate MUMAS with a diode laser which had fairly broad linewidth compared to its mode spacing and envelope width (typical values: $\Delta\nu_{space} \approx 50$ GHz, $\Delta\nu_{width} \approx 1$ GHz, $\Delta\nu_{env} \approx 150$ GHz (FWHM)). This gives intermediate arrays with $\approx 10^6$ elements. When stored as double precision floating point numbers such arrays would each require around 8 megabytes of memory to store – a manageable size [80]. The Er/Yb:glass micro-cavity laser described in Chapters 4 and 5 has a linewidth more than 100 times narrower ($< 10$ MHz) and hence required intermediate arrays with closer to $10^{10}$ elements. This would require tens of gigabytes of memory to store each array, which is not practical with current desktop computers.

This model can be modified to reduce memory usage without excessive loss of precision by modelling the laser scan at a lower resolution than that which describes the laser comb ($\delta\nu_{scan} \neq \delta\nu_{laser}$). This, along with narrowing the modelling window to a minimum, can reduce the size of the arrays used, but is still not sufficient to make this model practical for the Er/Yb:glass laser. It was noted, however, that although a fine resolution is required in the $L(\nu)$ vector to adequately represent the modes, the vast majority of the points were equal to zero; such arrays are described as sparse, and can be more efficiently stored as a list of locations and values of the non-zero elements. Therefore the model was modified to represent the intermediate arrays as sparse matrices, thus only requiring memory to store non-zero elements. Together these changes allowed the modelling of the Er/Yb:glass laser.

#### Cross-correlation calculation of the laser scan

A better method of modelling the laser scan has since been developed that removes the necessity of such large intermediate arrays without resorting to a slow loop-wise

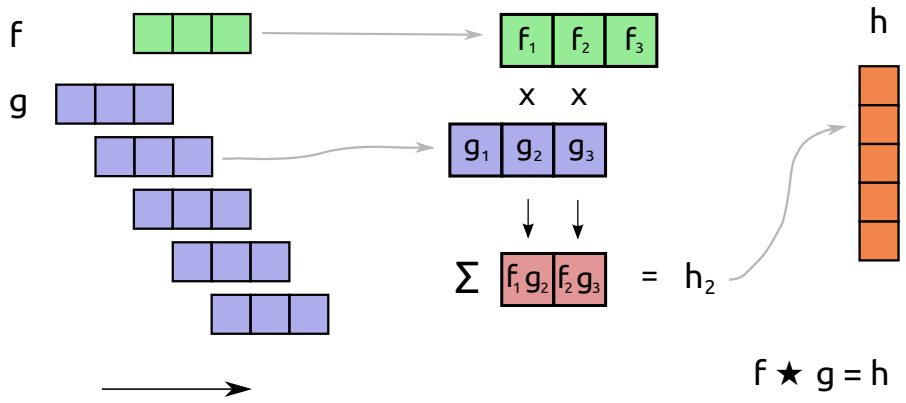


**Figure 3.4:** A diagram illustrated the discrete cross-correlation operation for real numbers. One vector is stepped past another (left) and at each step the sum of the element-wise products of over-lapping elements is calculated (centre). The result is a vector that has length equal to the number of steps (right) and which describes the overlap of the vectors at each offset.

implementation. The process of simulating the laser scanning past the absorption features – moving one vector past another, whilst calculating the sum of the element-wise product at each point – shares similarities with a cross-correlation.

A cross-correlation is defined as the result of sliding one signal past another, calculating the integral (or the sum in the discrete case) of the element-wise product at each point. This process is best understood through the use of a diagram, such as that shown in Figure 3.4, which illustrates the cross-correlation of two three-element vectors. In this diagram the cross-correlation of two vectors $f$ and $g$, both of equal length $N = 3$, produces a vector $h$ of length $2N - 1 = 5$. The process can be summarised for real numbers as

$$h_{[n]} = f \star g = \sum_{m=-\infty}^{\infty} f_{[m]}\, g_{[m+n]} \tag{3.11}$$

where $\star$ signifies the cross-correlation and subscripts are used for indexing vectors [81].

To generate a MUMAS spectrum by means of cross-correlation, two vectors should be produced: one representing the elements of the MUMAS system that are fixed in

frequency space, and one representing the scanning elements. For the former, the "unphysical" step of applying the laser comb envelope function ($E(\nu)$) to the gas transmission spectrum ($T(\nu)$) is taken. This frequency-fixed vector is then cross-correlated with a vector describing a ladder of unit-height cavity modes ($C(\nu)$). A small section of this result, equivalent to a scan of one mode spacing, then needs to be selected to represent $I(s)$ and a similar section of another cross-correlation (produced for a transmission of unity) taken to produce $I_0(s)$.

Although most of the resulting vector is discarded ($\sim 95\%$ for the lasers used in this work), making this seem like a wasteful method to simulate a short scan, this approach allows efficient computation of the cross-correlation by using Fast Fourier Transform (FFT) algorithms [81]. In analogy to convolution theory, a cross-correlation of two vectors is linked to the element-wise product of those vectors through Fourier transforms:

$$f \star g = \mathfrak{F}^{-1}\left[ \left(\mathfrak{F}\{f\}\right)^* \cdot \left(\mathfrak{F}\{g\}\right) \right] \tag{3.12}$$

where $\mathfrak{F}$ represents a Fourier transform, $\mathfrak{F}^{-1}$ its inverse, and $*$ the complex conjugate. MATLAB implements such a method in the *xcorr* function, part of the *signal processing toolbox*.

In summary the MUMAS model has been re-implemented using the *xcorr* function. This new model produces exactly equivalent results to the earlier versions while removing the memory limitations caused by using intermediate arrays. The time needed to produce a modelled spectrum is also reduced, often by more than 50%.

## 3.4 The multi-mode source

MUMAS is a widely applicable laser spectroscopy technique that can be carried out with any laser source that meets a small number of requirements. Some of these requirements

are very simple and would equally be required of a single mode laser used for absorption spectroscopy; for example, the need for the scanned output wavelength range to overlap with the wavelengths of transitions to be measured. Equally, the degree of intensity noise is important as this is directly linked to the signal to noise ratio and hence the minimum detection limits of the system.

Other requirements are particular to a laser used for MUMAS. The simplest of these is the requirement for the laser to produce output radiation simultaneously on several different longitudinal cavity modes — in the limit of reducing the number of lasing modes to one, MUMAS reverts to traditional single-mode laser absorption spectroscopy.

MUMAS has been described as a technique requiring "well-behaved multi-mode lasers" [6]. This refers to the necessity for the laser to operate in a way that is repeatable from one scan to the next, to allow averaging of spectra, but more importantly to operate in a predictable way within a single scan. This is in contrast to gas correlation spectroscopy (see Section 2.5.3), a technique that can utilise lasers exhibiting mode-hops and other temporal instabilities [56, 58]. Stability and predictability are required for MUMAS as it is not practical to measure the changes in mode structure throughout the laser scan – these parameters need to evolve in a predictable manner to allow for modelling of experimental data. The relative intensity of the laser modes must be temporally stable and must change through the scan in a manner determined purely by the envelope function. The laser must be designed in such a way that modes lase independently to a good degree: competition between modes for the energy stored in the gain medium will lead to random fluctuations in mode intensity. Fluctuations occurring at frequencies comparable to the scan rate of the laser will lead to measurement errors.

In addition to meeting these requirements, several properties of the laser source affect the form of the recorded MUMAS spectrum and hence the values of these parameters are important to produce useful MUMAS spectra. These key parameters have been

mentioned in Section 3.2 and are labelled in Figure 3.1.

The spectral resolution of a MUMAS spectrum is dependent on the mode linewidth. The width of the measured absorption "dips" is determined by a convolution between the molecular transition linewidth and the mode linewidth ($\Delta\nu_{molecule} \otimes \Delta\nu_{width}$). Therefore it is important, if possible, to have a mode linewidth much narrower than the expected transition width. An additional advantage of having a laser with a mode linewidth much narrower than the measured transition linewidth is that the precise value of the mode linewidth is not required for fitting as it has little impact on the spectrum.

The mode spacing is the parameter that most sensitively affects the form of a MUMAS spectrum. MUMAS spectra are equivalent to the super-position of multiple absorption spectra, and the way in which these individual spectral fragments overlap is sensitively dependent on the mode spacing. Therefore if the same gas sample is measured with two lasers having mode spacings differing by even a small amount, two MUMAS spectra will be produced with very different structure and shape.

This super-position of individual spectral fragments also leads to a tendency for the technique to be hampered in already spectrally congested regions, meaning that many transitions may overlap, reducing the "contrast" of the data, and potentially causing a loss of information. To minimise this, it is important to ensure that the mode spacing is much wider than the measured width of each absorption feature (given by $\Delta\nu_{width} \otimes \Delta\nu_{molecule}$). In general it is better to ensure that the mode spacing is more than $n$-times the measured width of a typical transition (where $n$ is the number of modes in the comb). In this case it is expected that there should be some regions of the MUMAS spectrum with near total transmission and not too many occurrences of co-incidentally overlapping transitions.

This effect is illustrated in Figure 3.5, which shows three simulated MUMAS spectra: the result of the interaction of three different laser combs with the same gas sample. All three combs cover the same spectral bandwidth but have different mode spacings,

and hence number of modes. It can be seen from the resultant spectra that the laser comb with the wider mode spacing produces the least congested spectrum. This less congested spectrum will ensure that information about the gas sample is not lost, and that the MUMAS fingerprint is as distinct and characteristic as possible. In principle a wider mode spacing will give a better MUMAS spectrum, however, an upper limit on this parameter is enforced by the maximum stable scanning range of the laser, and the physical constraints on making the laser cavity shorter to produce a larger mode spacing.

The principal advantage of MUMAS over single mode absorption spectroscopy is its broad spectral coverage, therefore the output bandwidth of the multi-mode source is a very important factor. Wider spectral coverage will lead to more transitions being probed, providing more information about the properties of the measured gas. Therefore, it would seem that a greater bandwidth will produce better MUMAS spectra. In reality this requirement is not that simple as due to the constraints on mode spacing mentioned above, a wider bandwidth will lead to more modes in the comb.

As the number of modes, $n$, increases the reduction in total transmitted intensity caused by partial absorption of one laser mode will decrease as a function of $1/n$. This will lead to a reduction in sensitivity to any particular absorption feature, and hence an overall reduction in sensitivity to detection of that given species (this reduction is moderated if multiple transitions of that species are detected). Modes that probe regions of the spectrum completely devoid of absorptions have a particularly negative effect on the quality of the MUMAS spectrum as they will reduce the S/N ratio of the spectrum without adding any information. The number of modes should be chosen such that the comb has sufficient bandwidth to probe the required number of transitions but small enough that the absorptions are observable.

Therefore the ideal bandwidth of a laser for use in MUMAS is dependent on the mode spacing of the laser, the strength of molecular absorptions to be detected (a function

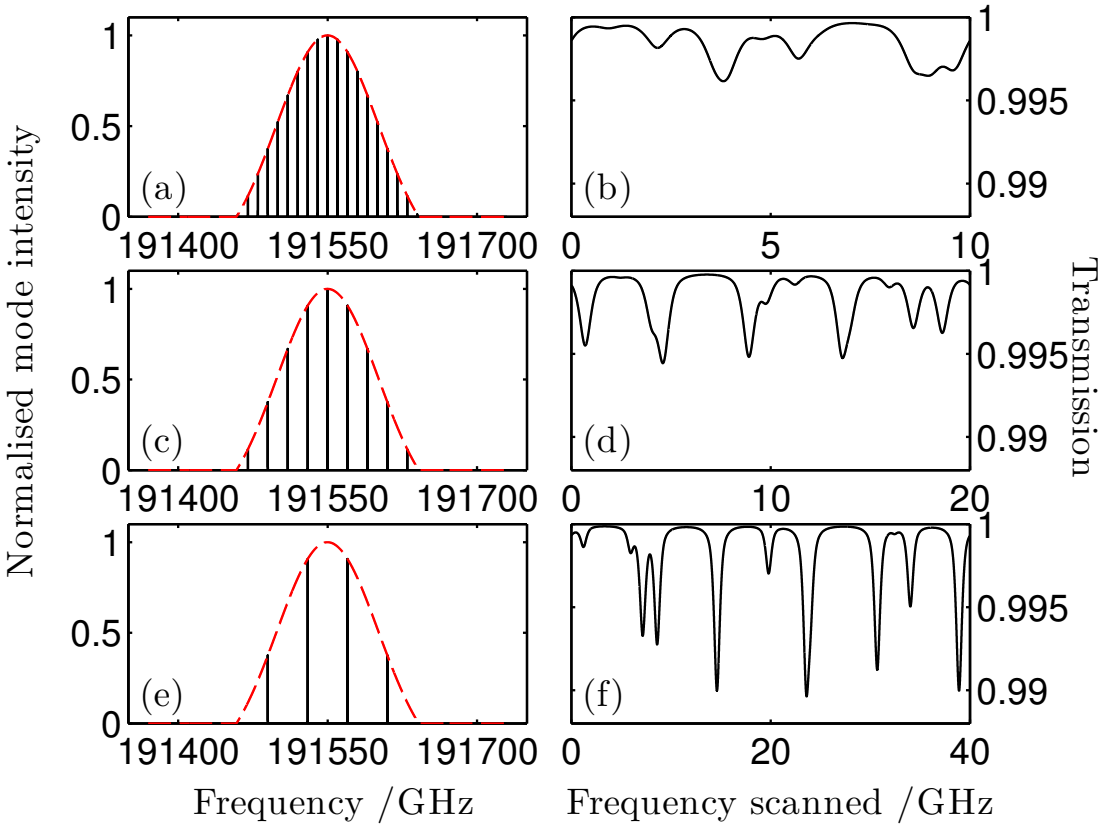


**Figure 3.5:** An illustration of the effect of mode spacing on the form of MUMAS spectra. Three laser combs are shown, (a), (c), (e), all having identical properties except the mode spacing, which is 10, 20, and 40 GHz respectively. The mode envelope function is marked in red for each case and from this it can be seen that all combs have the same spectral bandwidth. The interaction of each of these combs with the same gas sample is modelled (the sample contains 20 mbar of $N_2O$ buffered up to a total pressure of 0.1 bar with air). The resultant modelled MUMAS spectra are shown in (b), (d) and (e), where it can be seen that, everything else being equal, a wider mode spacing produces less congested and more distinctive MUMAS spectra.

of transition strength, absorber concentration, path length and broadening), and the spread of transitions in the spectral region. These properties change according to the sensing requirements of a particular application and so the precise numerical values of the bandwidth will also change.

In practice it has been found that a comb consisting of 5 – 15 modes generally offers a good trade off between spectral coverage and sensitivity to weak transitions. The lasers used in this work feature mode spacings of $\sim$ 20 GHz leading to an overall bandwidth in the range 50 — 200 GHz.

## 3.5 Conclusions

This chapter has discussed the principle of multi-mode absorption spectroscopy – MUMAS – the technique used for all work reported in this thesis. The theory of operation of the technique and the way in which experimental spectra are recorded have both been described. The factors determining the general shape and the specific form of MUMAS spectra have been explored, and it has been seen that these factors are properties both of the gas sample measured and also of the multi-mode laser used to perform the measurement.

The operation of the MUMAS model used to fit experimental spectra has been described. The original model – written during the course of previous work – has been modified and in large parts re-written to ensure that it continued to produce correct results in an efficient manner as the properties of the multi-mode lasers changed beyond original specifications. The changes made during the course of this work, and the necessity for these changes have been discussed in detail.

The general properties required of a multi-mode laser used to perform MUMAS have been discussed.

# Chapter 4

# Multi-mode laser development

## 4.1 Overview

This chapter reports laser development work with the aim of producing an improved multi-mode source for MUMAS. The motivation driving such development work is discussed first. The key requirements of a MUMAS laser are then considered and the improvements to the laser design needed to achieve these properties are discussed. Finally the ultimate design is introduced: a laser design capable of producing radiation with properties best suited to MUMAS.

## 4.2 Motivation

The MUMAS technique has been shown to be suitable for the simultaneous detection of multiple transitions: previous work has recorded spectra both with a diode laser operating at 760 nm, detecting transitions in the A-band of molecular oxygen, and with a solid-state laser in the near infrared region detecting transitions in the $\nu_1 + \nu_3$ overtone band of acetylene ($C_2H_2$) [6–8, 45]. Having demonstrated this, multi-species detection using multiple transitions from different species was the next goal. However, a suitable

multi-mode laser was required. The development work leading to such a multi-mode source is reported later in this chapter, but first the reasons leading to the choice of laser are discussed.

The near-infrared spectral region was an attractive target for testing the suitability of MUMAS for multi-species detection as this is where the $1^{st}$ overtone frequencies for the stretching modes of O-H, N-H and C-H bonds all lie. This provides a region containing overlapping bands of transitions present in many common molecules, enabling wide-ranging applications.

The global importance of telecommunications has led to extensive development of near-infrared (near-IR) laser sources, and in particular diode lasers, due to the optimum transmission window of optical fibres falling in this region. This has led to high-performance diode lasers being available cheaply as commodity items, however, such systems are typically optimised for single-mode operation by the integration of frequency selective elements into the structure such as in distributed Bragg reflector (DBR) and distributed feedback (DFB) lasers. Multi-mode operation is possible with Fabry-Perot (FP) devices but commercial devices are still typically optimised for single-mode operation. Multi-mode near-IR diode lasers have previously been tested and found to not have the required stability for MUMAS [45]. In addition the method by which a frequency scan is effected in diode lasers – injection current modulation – will modify the output power of the laser; in effect producing amplitude modulation (AM) as well as frequency modulation, adding additional complexity to the recorded signal.

Solid state lasers present an alternative and these systems have also seen development due to their potential for use in optical communications. Single-mode fibre lasers have been the focus of much attention, but short cavity free-space solid-state lasers have also been developed both in single-mode [82, 83] and multi-mode forms [84, 85]. The design of such lasers also provides an advantage for use in MUMAS as the cavities are usually

constructed of distinct elements, allowing the frequency scan of the laser modes to be effected by physically changing the cavity length. This has the advantage of not changing the gain properties of the laser and hence not overly changing the properties of the laser radiation in contrast to injection current modulation in diode lasers. The cavity length of short-cavity lasers previously reported results in a mode spacing useful for MUMAS (tens of GHz). Additionally, the short gain medium present in these lasers requires use of a high quality factor cavity to ensure the round-trip loss does not exceed the gain. This leads to the potential for narrow laser linewidths, in some cases tens of kHz [82].

One type of solid-state laser with particular potential for MUMAS is the Er/Yb:glass laser. These systems lase around 1.55 $\mu$m providing good access to the NIR region. The erbium transitions are subject to strong broadening, a result of crystal-field splitting in the glass host, enabling laser operation over a very broad region, up to 30 THz ($\sim$200 nm) [86]. This broadening also helps to support multi-mode operation. Finally, laser glass optimised for use in such systems is commercially available, making an Er/Yb:glass laser a viable proposition for development for use in MUMAS.

For these reasons a multi-mode Er/Yb:glass solid-state laser had previously been developed in the research group [8, 45]. This system was similar in outline to those reported by Laporta and co-workers [83, 87, 88] and consisted of a short cavity ($\sim$ 5 mm), formed between two concave mirrors with a centrally-positioned gain medium of phosphate glass co-doped with erbium and ytterbium ions. The mirrors were adjustable to facilitate cavity alignment and the output mirror was further mounted on a piezo-electric transducer to allow modulation of cavity length. The input coupler was optically coated for high reflectivity (99.9%) at $\sim$ 1530 nm and for high transmission ( 90%) at $\sim$ 980 nm; the output mirror had a reflectivity of 98 % at $\sim$ 1530 nm. The back surfaces of both mirrors were anti-reflection coated for the laser wavelength to reduce etalon effects.

The plane-plane erbium and ytterbium-doped phosphate glass disk was placed between

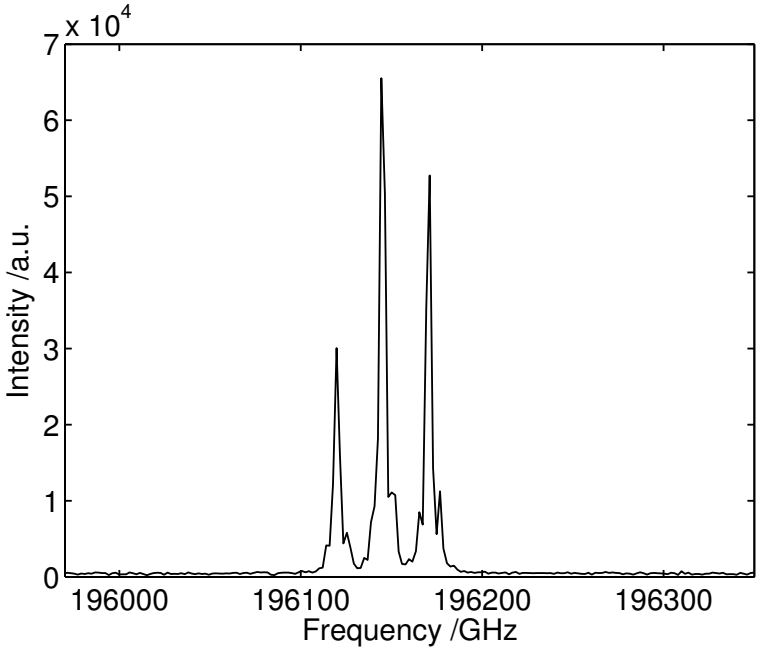


**Figure 4.1:** A typical output spectrum from the Er/Yb:glass laser developed for previous work.

the mirrors. To minimise parasitic lasing between the surfaces of this disk it was anti-reflection coated on both sides for the wavelength range 1500 — 1600 nm and held at an angle of $\sim 45°$ to the cavity axis. The beam from an InGaAs diode laser was reshaped and focused through the input coupler mirror into the gain medium. This end-pumping with $\sim$ 980 nm radiation produced continuous-wave multi-longitudinal-mode output around 1530 nm.

This system was used to detect acetylene and showed promise for use with MUMAS [8]. The output wavelength of 1530 nm allowed access to strong acetylene transitions ($S \approx 10^{-20}$ cm$^{-1}$/(molecule $\times$ cm$^{-2}$)). The beam contained tens of milliwatts of power spread over 3 — 5 modes with a mode spacing of 23.5 GHz. This gave an overall spectral coverage of up to 120 GHz resulting in MUMAS spectra containing multiple acetylene transitions. A typical output spectrum from the laser is shown in figure 4.1.

The piezo-electric transducer modulated the cavity length over a distance of order 1 $\mu$m, which resulted in the longitudinal modes scanning by $\sim 40$ GHz without mode-hops or other dynamic instabilities. This stable scan, over a frequency window exceeding the mode spacing of the laser, allowed it to be used to record MUMAS spectra.

Whilst this laser was capable of performing MUMAS, it did have several limitations, primarily relating to the reliability of the laser and its resilience to mechanical vibrations. Although this system was capable of producing modes exhibiting good stability, to do so required great care in the system alignment and an environment free from mechanical vibrations. The mode linewidth of this system, determined to be 0.7 GHz through fitting experimental MUMAS spectra, also limited spectral resolution. While the relative mode intensity during the scan was found to be stable and repeatable the mode envelope function $E(\nu)$ was of a complex shape, making modelling with a simple analytical function difficult. MUMAS spectra recorded with this laser also exhibited a periodic modulation ($\sim 3$ GHz period).

In order to investigate the suitability of MUMAS for multi-species detection several particular properties would be required from the multi-mode source. Most obviously, the laser would need to produce a comb of modes at such a wavelength and with sufficient spectral bandwidth to overlap with transitions arising from multiple molecules. In particular the spectral region 1550 – 1590 nm was chosen as a good target region as it contained bands of transitions of approximately equal strength from several small molecules including CO, $CO_2$, $N_2O$, and $C_2H_2$. In addition, this region also coincided with a broad plateau in the erbium gain curve, potentially allowing stable lasing on many modes simultaneously, giving a wide spectral bandwidth. A laser bandwidth target of 150 GHz or greater was chosen to give a good chance of detecting several transitions from multiple species.

Laser modes used for multi-species detection would need a narrow linewidth to allow

high resolution spectra to be recorded, and a mode spacing of around 10 – 50 GHz. In addition, repeatability of scanning behaviour was important to allow averaging of recorded spectra to increase the signal to noise ratio of the data, and a simple mode envelope was desired to simplify the modelling of experimental data. Finally, it was important for the laser to operate reliably and consistently to allow experiments to be performed with only modest environmental isolation.

It was not possible to find a commercial laser with these properties. The existing Er/Yb:glass laser was used as a basis for development of an improved multi-mode source. This system would require improvement of several key properties before it could produce spectra of the quality necessary for multi-species detection. In addition, development of an in-house laser would afford the flexibility for modification and customisation to suit particular applications.

## 4.3 Laser development

### 4.3.1 Overview

This section reports key elements of the laser development work undertaken to produce a stable multi-mode source for use with MUMAS. For the ease of communication, this work is presented using four strands, where each of sections 4.3.2 — 4.3.5 has the aim of improving a particular property of the existing laser; these sections discuss the required improvements for a laser property, before considering the underlying theoretical principles involved, and then report the development work that has been carried out. It should be noted, however, that in practice these development strands were interwoven, and many parts were investigated in parallel. The strands of development discussed in this section include: the reliability of the laser, the mode spacing and linewidth, the lasing wavelength and bandwidth, and the stability of the mode structure.

### 4.3.2 Reliability of operation

#### Requirements and objectives

To perform MUMAS measurements with a multi-mode laser it was important firstly for that laser to operate reliably and consistently. Specifically, it was important that the laser was not overly sensitive to environmental changes and disturbances, and that the mode structure was stable and repeatable. It was also considered to be beneficial for the beam produced by the laser to exhibit a simple Gaussian transverse profile.

When an Er/Yb:glass laser was initially constructed for this work, following the design used previously, it was found that it did not meet these simple requirements. Initially, it was extremely difficult to even achieve lasing. To improve on this, the laser design was considered in terms of the theoretical cavity stability, the cavity alignment, efficient pumping of the gain medium and the mechanical stability of the laser components.

#### Theory

Optical cavities can be described as stable or unstable; this property refers to whether a ray injected into the system with some initial position and angle relative to the cavity axis will stay within the cavity over many round trips. As such, cavity stability is determined by the properties and arrangement of optical elements in the cavity system, most importantly the curvature of mirrors and distance between them, and the effect of any other focusing elements.

A laser cavity can be understood by considering the properties of a Gaussian laser beam. Such a beam has a certain waist size and waist position. Two curved mirrors are placed onto this Gaussian beam, at any on-axis position either side of the waist, and if the curvature of the mirrors is precisely matched to the curvature of the wavefront then each of the mirrors will reflect the Gaussian beam exactly back onto itself. Providing the

mirrors are large enough to contain the beam (in practice substantially larger than the spot size to minimise diffraction losses) this will lead to the radiation in the beam forming a standing wave between the mirrors. The two mirrors form an optical resonator which can support not just this lowest order transverse mode (labelled $\mathrm{TEM}_{00}$) but also a family of higher-order transverse modes described by Hermite-Gaussian or Laguerre-Gaussian functions [89].

In practice it is useful to be able to determine whether any arbitrary laser cavity constructed from two mirrors, $M_1$ and $M_2$, having radii of curvature $R_1$ and $R_2$ and separation $L$, has a stable associated Gaussian mode. This can be done through a consideration of Gaussian optics.

The field distribution of a Gaussian beam is characterised by the beam waist, $\omega_0$. The transverse intensity distribution of the $\mathrm{TEM}_{00}$ mode in the plane containing the waist is given by

$$I(r) = e^{-2r^2/\omega_0^2} \tag{4.1}$$

where $r$ is the transverse distance from the beam axis and $\omega_0$ is the beam waist radius. There are several conventions for where the limit of the waist is drawn but the most common measures the radius to the point that the field intensity drops to a fraction $1/e^2 \approx 0.135$ of its centre value. A beam radius described in such a manner defines a circle containing 86 % of the power in the beam.

The intensity distribution of a Gaussian beam maintains its profile along its path and at a distance of $z$ from the beam waist has a beam radius $\omega(z)$ given by

$$\omega(z) = \omega_0 \left[1 + \left(\frac{\lambda z}{\pi \omega_0^2}\right)^2\right]^{1/2}. \tag{4.2}$$

The far-field divergence of a Gaussian beam is a cone of half-angle $\theta = \lambda/\pi\omega_0$.

The wavefront in a Gaussian beam is flat at the beam waist but either side of the waist, as the radiation converges or diverges, the wavefront exhibits curvature. This curvature is characterised by a radius of curvature $R(z)$ and this is given at any distance along the beam path by

$$R(z) = z\left[1 + \left(\frac{\pi\omega_0^2}{\lambda z}\right)^2\right]. \tag{4.3}$$

Equation 4.3 allows the theoretical stability of a cavity to be calculated. For a cavity to be stable each mirror needs to perfectly reflect radiation back to the mode waist, with exactly reversed wavefront curvature and propagation direction. For a cavity comprising two mirrors positioned at distances $z_1$ and $z_2$ from the (initially unknown) position of the mode waist, $\omega_0$, this situation can be represented by applying two conditions. Firstly the curvature of the wavefront at each mirror must match the curvature of that mirror (i.e. $R(z_1) = R_1$ and $R(z_2) = R_2$). Secondly, simply that the overall length of the cavity is the sum of the distance from each mirror to the mode waist ($L = z_1 + z_2$).

From these considerations it is possible to determine the parameters of the Gaussian waist in the cavity. This is normally carried out by means of the stability parameters $g_1$ and $g_2$, which are calculated in terms of the radii of curvature of the mirrors and the cavity length:

$$g_1 = 1 - \tfrac{L}{R_1}, \tag{4.4}$$

$$g_2 = 1 - \tfrac{L}{R_2}. \tag{4.5}$$

These stability parameters can then be used with Equation 4.2 to calculate the radius of the cavity mode waist in terms of the stability parameters:

$$\omega_0 = \left(\frac{\lambda L}{\pi}\right)^{1/2}\left(\frac{g_1 g_2\,(1 - g_1 g_2)}{g_1 + g_2 - 2g_1 g_2}\right)^{1/4}, \tag{4.6}$$

and the beam spot radii on the mirrors, $\omega_1$ and $\omega_2$, as

$$\omega(z_1) = \left(\frac{\lambda L}{\pi}\right)^{1/2} \left(\frac{g_2}{g_1(1-g_1g_2)}\right)^{1/4} \tag{4.7}$$

$$\omega(z_1) = \left(\frac{\lambda L}{\pi}\right)^{1/2} \left(\frac{g_1}{g_2(1-g_1g_2)}\right)^{1/4}. \tag{4.8}$$

The beam radii defined in equations 4.7 and 4.8 contain a fractional root of $(1 - g_1g_2)$. Real solutions for these parameters only exist when the product of $g_1$ and $g_2$ is less than one. This allows the stability condition for laser cavities to be expressed as

$$0 < g_1g_2 = \left(1 - \frac{L}{R_1}\right)\left(1 - \frac{L}{R_2}\right) < 1. \tag{4.9}$$

This inequality informs the choice of mirror curvature and the choice of separation of these mirrors to produce a stable cavity.

These calculations also have an impact on the pumping of a laser cavity. In order to most efficiently pump the laser, pump radiation should be focused to a waist of the same size as the transverse mode radius in the active medium. This ensures that the maximum amount of energy is coupled into the $TEM_{00}$ transverse mode, controlling oscillation of higher order modes.

Another consideration for the design of a laser cavity is the ease with which the cavity can be aligned in a practical system. A longitudinally pumped laser cavity constructed from two spherical concave mirrors, as described above, requires the careful alignment of three optical elements. Both mirrors must be adjusted relative to the pump beam, not just for two dimensions of tilt – pitch and yaw – but also for displacement in two dimensions across the beam axis – $x$ and $y$.

To align the system the input coupler must first be brought onto the axis of the pump beam and then the pitch and yaw adjusted to ensure that the pump focal waist will

efficiently fill the cavity waist. The output coupler then needs to be translated onto the same axis and the tilt optimised to form the cavity. In a short cavity it can be difficult to accommodate the necessary multi-dimensional actuators. Note that a cavity constructed from a concave input coupler and a planar output coupler remains theoretically stable but the output coupler no longer requires fine translational adjustment, simplifying this alignment procedure.

**Development**

One factor preventing lasing in initial designs was thought to be degradation of the laser diode used to optically pump the solid state system. Therefore this laser was replaced with a new 1 W diode (Roithner RLT981000G). Another problem was the diameter of the pump focal waist. The transverse mode profile in this system ($L = 5$ mm, $R_{1,2} = 10$ mm, $\lambda = 1535$ nm) was calculated to be a circle of diameter $\sim 80\,\mu$m, therefore a pump focus of approximately the same size was desired. This tight focus was challenging to produce due to the large and astigmatic divergence of the diode, and the long focal distance required to pump through the input coupler.

Initially the focus was produced with a bonded aspheric lens pair (Thorlabs C230260P, $f_{input} = 4.5$ mm, $f_{output} = 15.3$ mm, $\mathrm{NA}_{input} = 0.55$), however, while this was convenient and captured a large proportion of the highly divergent output of the diode laser it produced a focal region that was far too large and also rectangular in shape (due to the region being a magnified image of the diode laser facet).

The Er/Yb doped glass used in this solid state laser has the welcome property of producing visible fluorescence – observed as a dim green glow – when pumped with a moderately high intensity of 980 nm light. This emission is a result of frequency upconversion processes [90]. The green light from the pumped region was imaged using a video camera, generating an estimate of focal spot size. Several different reshaping

and focusing optics were investigated and the focal size measured for each. Simple beam reshaping was attempted using a cylindrical lens, but it was not possible to produce a beam of the required size and shape. To overcome this problem, the beam was coupled into a multi-mode optical fibre, producing a uniform, circular, beam profile, albeit with a reduction in power. A pair of high numerical aperture aspheric lenses (Thorlabs Al3026-B, $f = 26.0$ mm, NA$= 0.522$) were then used to image radiation emerging from the end of the fibre core (100 $\mu$m) to a spot of the same size in the cavity. This system produced a limited pump power due to inefficiency when coupling a beam of poor optical quality into a fibre. Finally, the bare diode was replaced with a fibre pigtailed version (Roithner RLCO-980-1000F), which had a 50 $\mu$m fibre core diameter, resulting in an imaged focal spot of diameter $\sim 60$ $\mu$m and good power density.

Cavity alignment of these solid state lasers also proved difficult. The initial cavity, shown in Figure 4.2(a) consisted of two concave mirrors with a slab of doped glass, anti-reflection (AR) coated for the output wavelengths and held at an angle ($\sim 10^{\circ}$) in the centre of the cavity. Attempts were made to align this system by monitoring the cavity fringes produced by a counter-propagating red beam produced by a helium-neon (HeNe) laser. Unfortunately the AR coating exhibited high reflectivity to red wavelengths, resulting in the cavity fringes being obscured. This prevented alignment and thus also laser action.

A new design of laser (shown in Figure 4.2b) was tested, comprising just two optical elements: a concave input coupler and a slab of doped glass, AR coated on one face and coated for 98 % reflectivity on the output face. This system allowed alignment using the HeNe and produced multi-mode radiation at 1.535 $\mu$m. In addition, the flat output coupler removed two dimensions of fine optimisation required to achieve alignment, as described in the section above. Unfortunately this laser produced a poor mode spectrum, thought to be due to the coupling of multiple sub-cavities, potentially arising from the

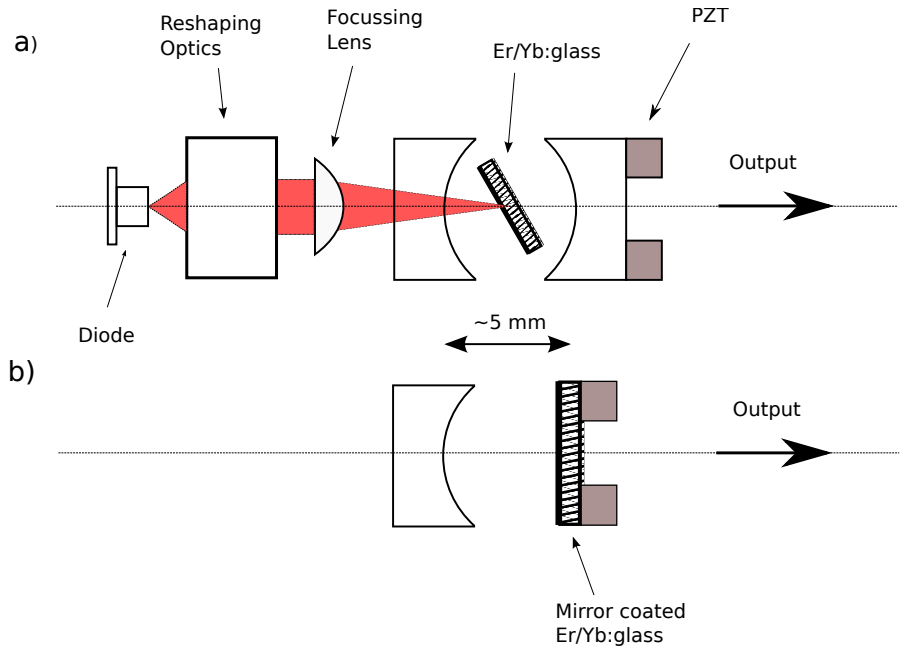


**Figure 4.2:** The micro-cavity laser construction. **(a)** The first laser constructed, with a cavity formed from two concave mirrors. PZT refers to the annular piezo-electric transducer used to change cavity length. **(b)** An alternative cavity design used in the second laser - formed from one concave mirror and a mirror coating on the doped-glass.

low but finite reflectivity of an AR coated surface normal to the cavity axis.

A new alignment procedure was then developed based on a hybrid of alignment with the HeNe laser, maximising pumping power density by monitoring visible emission, and iterative optimisation of below threshold NIR emission. The input coupler was first aligned onto the axis of, and normal to, the HeNe beam. The pump system was then brought onto this same axis. The glass and the output coupler (if separate elements) were then introduced on this beam axis and the pump laser switched on. The focal position of the pump light along the cavity axis was aligned into the centre of the gain medium by maximising the green fluorescence. Finally the sub-threshold fluorescence at $\sim 1.5$ $\mu$m was collected onto a photodiode, using a long pass filter to reject the far more intense pump radiation, and this signal optimised by adjusting each optical element in turn. This method typically resulted in laser action after several rounds of optimisation, provided

the starting positions were reasonably close to alignment. This alignment procedure was an important innovation, affording flexibility in the designs that could be aligned and tested.

### 4.3.3 Laser mode spacing and linewidth

#### Requirements and objectives

Both the mode spacing and mode linewidth are important properties of a multi-mode source used for MUMAS (as was described in Section 3.4). The mode linewidth has a direct impact on the spectral resolution achievable with MUMAS, as it would in any other form of direct absorption spectroscopy. The mode spacing does not have an analogue in single mode spectroscopy but the form of a MUMAS trace is sensitively dependent on this parameter. Although by differing mechanisms, both these parameters can have the effect of reducing the "sharpness" of a MUMAS spectrum if their values are not optimal – causing a reduction in the information that can be extracted from a spectrum.

The laser mode linewidth influences the absorption profile of each transition scanned over. The measured absorption profile is given by the convolution between the molecular transition linewidth and the laser mode linewidth. Therefore, a mode linewidth which is much narrower than the molecular transition width has the two-fold benefit of not limiting the resolution of the measurement and also not being an important factor in fitting a model to experimental data. Therefore it is key that this value is minimised, particularly for multi-species detection where it is be important to be able to distinguish closely lying absorption features.

The Er/Yb:glass laser used in previous work had a mode linewidth determined to be 0.7 GHz through the fitting of experimental MUMAS spectra. As molecular linewidths in this spectral region are of the order of 1 GHz for 0.1 – 1 bar of total pressure this

strongly limited the resolution of experimental measurements.

An ideal multi-mode source for MUMAS would not broaden the measured linewidth to a noticeable degree. An estimate of the desired linewidth can be made by noting that the linewidth of two Lorentzian profiles convolved together is given by adding the two component linewidths ($\Delta\nu_{A\otimes B} = \Delta\nu_A + \Delta\nu_B$). Therefore, assuming a Lorentzian mode profile, and that collisional broadening dominates other broadening mechanisms in the sample, a mode linewidth that is one hundredth of the transition linewidth will result in a measured linewidth $\sim 1\%$ wider than the actual linewidth – an acceptable situation. In the case that collisional broadening does not dominate and the molecular line profile is better described by a Voigt or Gaussian profile the effect of this laser linewidth broadening is lessened. This suggests that for molecular transitions of linewidth $\sim$1 GHz a laser linewidth of the order 10 MHz would not overly impact on the achievable spectral resolution.

The optimum mode spacing of a laser for MUMAS is harder to determine. In effect, this parameter sets the length of each of the spectral fragments that are added together to form the MUMAS trace. Closely spaced laser modes will lead to MUMAS spectra resulting from a short frequency scan and hence the linewidths of each transition will be proportionally wide relative to the length of the trace. In addition, for the same bandwidth, a comb with a small mode spacing will contain more modes hence leading to more spectral fragments being summed to produce the final spectrum. Both these mechanisms have the potential to reduce the clarity of the measured spectrum. The upper limit on this parameter is primarily determined by the physical constraints on cavity length but also the frequency range over which the laser can be made to scan in a stable manner. Simulations suggest that a mode spacing in the range 10 – 50 GHz would produce spectra of the required quality, with the upper limit being preferable.

**Theory**

The mode spacing and mode linewidth of a multi-mode laser are both strongly linked to the properties of the laser cavity.

If light circulating in a passive cavity (one with no amplification) is considered, it can be seen that interference will occur due to the overlap of reflected light. This will produce a comb-like transmission profile, the result of the survival of only light at frequencies such that the round-trip phase shift is an integer multiple of $2\pi$. This process leads to the concept of resonant cavity modes, the frequencies of which are given by the solution of the three dimensional wave equation. These can be expressed as [91]:

$$\nu_{q,l,m} = \frac{c}{2nL}\left[q + \frac{1+l+m}{\pi}\arccos(\pm\sqrt{g_1 g_2})\right] \tag{4.10}$$

where $q$ is the longitudinal mode number, $l$ and $m$ characterise the transverse mode properties, and $g_1$, $g_2$ are the stability parameters for the cavity. Modes arising from consecutive integer values of $q$ are termed longitudinal modes, and their spacing is the free spectral range (FSR) of the optical cavity, given by

$$\Delta\nu_{FSR} = \frac{c}{2nL}. \tag{4.11}$$

Each longitudinal mode has a set of associated transverse modes, corresponding to differing values of $l$ and $m$ for the same $q$ and are normally labelled $\mathrm{TEM}_{nm}$. Higher order modes ($n, m \neq 0$) have a complex spatial profile in the transverse plane. The mode structure of the cavity of a laser is described by accounting for the gain medium in the $nL$ factor.

The transmissive lineshape of a passive cavity can be derived from a consideration of the lifetime of photons within it [91]. For a given mode in a cavity the intensity at the

same point after a number of round trips, $m$ (i.e. at time $t_m = 2mL/c$) is

$$I\left(t_m\right) = \left[R_1 R_2 (1 - T_i)^2\right]^m I_0 \tag{4.12}$$

where $I_0$ is the initial intensity and $R_1, R_2$ the reflectivities of the two mirrors. $T_i$ is the fractional internal loss per pass due to mechanisms such as scattering and diffraction. The squared term is the internal loss per round trip. This can equally be represented in terms of the number of photons, $\phi$, in the cavity after $m$ round trips by setting $\phi\left(t\right) \propto I\left(t\right)$ to give

$$\phi\left(t_m\right) = \left[R_1 R_2 (1 - T_i)^2\right]^m \phi_0 \,. \tag{4.13}$$

If we assume that this holds true not only after complete round trips but at any arbitrary time, $t$, we can then write

$$\phi\left(t\right) \approxeq \phi_0 \exp\left(-\frac{t}{\tau_c}\right) , \tag{4.14}$$

where the photon lifetime in the cavity is then given by the time constant $\tau_c$, equal to

$$\tau_c = \frac{-2L}{c \ln[R_1 R_2 (1 - T_i)^2]} \,. \tag{4.15}$$

Therefore the time dependence of the electric field in a cavity mode can then be expressed as

$$E\left(t\right) = E_0 \, \exp[(-t/2\tau_c) + i\omega t] \tag{4.16}$$

where $\omega$ is the angular resonance frequency of the mode. The same temporal behaviour applies to the field of the radiation leaking out of the cavity mirrors. If a Fourier transform is taken of an electric field decaying in such a way we find that the power spectrum has a

Lorentzian lineshape with a linewidth (FWHM) given by

$$\Delta\nu_c = 1/2\pi\tau_c\,. \tag{4.17}$$

This gives the transmission spectrum of a passive cavity to be Lorentzian.

In an active laser cavity the same passive cavity mechanisms are at work, however, the linewidth profile is modified by the laser gain – the intensity dependent amplification results in narrowing of the lineshapes. An ultimate, quantum limit on the lower bound of the mode linewidth is imposed by zero-point fluctuations of the laser mode field. These are usually described in terms of random phase noise introduced by spontaneous emission. The mode linewidth in this limiting case is described by the Schawlow-Townes formula:

$$\Delta\nu_{osc} = \frac{\pi h\nu_{osc}\,(\Delta\nu_c)^2}{P_{osc}}\,\frac{N_2}{N_2 - N_1} \tag{4.18}$$

where $P_{osc}$ is the output power in the mode. The term $N_2/(N_2 - N_1)$ is the excess noise factor and accounts for the differing proportion of spontaneous emission in different laser modes.

In semiconductor lasers the Schawlow-Townes formula may determine the actual mode linewidth (albeit with a $(1 + \alpha^2)$ correction factor to account for an additional noise source that arises from the coupling between intensity and phase noise in these devices) [91]. In the case of solid-state lasers, however, the value given by this formula is extremely small (typically $< 1$ Hz) and is masked by sources of "technical noise" such as mechanical vibrations, acoustic noise and thermal drift leading to small changes in cavity length or alignment.

**Development**

To produce a laser with mode spacing in the range 10 — 50 GHz required an optical cavity length of 15 — 3 mm. The design and construction of cavities of this short length presents challenges, particularly as some of the available cavity length is taken up by the concave nature of the cavity mirrors (approx 1 mm per mirror) and more by the gain medium (of physical length 1 — 2 mm giving an optical length of 1.5 — 3 mm for a refractive index, $n = 1.5$). The previous erbium laser had a mode spacing of 23.5 GHz, suggesting that the length of the cavity employed in this design would not need to be changed. Therefore this parameter did not require active development but rather needed to be maintained through iterations of different prototype laser designs.

The mode linewidth of the previous laser (determined to be $\approx 0.7$ GHz) required a marked reduction to allow high resolution spectra to be recorded. The linewidth in this previous laser was thought to be limited by the optical flatness of the doped glass used [45]. The glass disk was not optically polished and thus the quality of the cavity was limited by the flatness finesse rather than the reflection finesse. This suggested that large improvements in this parameter could be achieved by simply ensuring that the surfaces of the glass used in the laser were polished to an optical standard.

New laser glass was ordered with surfaces polished to a good optical quality (scratch/dig 10/5, $\lambda/10$). This glass was also AR coated ($< 0.1\%$ R for 1540 — 1580 nm) to reduce reflection losses. These changes reduced the mode linewidth dramatically to a value below 10 MHz (measurement limited by the instrumental linewidth of the spectrum analyser used to make measurement), leading to the principal linewidth limitation being mode frequency jitter over the timescale of spectrum recording rather than instantaneous mode linewidth.

### 4.3.4 Wavelength and bandwidth of the laser comb

#### Requirements and objectives

To enable multi-species detection with MUMAS, it was important that the laser comb overlapped with transitions arising from multiple species. Therefore the envelope function defining the comb required a suitable central frequency and bandwidth.

In the design of the laser previously used for spectroscopy, no attempt had been made to choose the wavelength of operation leading to lasing near 1530 nm, at the peak of the erbium gain curve. The erbium gain drops off rapidly either side of the peak and therefore radiation was only produced over a relatively narrow spectral region. To produce a comb of greater bandwidth it was important to promote lasing in a flatter region of the gain curve, such as between 1540 nm and 1580 nm.

Transition information from the HITRAN database [76] was used to investigate the possibilities for multi-species detection within this flatter gain region (see Figure 4.3). A window was identified, between 1563 and 1575 nm, where transitions arising from at least three molecules were found with line strengths expected to give similar, and measurable, absorptions. In this region $N_2O$ and CO transitions were found with line strengths of the order $10^{-23}$ and $10^{-24}$ $cm^{-1}/(molecule \times cm^{-2})$ respectively. At the shorter wavelength end of the window $C_2H_2$ transitions were present with strengths of $10^{-24}$ and at the longer wavelength end $CO_2$ transitions were present of strength $10^{-23}$ $cm^{-1}/(molecule \times cm^{-2})$. The preceding species were readily available from commercial suppliers and were of interest for environmental, medical or combustion monitoring, making this region an attractive target.

In this target region the most widely spaced transitions arise from CO and are approximately 90 GHz apart. This suggested a minimum laser comb bandwidth (i.e. total coverage) of around 120 GHz would be needed for laser modes of appreciable

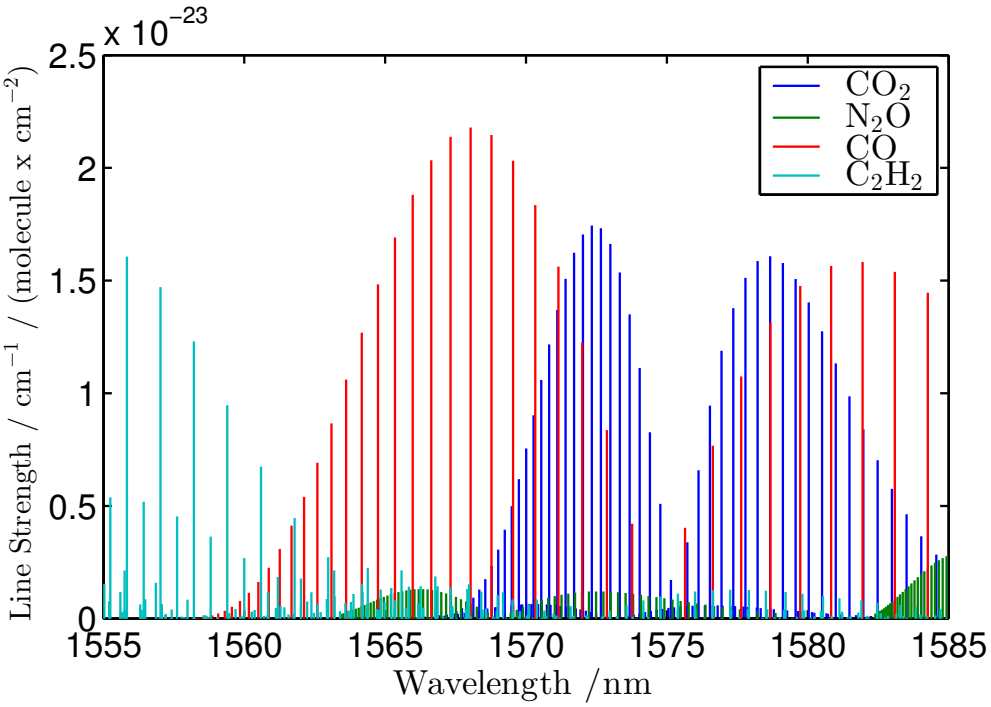


**Figure 4.3:** Transitions of selected species between 1555 and 1585 nm from the HITRAN database.

intensity to interact with two such transitions, and that a bandwidth greater than 180 GHz would ensure that two CO transitions could be probed without fine control being required over the central wavelength of the comb.

### Theory

To design a laser with these tailored properties it is important to consider the operating mechanisms of the Er/Yb laser. In the Er/Yb:glass laser, radiation is produced by transitions between the energy levels of erbium ions. The gain medium consists of $Er^{3+}$ ions doped as an impurity into a phosphate glass matrix (along with an ytterbium ion co-dopant which acts as a pump sensitiser, aiding pumping efficiency). For the work described here a commercial laser glass is used (Kigre QX/Er, $[Er^{3+}] = 1.46 \times 10^{20}$ ions

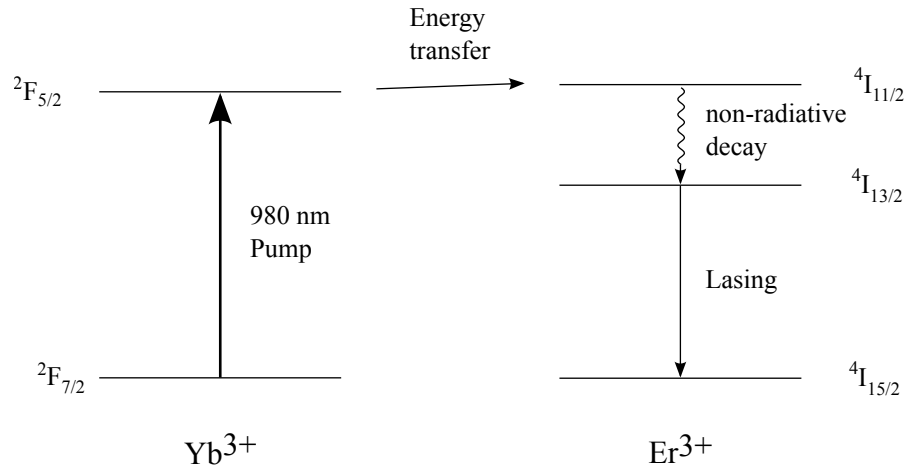


**Figure 4.4:** A simplified energy level diagram for the Er/Yb system. Details of the processes shown are found in the text.

$cm^{-3}$, $[Yb^{3+}] = 1.9 \times 10^{21}$ ions $cm^{-3}$). The energy level scheme for the Er/Yb laser is complex with many contributing processes. However, a qualitative understanding can be gained from analysis of a simplified system as presented in Figure 4.4. More details are provided by Taccheo *et al.* [87].

When operated around 1550 nm the erbium laser behaves as a three-level lasing system [87]. Pump radiation at 980 nm promotes $Yb^{3+}$ ions from the $^2F_{\frac{7}{2}}$ ground state to the $^2F_{\frac{5}{2}}$ excited state (direct pumping of erbium can be neglected due to its much lower rate). This excitation is then resonantly transferred to a closely matched $Er^{3+}$ state which rapidly decays to the long lived $^4I_{\frac{13}{2}}$ state (lifetime ∼8 ms). Lasing action occurs from this state to the $^4I_{\frac{15}{2}}$ ground state. The generation of the population inversion necessary for lasing is aided by the long lifetime of the upper state, however, the large thermal population in the lower (ground) state means that at least half the population must be transferred to the upper state.

The Er/Yb gain medium provides gain over a very broad region. Stark splitting arises from the local electric field experienced by the ions in the glass matrix, and causes the upper and lower laser levels to be split into manifolds of 14 and 16 sublevels respectively,

resulting in a total of 56 laser transitions. These transitions are then subject to both homogeneous and inhomogeneous broadening mechanisms. The homogeneous broadening arises from limited lifetime effects, a result of rapid phonon-induced transitions between Stark components within a given multiplet [86]. The inhomogeneous effects are due to variations in the local electric field experienced by each ion, themselves a result of the amorphous glass structure. Overall, these interactions give rise to a strongly broadened emission spectrum spread over tens of THz. The relative weight of the broadening mechanisms is still open to debate, and can vary strongly with host material and temperature, however, the behaviour observed generally suggests predominantly homogeneous effects [85, 86, 92].

The broadening mechanisms operating in the gain medium allows understanding of the multi-mode operation of the Er/Yb laser. Given a basic understanding of lasers, it might be expected that they would generally operate on multiple longitudinal modes, since the frequency separation of modes is usually much smaller than the width of the gain profile, meaning that several, often very many, cavity modes fall within the gain region [91]. Even the micro-cavity laser described in this chapter has a mode separation (of order 10 GHz) far narrower than the width of the gain profile (10 THz). However, further analysis of laser operation predicts that in fact a homogeneously broadened system will always feature single-mode operation. This result is reached by considering the gain as a function of frequency. As pumping power is slowly increased, gain will grow until the mode nearest the peak reaches the threshold for lasing (the condition of its round-trip gain equalling round-trip loss). At this point the gain at the frequency of the lasing mode will stop growing. Due to the presence of purely homogenous broadening, the shape of the gain profile cannot change so gain at all other frequencies will also stop increasing, preventing any other mode achieving threshold. Thus one mode extracts energy equally from all excited molecules of the gain medium.

The situation is quite different for the case of an inhomogenously broadened system where each mode can extract energy from a different sub-group of molecules or ions in the gain medium (for example velocity sub-classes in a gas laser or ions in different environments in a solid state laser). In this case, as the pumping power is increased the gain at each mode frequency will be clamped at the threshold value but if the mode separation is greater than the inhomogenous linewidth then the gain between modes is free to increase – a phenomenon known as spectral hole-burning.

In reality multi-mode operation is often observed in homogenously broadened lasers. This is the result of each longitudinal mode corresponding to a well defined standing wave pattern in the gain medium. As such, energy can only be extracted from the gain medium in regions where this standing wave has a non-zero intensity, and therefore regions of unused gain remain at the spatial location of each node of the standing wave. This situation is described as spatial hole-burning. Lasing action may then be supported on multiple cavity modes if the spatial intensity pattern of their standing waves in the gain medium has sufficient phase difference to allow gain to be obtained from separate spatial regions.

In an Er/Yb laser constructed from phosphate glass, such as the Kigre QX/Er used for this work, multimode operation typically occurs spontaneously unless it is intentionally suppressed by wavelength selective cavity elements. Although the precise balance of broadening mechanisms in this system is unknown this multimode operation is generally ascribed to spatial hole-burning [87].

**Development**

Due to the broad emission range of Er/Yb doped phosphate glass, laser operation can be achieved across a broad spectrum. In any particular erbium laser the output wavelength and bandwidth is the result of the balance of gain and loss in the laser cavity at different

frequencies, and this balance can be tipped towards a particular wavelength by factors such as pumping intensity or the wavelength response of optical elements in the cavity.

The effect that the intensity of optical pumping has on the output wavelength of a laser can be better understood by modelling the main wavelength-dependent gain and loss process occurring in the laser cavity - the absorption and emission by the erbium ions in the laser glass – for different proportions of population in the upper state. A gain cross-section can be defined that represents the net gain or loss at a particular wavelength [93]:

$$g(\lambda) = \beta\sigma_{em}(\lambda) - (1-\beta)\sigma_{ab}(\lambda) \ , \tag{4.19}$$

and subsequently used to understand the potential wavelength range of the laser and also the favoured output wavelength. In this equation $\beta$ is the proportion of population in the upper lasing state, and $\sigma_{em}$ and $\sigma_{ab}$ are the emission and absorption cross-sections of the erbium ions in the doped glass. If the analytical forms of the absorption and emission cross-section provided by [94] are used it is simple to model the gain cross-section for Er/Yb doped phosphate glass, as shown in Figure 4.5.

These gain cross-section curves illustrate the wide wavelength region of positive gain and also the sensitivity that the peak wavelength shows to perturbation. One way to take advantage of this sensitivity is to engineer the wavelength response of the various laser components to tune the lasing wavelength to a desired value.

An intra-cavity interference filter was tested in the course of previous work and was found to produce some tunability of the output wavelength [45]. A different approach is to use cavity mirrors with carefully tuned spectral reflectivity profiles. Mirrors with high peak reflectivity and arbitrary wavelength reflectivity response can be produced using multi-layer dielectric coatings. Initial work on this project used mirrors coated for broadband reflectivity across the erbium emission spectrum, with the expected result

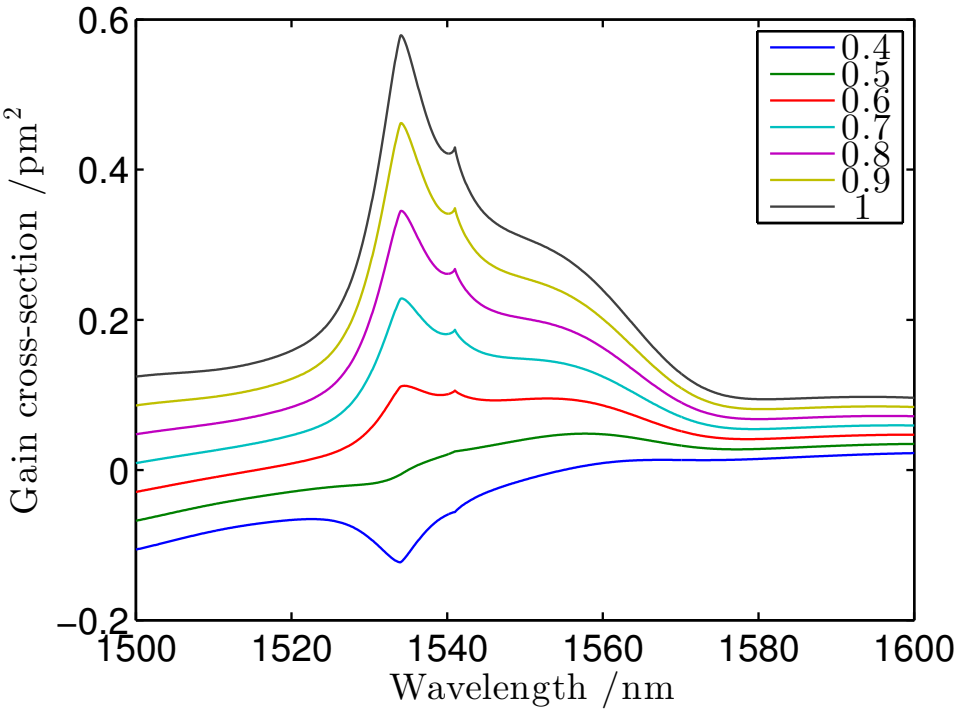


**Figure 4.5:** Modelled gain cross-sections for an Er/Yb phosphate glass over a range of values of $\beta$, the population ratio between upper and lower lasing levels.

that radiation was produced near to the peak of the erbium gain profile. To produce radiation at the wavelengths desired for multi-species detection, custom output coupler coatings were commissioned with the reflectivity peak shifted to longer wavelengths. When coupled with a broadband, high-reflectivity input coupler this shifted the laser comb centre wavelength to around 1565 nm, within the desired range.

Parallel work in the group focused on simultaneous detection of CO and $CO_2$ [95]. The ratio of these gases in combustion exhaust gases gives insight into the completeness of combustion. A laser constructed from the same output coupler and an input coupler which only achieves high reflectivity for wavelengths longer than 1567 nm shifted the output wavelength to 1571 nm – within the region of overlap between the $CO_2$ $3\nu_1 + \nu_3$

and CO $3\nu$ bands.

The comb bandwidth of a multimode Er/Yb laser is the result of the interplay between effects such a spatial hole burning, the wavelength dependence of both the gain in the erbium glass and the reflectivity of the cavity mirrors, and as such it is challenging to predict the bandwidth a particular laser design. Shifting the output wavelength to a flatter part of the erbium gain curve resulted in the production of a broader multimode comb, however, early designs of the Er/Yb laser suffered from coupled cavity interference leading to a complex shaped envelope function (see Section 4.3.5). Once this effect had been removed a comb was produced containing 8 — 12 modes spread over approximately 180 GHz.

### 4.3.5 Comb structure and temporal stability

#### Requirements and objectives

The structure of the laser comb and its temporal stability are both key properties of a multi-mode source used for MUMAS. It is essential that the laser produces a comb of laser modes that are defined by a simple envelope to allow the modelling of the laser output. The temporal properties of the laser output are also important and it is vital for the mode structure to not just be stable and repeatable but also to scan in a manner that is predictable and consistent; these requirements are closely related – and the first is a prerequisite of the second – and they can be termed *static stability* and *scanning stability* respectively.

The previous laser could be made to operate with reasonable static stability, however to do so required extremely careful cavity alignment. In addition this stability was not resistant to acoustic and mechanical vibrations, making the laser difficult to use for spectroscopy. For this work it was necessary to improve this behaviour.

During scanning, the output of the previous laser was modulated by a periodic fine structure (period ∼3 GHz) and the mode envelope function was found to be of a complex shape. It was hoped to improve these properties to allow more accurate modelling of experimental data. In addition, early prototypes of lasers developed during this work showed very poor comb structure and scanning stability. Even when a stable and well structured comb could be produced this was often found to be completely destroyed by scanning the cavity length, making the laser unsuitable for MUMAS.

### Theory

The comb structure problems were thought to be caused by optical feedback or coupled cavity resonances. This feedback can arise from reflections from surfaces either within or outside the laser cavity and leads to the imposition of additional phase requirements on the radiation within the cavity, resulting in a laser comb with a complex shape.

These optical feedback effects can also have a negative effect on the temporal stability of the laser comb. The coupling together of two cavities heightens the sensitivity of the laser to environmental disturbances. Any small changes in the length of either cavity, such as those that may arise from mechanical vibrations or acoustic noise, can then result in dramatic changes in the structure of the comb. This effect can be even more pronounced when the cavity length is intentionally changed to scan the laser modes.

The mechanical stability of the laser is important even in the absence of optical feedback. Changes in the cavity length due to vibrations – even on the scale of nanometers – will cause the frequency of the laser modes to jitter, reducing the quality of recorded spectra.

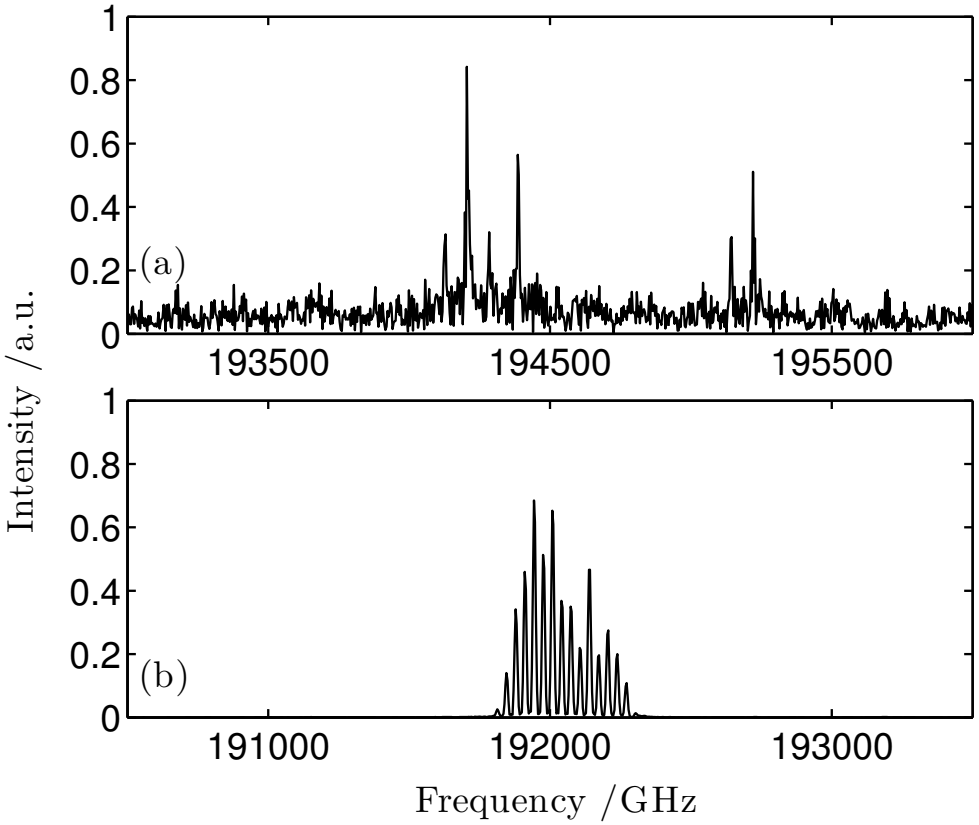


**Figure 4.6:** The output spectrum of two prototype laser designs recorded using a Bristol Instruments 721-B spectrum analyser. **(a)** Spectrum of the laser shown in Figure 4.2(b) **(b)** Spectrum of a laser constructed from two wedges.

### Development

To counter these effects it was first important to remove any possible source of optical feedback from the laser. Laser designs similar to the previous design shown in Figure 4.2(a) with either a concave-planar or planar-planar output coupler were found to suffer due to reflections from the back surface of the output coupler (despite an AR coating). A similar effect was also seen with the design shown Figure 4.2(b), where the front surface of the mirror coated glass slab was thought to cause intracavity reflections despite it, again, being AR coated. A typical output spectrum of this laser illustrating the poor mode structure is plotted in Figure 4.6(a).

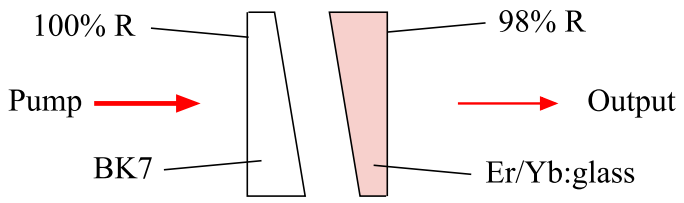


**Figure 4.7:** Schematic diagram showing a laser constructed from complimentary wedges of BK7 and Er/Yb doped glass. The cavity is formed between the mirror coated rear surfaces of the wedges.

To remove these effects, a laser was designed based on wedging the front surface of the doped glass to remove any reflections from the cavity. This wedge was mirror coated on the rear surface to be used as an output coupler. A laser cavity made up from such a wedge and using a complementary wedge of BK7 glass as the input coupler (see Figure 4.7) was found to have a vastly improved mode structure (Figure 4.6(b)).

It was also important to increase the mechanical stability of the laser cavity. The previous design and early prototypes made for this work held the laser mirrors separately on standard mirror mounts. When the doped glass was placed in the centre of the cavity, this was suspended from a third mounting structure. The mirror mounts were swapped for commercial high stability mounts without apparent improvement. Therefore lasers were designed with the optical components physically held together in a stack, within a monolithic block of aluminium. This removed the possibility of the components moving independently when subjected to mechanical vibrations, and also created a sealed air volume within the laser cavity reducing the impact of acoustic noise. In combination with wedging the doped glass, this led to large improvements in the static stability of the laser modes.

Upon scanning the cavity length, however, the stable mode structure of this laser was found to rapidly fluctuate. It was hypothesised that this could be due to weak optical

feedback from a surface outside the laser. The scanning of the cavity length could cause this reflected light to interfere with radiation within the laser cavity in a time-varying manner. Therefore, an optical isolator was included close to the output side of the laser. This addition improved the scanning behaviour and resulted in a laser comb capable of scanning over a full mode spacing in a stable and repeatable manner.

This improvement in scanning stability allowed an additional effect to be noticed. A transient reduction in output power was observed, occurring at a consistent position in the scan of the multi-mode laser. This effect was found to be sensitive to the positioning of the pump laser fibre. It was suspected that this behaviour was due to pump radiation being reflected from the back surface of the input coupler, weakly coupled back down the fibre, and feeding-back into the diode laser. To reduce this problem the output coupler was tilted, moving the cavity axis such that the pumping axis was no longer normal to the back surface of the input coupler.

## 4.4 Final laser design

The elements of this development work were brought together to produce a final laser design with the desired properties for multi-species detection. The design and properties of this laser are described below.

### 4.4.1 Design

The laser has a simple, robust structure based on a monolithic barrel-shaped design – the components are stacked in a cylindrical assembly within the bore of a single piece of aluminium (Figure 4.8). This arrangement gives good mechanical stability due to the arrangement of optical elements, pressing directly on one another. It also forms a sealed air volume around the cavity, excluding acoustic vibrations. The laser uses

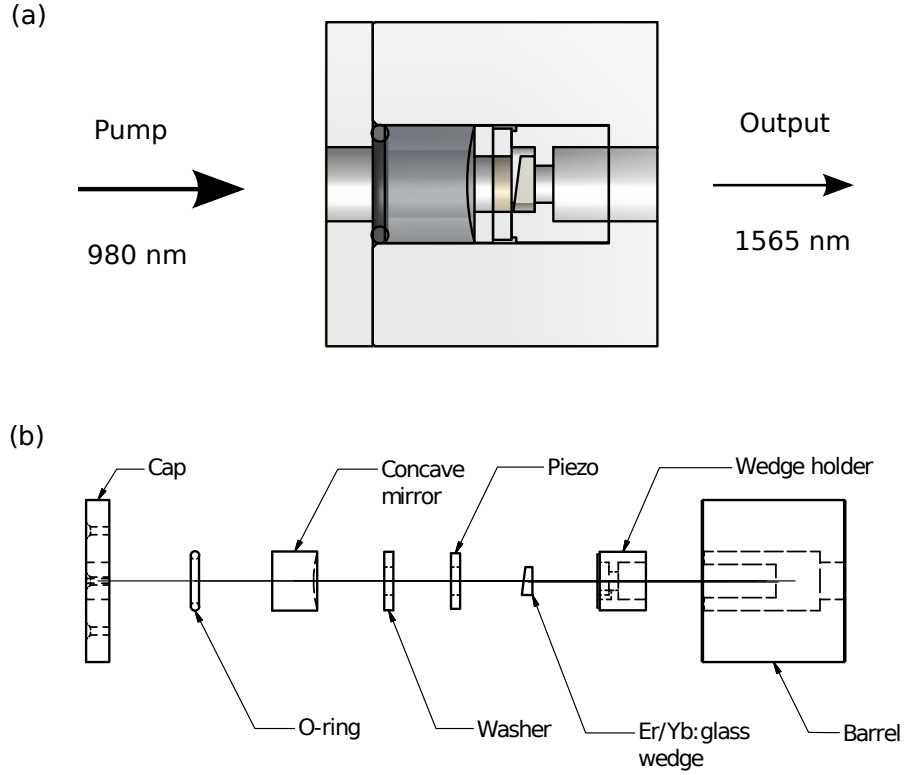


**Figure 4.8:** A diagram of the final laser design. The optical and mechanical components are arranged in a stack that sits in a bore within a cylinder of aluminium. The cavity is pumped in a longitudinal manner through the input coupler, details shown in Figure 4.9. **(a)** The assembled laser, showing the position of all components. **(b)** An exploded diagram of the laser identifying all parts.

an Er/Yb-doped phosphate glass chip (Kigre QX/Er) as the active medium, the front surface of which is wedged at 7.6° to avoid coupled cavity inference.

The laser cavity is formed between a concave spherical mirror (of diameter 12.7 mm and radius of curvature 25 mm), and the planar output face of the wedged glass chip (face size 6 mm x 6 mm). The curved mirror was custom coated in-house to produce high reflectivity over a broad region centred on the laser wavelength. The external face of the wedged chip was custom coated with a broadband coating with reflectivity 98% over the range 1538 — 1580 nm, centred around 1550 nm. The back face of the input coupler

was AR coated for pump and laser wavelengths. The internal face of the wedge was also coated with an anti-reflection layer to give a reflectivity $< 0.1\%$ at laser wavelengths to further discourage sub-cavity formation.

This design of laser cavity has the benefit of resulting in automatic optical alignment – the concave mirror and wedge are held at the correct relative transverse position, separation distance, and relative angle by the mechanical components. Provided that these parts are made to a good degree of precision and assembled carefully, the optical elements will produce the desired optical cavity. This simplifies the set up of the laser system as the only adjustments then necessary to achieve lasing are to optimise the focal position and input angle of the pump radiation. The absence of adjustable mirror mounts also increases mechanical stability and reduces the potential for alignment drifts.

Figure 4.9 shows the the way in which optical pumping is provided by the fibre-coupled output of a diode laser (Roithner, RLCO-980-1000-F) at 975 — 980 nm. The pump light emerging from a 50 $\mu$m fibre core is imaged using two large diameter aspheric lenses ($\phi = 30$ mm), through the curved mirror and to a spot of diameter $\sim 60$ $\mu$m in the Er/Yb:glass. This diameter was chosen to approximately match the the transverse mode diameter of the resonator.

The laser modes are scanned using an annular piezo-electric transducer, PZT, placed between the laser mirrors (Noliac CMAR03). This transducer alters the cavity length by approximately 1 $\mu$m, pressing the curved mirror against a compressible "O-ring". In this way, the cavity modes can be tuned in frequency to effect the MUMAS spectral scan. An optical isolator (Thorlabs IO-2.5-1550-VLP) provides $\sim$35 dB of isolation, removing the disruptions to mode structure caused by back reflections.

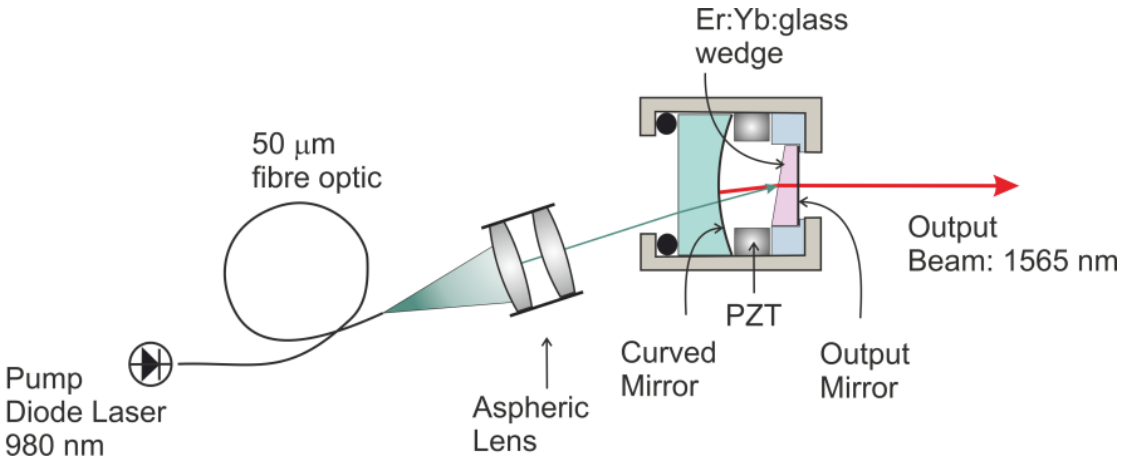


**Figure 4.9:** A diagram illustrating the method of optical pumping in this laser. A fibre-coupled 980 nm diode laser is aligned into the laser cavity at an angle to allow for refraction at both surfaces of the input coupler and the front surface of the wedge. The pump radiation is tightly focused into the active medium through the use of two large diameter aspheric lenses in an imaging arrangement. In this way the power density necessary for lasing is achieved and higher order transverse modes are suppressed.

### 4.4.2 Characterisation of properties

The properties of this laser were measured to verify performance. The efficiency curve for this laser is shown in Figure 4.10. It can be seen that the threshold of laser action occurred at around 295 mW of pump power, and the slope efficiency was ∼19 %, both within the ranges reported previously [87, 93]. A typical pump power of 500 mW produced a laser power of ∼40 mW. The output was collimated using a 75 mm focal length lens to form a beam with an approximately Gaussian intensity distribution and 2 mm diameter. The full-angle beam divergence was measured to be 1.4 mrad which compares well with the estimated diffraction limit of 1.0 mrad.

The output spectrum of the laser was recorded using a 1 m Czerny-Turner grating spectrograph with a grating of 1000 lines/mm and an InGaAs CCD array (Andor DU490A-1.7). The result, shown in Figure 4.11(a), shows a stable, multi-mode output with a mode spacing of 18.39 GHz (corresponding to an optical cavity length of 8.15 mm), centred

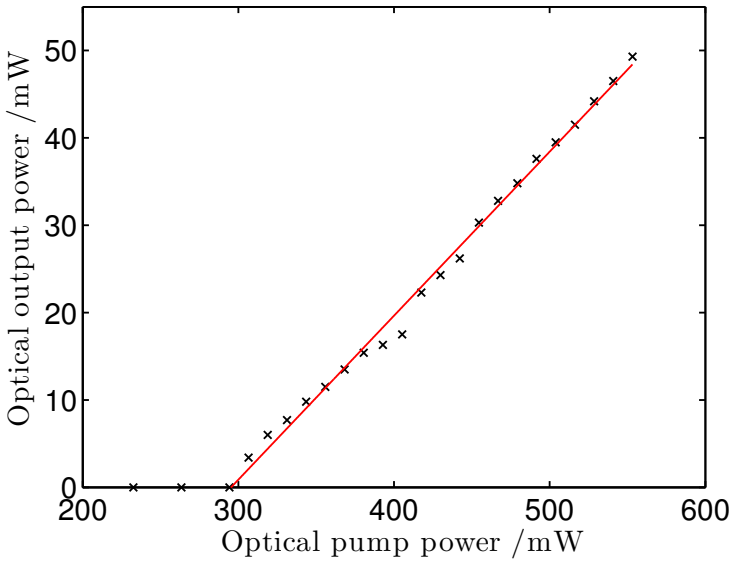


**Figure 4.10:** Measured efficiency curve for the final laser design. Laser action occurs for pumping powers above the threshold pump power of ∼295 mW. The slope efficiency above this point was determined to be ∼19% using a linear fit.

around 1565 nm. A comb of 10 modes was typically produced, covering a bandwidth of ∼180 GHz (1.4 nm). Measurements of mode linewidth were limited by the resolution of the available spectrum analyser to $< 10$ MHz. The laser was capable of scanning the modes within the comb in a stable and repeatable manner. The longitudinal modes could be scanned over a frequency range corresponding to $\sim 3$ times the mode spacing ($\sim$ 60 GHz) with a repetition frequency of 1 — 10 Hz, limited by the high-voltage amplifier driving the piezo transducer (Noliac NDR6110). The scanning of the laser modes is plotted in Figure 4.11(b).

The flexibility of the design enabled different lasers to be constructed with differing mode spacings or output wavelengths. The use of an alternative mounting cylinder allowed combs to be produced with mode spacings in the range 10 — 40 GHz. Two such combs are shown in Figure 4.12 and compared to the "base" model already described.

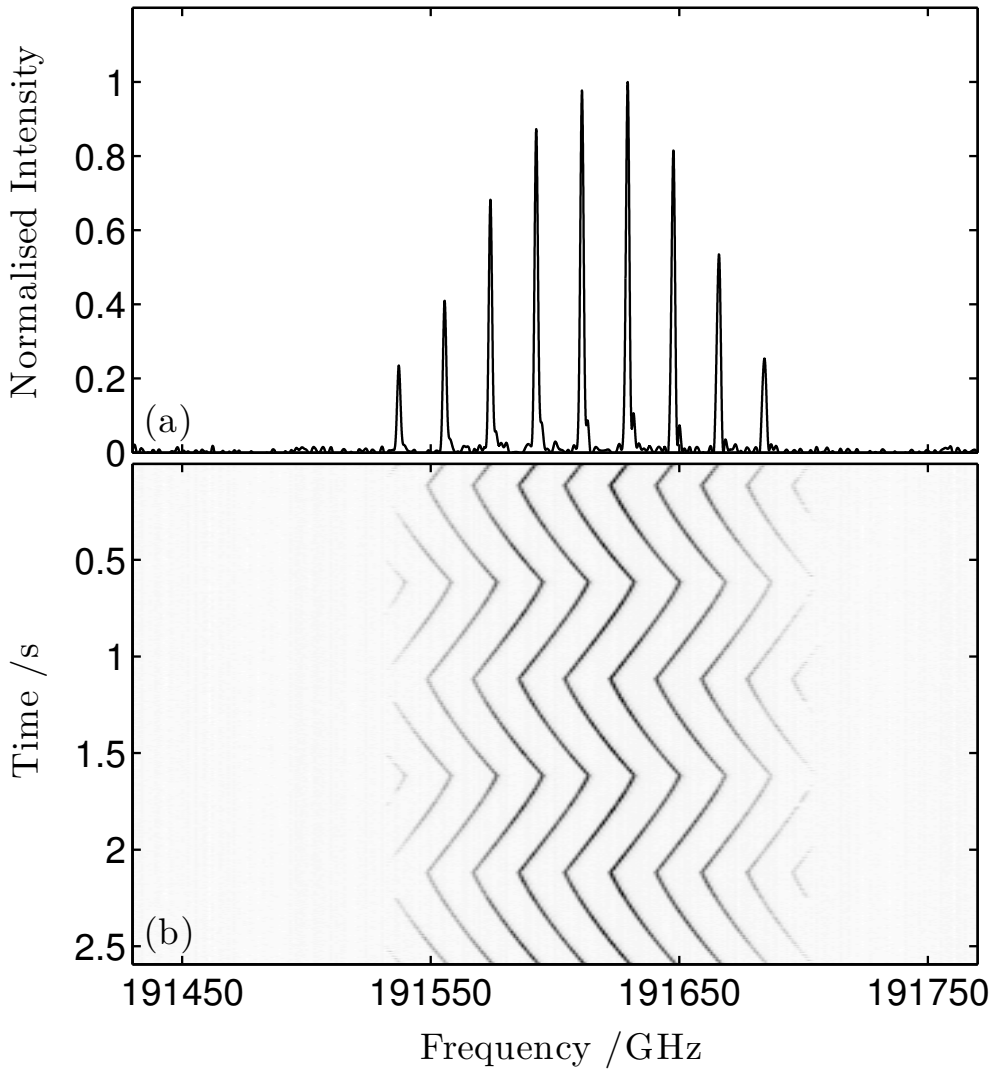


**Figure 4.11:** Spectrum of the Er/Yb glass microlaser recorded with a 1 m spectrograph and a CCD array detector. The multi-mode comb is centred about 1565 nm, has a mode spacing of 18.39 GHz and a spectral width of approximately 180 GHz (1.4 nm). The linewidth of the laser modes has been broadened by the instrument resolution limit. **(a)** The static comb. **(b)** The frequency scan of the laser modes.

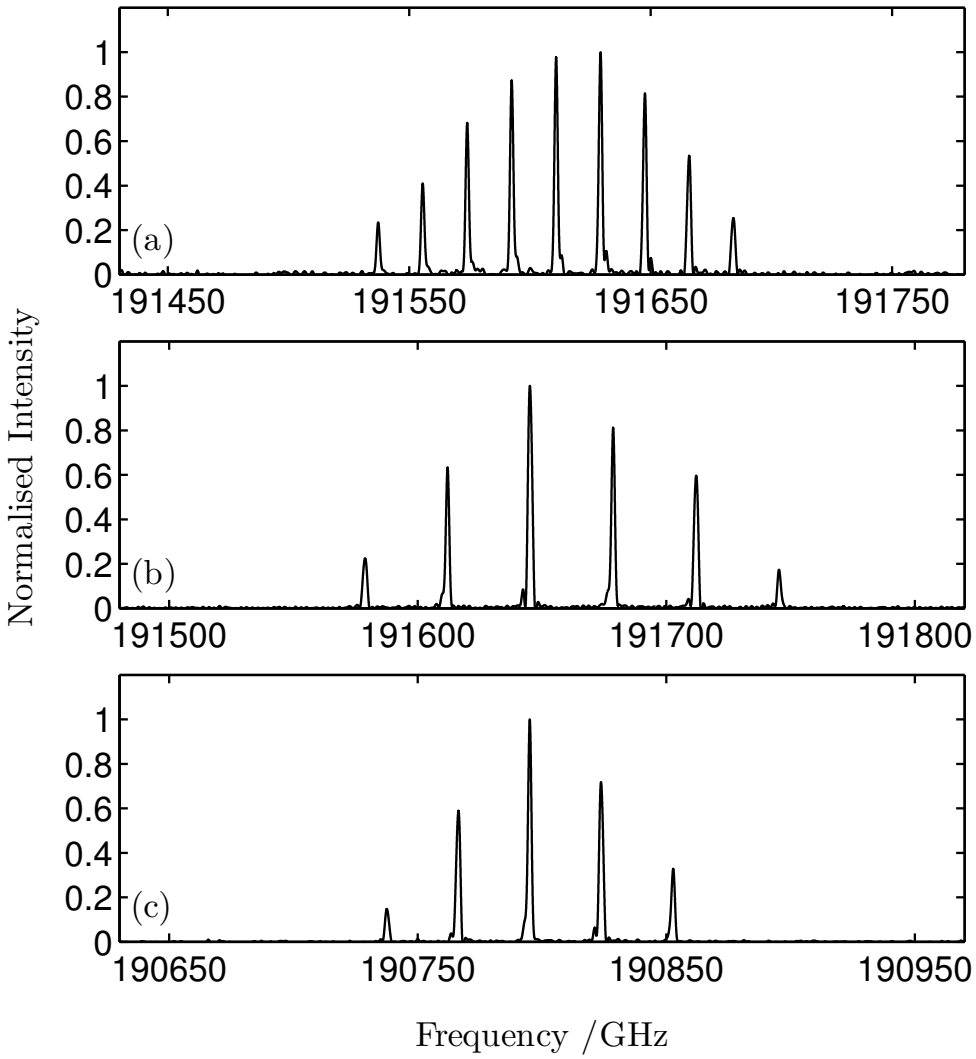


**Figure 4.12:** Spectra of three Er/Yb lasers illustrating the flexibility of this design. Data recorded with a 1 m spectrograph and a CCD array detector. **(a)** The laser described in this section. Mode spacing 18.39 GHz. **(b)** A laser design with a shortened cavity giving a mode spacing of 33.06 GHz. **(c)** A laser with intermediate cavity length and an input coupler with a reflectivity profile design to shift operation to longer wavelengths. Mode spacing 28.80 GHz and central comb frequency 190804 GHz ($\approx$ 1571 nm).

## 4.5 Conclusions

This chapter has reported on the development of a multi-mode laser intended to demonstrate multi-species detection with MUMAS. The near-IR spectral region was chosen for these experiments due to the maturity of laser technologies at these wavelengths and due to the number of overlapping vibrational bands found here.

A previous Er/Yb multi-mode laser design was used as the basis for the new laser, and its properties compared to the specifications required for the planned experiments. Improvements were needed to several properties of the laser design to produce a suitable multi-mode comb.

Development work was undertaken with the aim of making the required changes to the laser design; this work has been discussed in terms of the improvements required, the theoretical aspects of the laser design that had an influence on this property, and the changes that were made. The key properties needing improvement were reliability, temporal stability, and linewidth. The wavelength and bandwidth of the laser comb also needed to be changed.

Ultimately, these separate improvements were brought together into a new laser design. This system was tested and found to meet the required specifications.

# Chapter 5

# Multi-species MUMAS

## 5.1 Introduction

This chapter reports the first demonstration of multi-species detection using MUMAS [10]. An in-house constructed multi-mode Er/Yb:glass laser – the development of which was described in the previous chapter – has been used to detect three molecular species from within a mixture composed of these gases and additional non-absorbing components. MUMAS has previously measured multiple absorption features arising from transitions within a single molecule, in $O_2$ [6, 7], and $C_2H_2$ [8], but this extension of the technique comes closer to illustrating the full potential of MUMAS for gas sensing. This ability to perform multi-species detection with a single laser and a simple detection scheme compares favourably to other deployable multi-species detection schemes, such as those reviewed in Section 2.4.

As was described in Section 4.3.4 the custom multi-mode laser used in this work was designed with potential spectroscopic targets in mind. The precise output wavelength of the final laser allowed access to a region containing multiple transitions of three species: carbon monoxide (CO), nitrous oxide ($N_2O$), and acetylene ($C_2H_2$). Absorption

lines of all three molecules were present with similar maximum line strengths ($10^{-23}$ — $10^{-24}$ $cm^{-1}/(molecule \times cm^{-2})$), an ideal situation for laser absorption spectroscopy based multi-species detection.

The ability to detect these three species is of considerable interest for many applications. Carbon monoxide is a product of incomplete combustion, and thus exhaust gas CO monitoring can be used for closed-loop combustion control [33]. It is also used in concentration sensitive industrial processes such as the synthesis of acetic acid. Monitoring of carbon monoxide concentration in enclosed environments can be important due to its explosive (lower explosive limit 12.5 %) and toxic nature [96, 97]. Acetylene is a widely used but chemically unstable industrial gas; it is explosive over a very wide mixing ratio (2.5 — 100 %) and consequently rapid detection of leaks is important [96]. Finally, nitrous oxide is an atmospheric pollutant which is known to be a powerful greenhouse gas and damaging to the ozone layer [98–101].

The experiments discussed below were designed to demonstrate the ability of the MUMAS technique to simultaneously detect multiple gaseous species. As such it was important to first show that the signature arising from these species could be unambiguously identified both in a pure sample and in a gas mixture. Once this had been accomplished, the aim shifted to determining the ability of MUMAS to perform accurate, quantitative concentration measurements of individual components within a mixture. These experiments were not concerned, *per se*, with determining the lower detection limits of the technique; the transitions observed in the present work are not of sufficient line strength for achieving maximum sensitivity. Higher sensitivity multi-species detection is discussed in Chapters 6 and 7.

## 5.2 Experimental apparatus and procedure

### 5.2.1 Apparatus

A schematic diagram showing the layout of equipment used for these experiments is shown in Figure 5.1. It is a simple system, essentially very similar to direct absorption spectroscopy with a single mode laser. The output of the multi-mode laser is split (using a pellicle beam splitter, Thorlabs BP145B3, 45:55 split ratio) into probe and reference beams, with the probe directed through a multi-pass cell containing the absorbing gases. The radiation transmitted though the gas cell is measured by a photo-diode (Thorlabs DET-410), and recorded in the form of time varying intensity signals using a data acquisition system (Handyscope HS4). The reference beam is similarly detected and its intensity used to normalise the absorption signal for laser intensity variations. The multi-pass cell – a White cell (Specac, Tornado 20) – provided 16 m of absorber path length.

An additional beam splitter (Thorlabs BP108, 8:92) was inserted early in the beam path to extract a small fraction of the beam for on-line laser diagnostics. This enabled the use of several different instruments for determination of laser performance and properties: a Czerny-Turner grating spectrograph with a CCD camera (Andor model DU490A-1.7) was used to monitor the temporal properties of the mode structure, a Michelson interferometer-based spectrum analyser (Bristol Instruments 721-B IR) provided an absolute frequency scale for the laser spectrum, and a 1.5 GHz Fabry-Perot etalon (Thorlabs SA200-12B) was used to monitor the scanning of the laser modes. While these instruments provide useful information during development, they are not essential equipment for MUMAS – multi-species detection only requires a well characterised multi-mode laser and the ability to record time-varying intensity variations from the pump and probe channels.

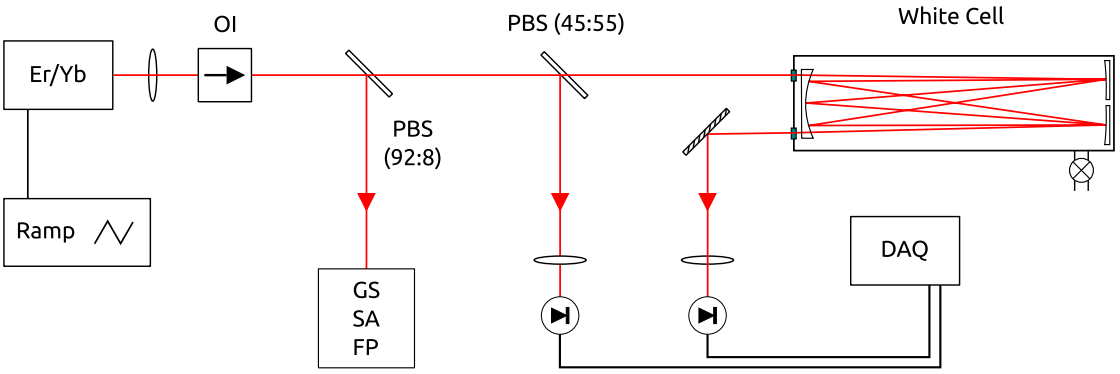


**Figure 5.1:** The experimental layout used for these measurements. Er/Yb represents the Er/Yb:glass multi-mode laser; GS, grating spectrometer; SA, spectrum analyser; FP, Fabry-Perot etalon; OI, optical isolator; PBS, pellicle beam splitter (marked with split ratio); DAQ, data acquisition system. Further details in the text.

Transmission spectra were recorded as the frequency of the laser modes was scanned repetitively at rates up to 10 Hz across the inter-mode spacing. This frequency sweep was effected through the use of a piezo-electric transducer stack to modulate the cavity length. A ramp signal was produced by a function generator (TTI TG315), amplified to high voltage by a commercial driver module (Noliac NDR6110) and applied to the piezo stack to sweep the cavity length.

Before carrying out measurements the gas cell was flushed with nitrogen and evacuated using a rotary vacuum pump (Edwards E2M5). To produce a sample for measurement different gases were then added to the cell with low partial pressures, as measured by a capacitance manometer (Setra 730, quoted accuracy 0.25% down to a pressure of 0.025 mbar).

### 5.2.2 Processing of data

For this work MUMAS spectra were recorded as the ratio between photodetector signals recorded from the signal and reference beams. A sequence of ∼20 such transmission measurements were averaged to reduce the impact of experimental fluctuations, and a

"frequency scanned" scale was applied to the spectrum using information provided by the Fabry-Perot spectrum analyser. A Fourier low-pass frequency filter was applied to the data to attenuate high frequency laser and detector noise. Stable baseline fluctuations, such as those caused by weak optical interference from stray beam path etalons, were removed by dividing the transmission signal by that of the empty gas cell.

To record a MUMAS spectrum it is only necessary to sweep the laser modes over a frequency corresponding to one mode spacing. If the frequency scanned exceeds the mode spacing, the pattern of absorption repeats as each absorption line is probed by the next mode in the comb, thus it is possible to easily confirm that a complete mode spacing has been covered. In practice, the scan is typically allowed to exceed $\Delta\nu_{space}$ by a factor of approximately 1.5 in order to ensure that all the spectral features within the overall bandwidth appear in the centre of the trace away from any inconsistencies that may be found at either end of the scan. The MUMAS fitting program requires that a single, complete scan is present and so a section corresponding to one mode spacing was selected by using knowledge of the mode spacing.

### 5.2.3 Correcting for non-linear frequency scan

The piezo stack was actuated with a linear, triangular ramp, however, the frequency scanned by the laser was observed to be non-linear. It was determined that the piezo transducer responded in a non-linear manner to applied voltage and further suffered from hysteresis in its movement. This affected the experimental data, causing spectral features in the recorded MUMAS traces to be distorted, with the first ∼20% of each scan being particularly badly stretched. This effect can be seen as curvature in the lines plotted in Figure 4.11.

This non-linear response can be corrected for in a similar manner as might be used in traditional, single-mode spectroscopy. A fraction of the beam is directed into the same

Fabry-Perot spectrum analyser used previously, and the pattern of fringes throughout the scan monitored. When using a single-mode laser a pattern of repeated fringes would be expected, each separated by the known free spectral range (FSR) of the etalon, however, in the case of a multi-mode laser the situation is more complex. The observed pattern is instead a complex interferogram, generated by individual modes each illuminating separate sets of transmission fringes of the etalon. When the etalon FSR is smaller than the laser mode spacing – the situation here – the pattern takes the form of multiple repeat-units of peaks, repeating every etalon FSR. For a laser comb of $n$ modes each unit is a pattern of $n$ peaks, with height corresponding to the mode intensity at that point in the scan and with a relative position linked to the order that each mode comes into resonance with an etalon fringe. A detailed explanation of the form of the repeat units can be found in Section 5.3.1.

However, the situation can be simplified by identifying the same feature in each of these units, which will occur every etalon FSR during the scan. This is illustrated in Figure 5.2, in which the lower panel shows the interferogram resulting from a single scan of the laser modes over a frequency slightly greater than one mode spacing. The location of the same fringe has been identified in each repeat-unit and all such instances are marked with a red star. The temporal positions of these marks are then transferred to the top panel of Figure 5.2, where they are plotted with their known frequency spacing. A time to frequency conversion function can then be computed by fitting a polynomial to this trend, allowing the experimental MUMAS spectra to be interpolated onto a linear frequency scale. The non-linearity of this conversion is illustrated with a straight line fitted through the latter portion of the trend.

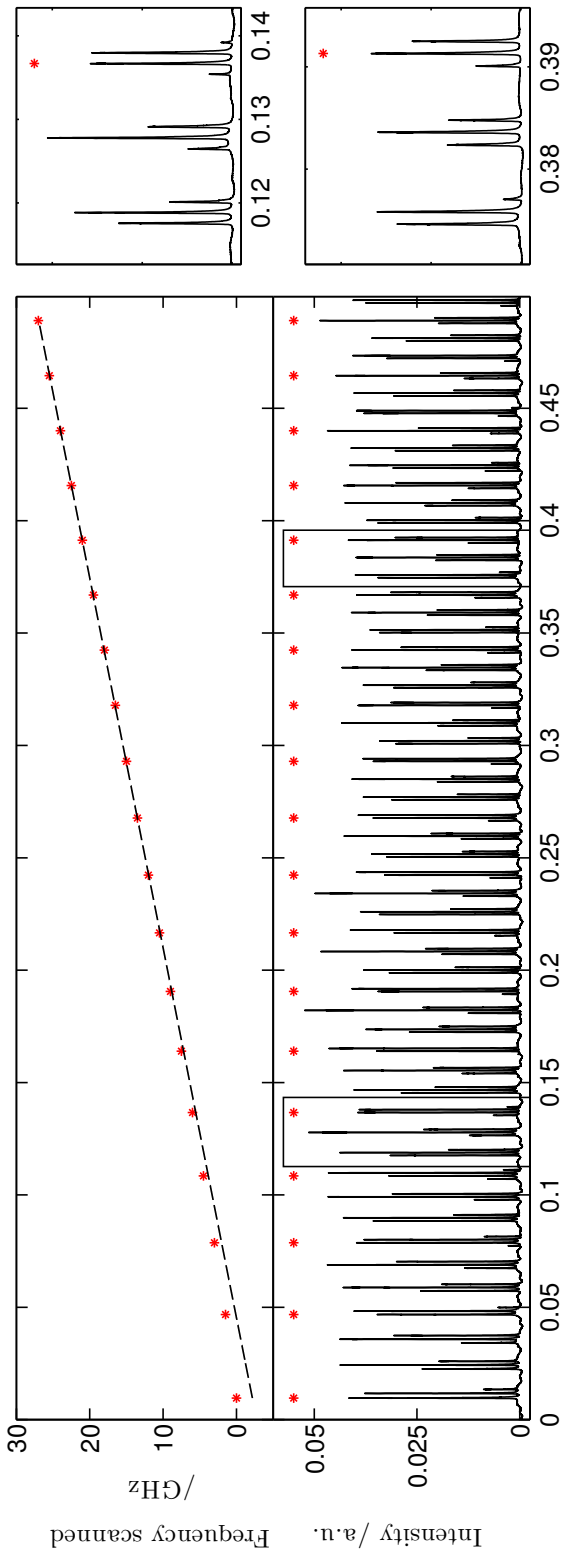


**Figure 5.2:** Calculating a time to frequency conversion for a MUMAS scan. **Main figure:** The lower panel shows the transmission signal recorded on passing the scanning multi-mode laser comb through a Fabry-Perot etalon: an interferogram containing a series of repeat-units occurring every etalon FSR. The temporal position of the same feature in each repeat-unit has been labelled with a red star. The known frequency spacing of these stars allows a time to frequency-scanned conversion to be computed (top panel). **Right:** Expansions of the marked regions of the etalon transmission signal, illustrating the repeating pattern.

## 5.3 Fitting of experimental data

An experimental MUMAS spectrum contains information both about the transmission spectrum of the gas sample that has been measured, and the properties of the multi-mode laser used to make the measurement, encoded together in a non-reversible manner. To extract either set of information, or parts thereof, it is necessary to forward-model the experimental process and then fit this model to the experimental data in an iterative manner. The parameters of the model that produced the best fit to the data are then taken as the experimental measurement.

To carry out this process with the aim of detecting or measuring the concentration of a species within a gas sample requires an accurate model of the MUMAS process, a complete spectral database, a robust fitting algorithm, and good knowledge of the properties of the laser comb. The MUMAS model, and the improvements made to it during the course of this work are described in Chapter 3; the method used to determine laser properties, and the fitting of experimental spectra is described below.

### 5.3.1 Accurate determination of laser parameters

The fitting of experimental MUMAS spectra requires a good knowledge of parameters describing the laser, namely the frequency separation of the laser modes ($\Delta\nu_{space}$), the linewidth of these modes ($\Delta\nu_{width}$), and the envelope function describing the laser comb ($E(\nu)$), which in turn defines the central frequency and the relative mode intensities. Measurement of these parameters can be performed with commercially available spectrum analysers, however, in most cases the precision of such measurements is insufficient for the modelling process. In practice, the best method is to take such a coarse measurement and optimise it, by fitting a modelled MUMAS spectrum to experimental MUMAS data taken under controlled conditions.

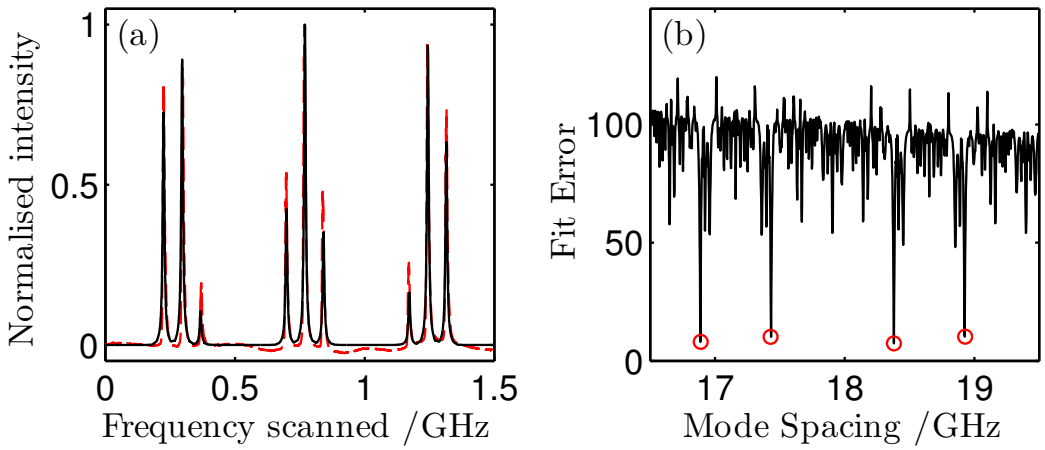


**Figure 5.3:** An analysis of the interferogram resulting from the interaction of the multi-mode laser with a Fabry-Perot etalon. **(a)** A single repeat-unit from the interferogram (red, dashed line), fitted by a model (black, solid line). **(b)** The fit error plotted against laser mode spacing showing repeated minima (marked with red circles) corresponding to equally-likely solutions. This ambiguity in the measured value of the mode spacing can be resolved only by additional information.

The most critical parameter in modelling the MUMAS signature is the mode spacing, due to the sensitive and non-linear dependence that the MUMAS spectrum has on this variable [45]. An estimate of this may be made with a spectrometer or spectrum analyser such as the Bristol Instruments 721-B IR used in this work. This estimate can then be improved through the consideration of the same interferogram between the multi-mode laser and a Fabry-Perot etalon as was used for frequency linearisation. Analysis of the pattern of peaks within a single repeat-unit allows determination of the mode spacing to be made with good precision.

This analysis was carried out through a modelling process. An adapted version of the MUMAS model was produced to simulate the interferogram, and this fitted to the experimental data in an exhaustive manner by varying the mode spacing. The outcome of this process is shown in Figure 5.3(a), which shows a single repeat-unit fitted with the model. The fit error for different values of laser mode spacing is shown in Figure 5.3(b)

from which it can be seen that due to the periodic nature of the etalon fringes, this analysis provides a series of similarly-likely repeat solutions, seen to occur approximately twice per etalon FSR. This ambiguity can be resolved only with additional information, for example that provided by an interferogram of the same light obtained with an etalon of different FSR. In practice it is possible to exclude all but 2 — 3 of these possible values using the spectrum analyser estimate, ultimately providing a small number of precisely known possible values for the mode spacing. Each of these can then be quickly tested to find the correct solution by fitting data taken under known conditions.

The form taken by the interferogram repeat-unit is dependent on the ratio of $\Delta\nu_{space}$ to the etalon FSR, and can look quite different for different values of these parameters. The triplet pattern observed in Figure 5.3(a) implies that the etalon FSR is close to being a multiple of three times the laser mode spacing (i.e. $3\Delta\nu_{space}/FSR \approx n$). Thus, every third laser mode (almost) simultaneously comes into resonance with its respective etalon fringe.

The value of the mode linewidth, $\Delta\nu_{mode}$, may also be estimated with the same modelled fit to the interferogram data. The observed fringes had a FWHM of approximately 11 MHz and this was best reproduced by using a laser mode linewidth of 8 MHz (the finesse of this etalon was specified to be 494 giving an instrumental linewidth of 3.0 MHz). This value is much narrower than the absorption features being probed, and as such the actual value of this parameter is not critical, since it does not contribute significantly to the observed width of the feature in the MUMAS signature. Therefore this parameter was not optimised further and a value of 8 MHz was used in all subsequent fitting.

The intensity envelope of the laser is parametrised in the MUMAS model as an analytical function representing the shape of the comb and its central frequency ($\nu_{centre}$). For the Er/Yb laser used in this work a good representation of the laser comb was produced by subtracting a constant from a Gaussian profile and then renormalising the

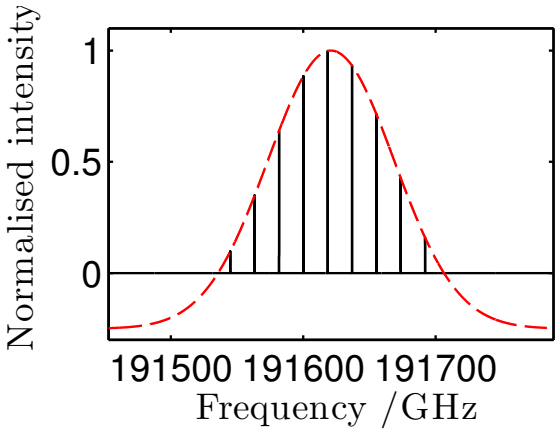


**Figure 5.4:** A modelled spectrum of the laser comb overlaid with the mode envelope determined from the fit to the acetylene spectrum.

resultant profile to a peak intensity of unity (this is illustrated in Figure 5.4). This necessitated two parameters, the FWHM of the Gaussian ($\Delta\nu_{env}$), and the constant to subtract ($c$). Estimates of $\nu_{centre}$, $\Delta\nu_{env}$ and $c$ were obtained with the Bristol Instruments spectrum analyser.

These estimated values of the laser parameters were then further refined by fitting a MUMAS spectrum taken under known conditions. A sample of $C_2H_2$ was measured at room temperature and a pressure of 6.66 mbar. The recorded MUMAS trace was then fitted by holding constant the parameters describing the properties of the gas at known values, and allowing the laser parameters to vary from their starting values within tight limits. The method by which this fit is carried out is described in the next section. Acetylene was chosen for this calibration procedure as in this region the transitions are the result of several overlapping vibrational bands. This produces a complex, non-repeating pattern of absorption features, reducing ambiguity when looking for a global minimum. The estimates of the parameters used as starting conditions for this fitting process are listed in Table 5.1 alongside the final, optimised values.

| Parameter | Estimate | Final value |
|---|---|---|
| $\Delta\nu_{space}$ | 17.43, 18.38, 18.93 GHz | 18.39 GHz |
| $\Delta\nu_{width}$ | 8 MHz | *not optimised further* |
| $\nu_{centre}$ | 191600 GHz | 191621 GHz |
| $\Delta\nu_{env}$ | 100 GHz | 112 GHz |
| $c$ | 0.03 | 0.20 |

**Table 5.1:** Values of the parameters describing the multi-mode laser used in this work. Estimates were first generated though a combination of direct measurement techniques and then these refined through the fitting of experimental data taken under known conditions. The details of this process are described in the text.

### 5.3.2 The fitting process

To achieve a good fit between modelled and experimental spectra is is necessary to generate an error signal, which provides a method to quantify the discrepancy between the two spectra. This can then be minimised by a suitable algorithm through the process of varying model input parameters. The stages required to achieve this are described here.

#### Comparing model to experimental data

Before a direct comparison can be made between the model and the data two additional steps must be taken. After processing, experimental MUMAS spectra consist of a transmission signal varying over a frequency window, which corresponds to the mode spacing of the laser modes ($\Delta\nu_{space}$). As was described in Chapter 3, the frequency of each laser mode at the start of the scan is sensitively dependent on the cavity length (and hence the cavity FSR). It is impractical to make a direct, sufficiently precise measurement of this property, so no attempt is made to predict this parameter in the MUMAS model. Instead, the fact that the modes scan under a frequency-fixed envelope is used – this means that when any mode passes through a particular *absolute* frequency its intensity

will be of the same value, and so it does not affect the spectrum if a particular absorption feature is probed by a particular mode at the end of its scan, or the next mode as it starts to scan.

To account for the cyclic shift that may therefore be present between the model and the data the modelling code is instructed to produce an output corresponding to a scan over twice the mode spacing. This simulated spectrum will contain two identical sets of absorption features. The experimental spectrum contains only one set of features but probably starts in a different place. A cross-correlation between experiment and simulation is used to determine this frequency offset. In practice, MUMAS spectra are recorded by sweeping the laser modes up and down in frequency, which may cause features to appear in the opposite sequence. Therefore this process is also carried out with the experimental data reversed on its frequency axis to determine the direction of frequency scan in the experiment.

As is often the case in absorption spectroscopy, determining the zero-absorption level in a recorded MUMAS spectrum can be difficult. Experimental drifts occurring in the time between measuring the background transmission of the gas cell and measuring the transmission of a sample can result in small offsets in the transmission of the recorded spectra. Similar results can result from frequency-independent losses, such as scattering. To allow for these small discrepancies a small offset value (typically within the range $\pm 10^{-3}$) is added to the experimental transmission signal and allowed to vary in the fitting process.

#### The minimisation problem

An experimental MUMAS spectrum, $M'$, can be compared to a modelled MUMAS spectrum generated for the same frequency scan, $M$, by means of the residual vector,

calculated:

$$r_j(\mathbf{x}) = M_j(\mathbf{x}) - M'_j \tag{5.1}$$

where $\mathbf{x} = [x_1, x_2, \ldots x_n]$ is the set of parameters on which the modelled spectrum, and hence the residuals, depends [45]. The index, $j = 1, 2, \ldots m$, runs over the elements at which the MUMAS spectra (both measured and simulated) are sampled, and represents, in essence, discrete steps in frequency space.

It is the aim of the fitting routine to minimise the error function, defined

$$\mathcal{E}(\mathbf{x}) = \sum_{j=1}^{m} w_j r_j^2(\mathbf{x}) \ , \tag{5.2}$$

where the vector $w_j$ is a weighting vector, allowing the importance of different regions of the spectrum to be varied. The usual case is an un-weighted fit, where the elements of $w_j$ are set at unity.

Therefore $r_j(\mathbf{x})$ is a set of $m$ non-linear equations in $n$ variables (these are the input parameters of the MUMAS model), and the minimisation of the error function, $\mathcal{E}(\mathbf{x})$, is a non-linear least squares problem. In general, non-linear least squares problems may feature multiple local minima and maxima, and are consequently difficult to minimise.

**The model parameters**

Two properties of the parameters for a non-linear least squares fitting problem are particularly important to allow a solution to be computed in an efficient and accurate manner: their orthogonality and relative sensitivity. A good degree of orthogonality of each member of the set of parameters ($\mathbf{x} = [x_1, x_2, \ldots x_n]$) is desirable as this allows simpler methods to be utilised in the solving of the problem. In the case of fitting algorithms based on Newton's method it allows use of just the Jacobian matrix, and does not require an additional set of Hessian matrices that would be required to allow

for covariance; a considerable computational advantage [102].

The MUMAS model has five laser parameters and other parameters describing the sample, which include the total pressure, optical pathlength, temperature and the partial pressures of any absorbers (see Table 5.2). It is clear that these inputs are not all completely orthogonal, for example, the combination of pressure and temperature broadens features through pressure broadening in a manner that is very similar to the result of an increase in laser linewidth. Fortunately, fitting only occurs over a subset of parameters, and for the subsets most commonly chosen the parameters are found to be nearly orthogonal.

The first stage of analysing a dataset involves accurately determining the laser parameters by fitting a spectrum taken under known conditions. The orthogonality of these parameters was investigated in the course of previous work on MUMAS [45]. It was found that the four laser parameters used in that work ($\Delta\nu_{space}$, $\Delta\nu_{width}$, $\Delta\nu_{bandwidth}$, $\nu_{centre}$) were independent to a good degree. The laser used in the current work requires an additional parameter, $c$, to describe the cut-off on the envelope function, and this has been found to be not entirely orthogonal to other laser parameters. Thus, care is required in the optimisation of its value.

The most common case in which MUMAS spectra are fitted is when analysing a dataset to determine partial pressure of absorbing species, or sample temperature. Individual absorbing species each contribute a unique set of transitions to the MUMAS fingerprint, and so it can be seen that the partial pressures of these components – determining the measured absorption of these sets – will be orthogonal, provided that the transitions can be individually resolved. The sample temperature is determined from the observed strengths of transitions arising from one species. This measurement will be independent of partial pressure provided that multiple transitions fall within the measurement window, and that these transitions have been chosen such that they experience an appreciable

| Laser parameters | | Additional variables | |
|---|---|---|---|
| Mode spacing | $\Delta\nu_{space}$ | Temperature | $T$ |
| Mode linewidth | $\Delta\nu_{width}$ | Pressure | $P$ |
| Envelope width | $\Delta\nu_{band}$ | Absorption pathlength | $L$ |
| Envelope centre | $\nu_{centre}$ | Partial pressure of absorber $i$ | $p_i$ |
| Envelope offset | $c$ | Data offset | $\delta$ |

**Table 5.2:** Parameters used in the fitting of MUMAS data.

change in their *relative* strength over the temperature range of interest.

It is also important to consider the relative sensitivity of the model parameters. Optimisation algorithms generally make perturbations of the same magnitude to each of the variables, when determining the local gradient of the fitting surface. This can lead to certain variables being neglected if their effect on the model is small when compared to others, in turn producing slow convergence and poorly optimised solutions. The absolute values of the MUMAS model parameters vary over many orders of magnitude, and the sensitivity of these parameters to relative changes also varies greatly; for example $\Delta\nu_{space}$ is more that 100 times more sensitive that $\nu_{centre}$. These sensitivity differences are compensated for by centering and rescaling all parameters such that a user-chosen confidence range is linearly mapped onto the same fitting range.

### The fitting strategy

The fitting of a model to experimental MUMAS spectra has previously been investigated in detail, and a working method developed. The approach detailed in Arita [45, Chapter 5] utilised a nonlinear least-squares fitting algorithm to efficiently find a solution to the problem, and is summarised below. However, in some circumstances this method has been found unreliable (both in previous work and in the current work). Therefore, an alternative method has been developed for use in such cases. Both of the methods, and

the situations in which they are used, are described below.

A fitting function was written in the course of previous work to fit the MUMAS model to experimental spectra. This program used a non-linear least squares fitting algorithm, *lsqnonlin*, provided in the MATLAB computing environment. In operation, the fitting program called the MUMAS model, calculated the error function, $\mathcal{E}(\mathbf{x})$, and then attempted to minimise this by varying input parameters. Starting values and upper and lower bounds of the fitting parameters were chosen by the user.

This approach provides an efficient method to optimise problems that possess a simple error surface, where the parameter space investigated produces a single, global minimum. However, this is not necessarily the case for the optimisation of all parameters in the fitting of MUMAS. Some fitting problems result in a complex error surface characterised by multiple local minima from which the optimum solution corresponds to the lowest. In this scenario a nonlinear fitting process can become "trapped" in a local minimum, leading to a result that is not the global minimum and that is sensitively dependent on the starting values of the input parameters.

To give an example, the initial fitting of laser parameters as described in Section 5.3.1 shows such behaviour. An alternative method to determine a best fit in such a situation is by an exhaustive search of the parameter space, trying each combination of parameters over a pre-defined range to find the global minimum. The drawback of this approach is that the time required to complete a fit can be very large, particularly when solving for multiple parameters.

Therefore a hybrid fitting strategy has been developed. In cases where the error surface is expected to be simple, such as the fitting of absorber concentration for a well characterised laser, the experimental spectra are fitted by the non-linear least squares method. This provides a quick, reliable result, making it suitable for processing many spectra, and allows the fit to be simultaneously optimised for multiple parameters, such

as the concentrations of multiple absorbing species.

In cases that are expected to yield more complex error surfaces, such as the determination of laser parameters, an exhaustive search is used. To make this more efficient, parameters are optimised independently where possible, relying on their near-orthogonality. A final multi-parameters search can then be carried out over a very small range to allow for any deviations from this ideal. To further increase the efficiency of the exhaustive search, parameters are initially investigated on coarse grids before then "homing in" to investigate promising areas in more detail. Overall, this process has been found to reliably fit the laser parameters, and while it takes more time and is less automated than the non-linear least squares fit it only needs to be performed at most once per dataset.

## 5.4 Results and discussion

### 5.4.1 Single-species MUMAS

The MUMAS spectra of the three chosen molecular species, $N_2O$, CO and $C_2H_2$, were first recorded individually to verify the operation of the equipment and the fitting process. Averaged MUMAS spectra were obtained from typically 20 scans at a repetition rate of around 3 Hz and processed as described in Section 5.2.

The experimental spectra were then fitted to determine the partial pressure of absorbing species. This was performed by setting the laser properties to those previously determined (Section 5.3.1) and allowing the non-linear least squares fitting algorithm (Section 5.3.2) to vary the partial pressure of absorber to produce the best fit between measurement and model. This process is illustrated for the case of $N_2O$ in Figure 5.5, in which the lower panel shows a recorded MUMAS spectrum for 1.80 mbar of $N_2O$ as a dashed red line, and the best-fit, modelled MUMAS spectrum as a solid black line. The

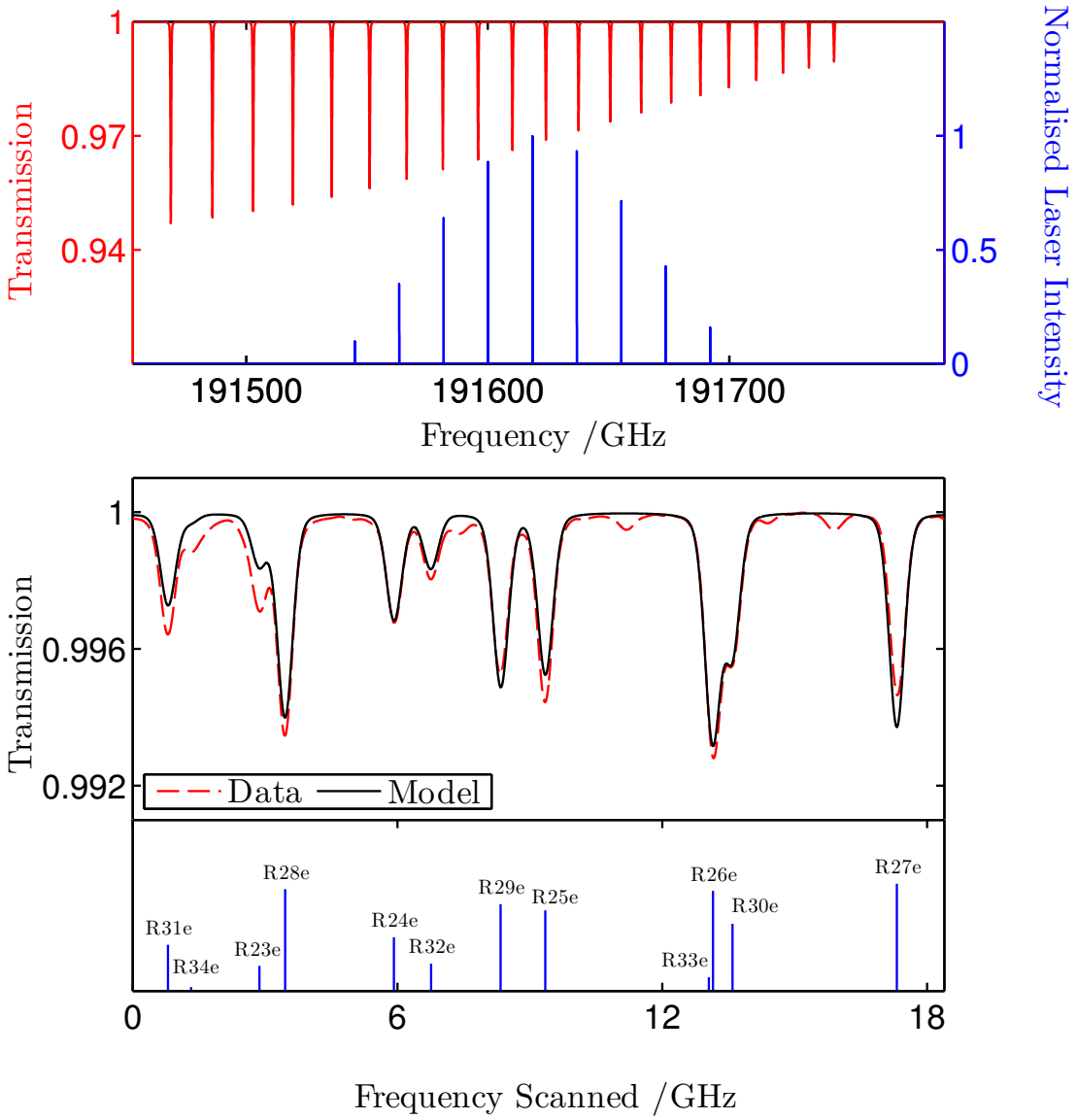


**Figure 5.5:** Modelling and fitting of MUMAS data is illustrated for the case of $N_2O$. The upper panel shows the simulated $N_2O$ absorption spectrum around 1565 nm (in red) and the simulated mode spectrum of the Er/Yb laser (blue). In the lower panel the simulated MUMAS spectrum resulting from using this mode spectrum is shown as a solid black line. The dashed red line is the experimental data to which the modelled $N_2O$ MUMAS spectrum is fitted. The stick spectrum in the lower panel indicates the spectral assignments of the observed transitions which lie in the $5^{th}$ harmonic of the $\nu_1$ band of $N_2O$.

simulated experimental conditions used to generate this modelled spectrum are shown in the upper panel. The absorption spectrum of $N_2O$ in this spectral region is plotted in red, calculated using the values of line positions and strengths of the $5^{th}$ harmonic of the $\nu_1$ band from the HITRAN database [76]. The modelled laser mode spectrum, generated using parameters listed in Table 5.1 is shown in blue.

Figure 5.5 shows that there are slight discrepancies between the modelled and measured spectra. These take the form of differences in the peak absorption values of several lines, and the presence of additional absorption features in the data that do not appear in the simulation. The additional features may arise from impurity species that have not been identified or weaker transitions in $N_2O$ not tabulated in the literature (in this region the spectral database only includes transitions to a minimum line strength of 5 times weaker than the strongest probed here). The spectroscopic assignment of each absorption feature is given in the stick spectrum in the lower part of the panel. From this it can be seen that the MUMAS spectrum is the result of the interaction of the laser comb with 12 transitions spread over ∼150 GHz (∼1.2 nm).

Similar spectra were recorded for the other two gas species, CO and $C_2H_2$. Figure 5.6 shows the same $N_2O$ spectrum alongside spectra of samples of CO at 1.41 mbar and $C_2H_2$ at 8.76 mbar, all fitted with modelled spectra. It can be seen that the CO spectrum only consists of two features, a result of the widely spaced transitions found in the $3^{rd}$ harmonic of the $\nu_1$ band measured here. In this simple case the MUMAS model provides a very good ft to the experimental data.

The $C_2H_2$ transitions probed here arise from several overtone and combination bands, and as a result this spectral region contains many transitions, leading to a more congested MUMAS spectrum. First attempts to fit this spectrum with transition data from the HITRAN database proved unsuccessful and upon further investigation it was determined that the database was incomplete in this region. To obtain reliable spectral information

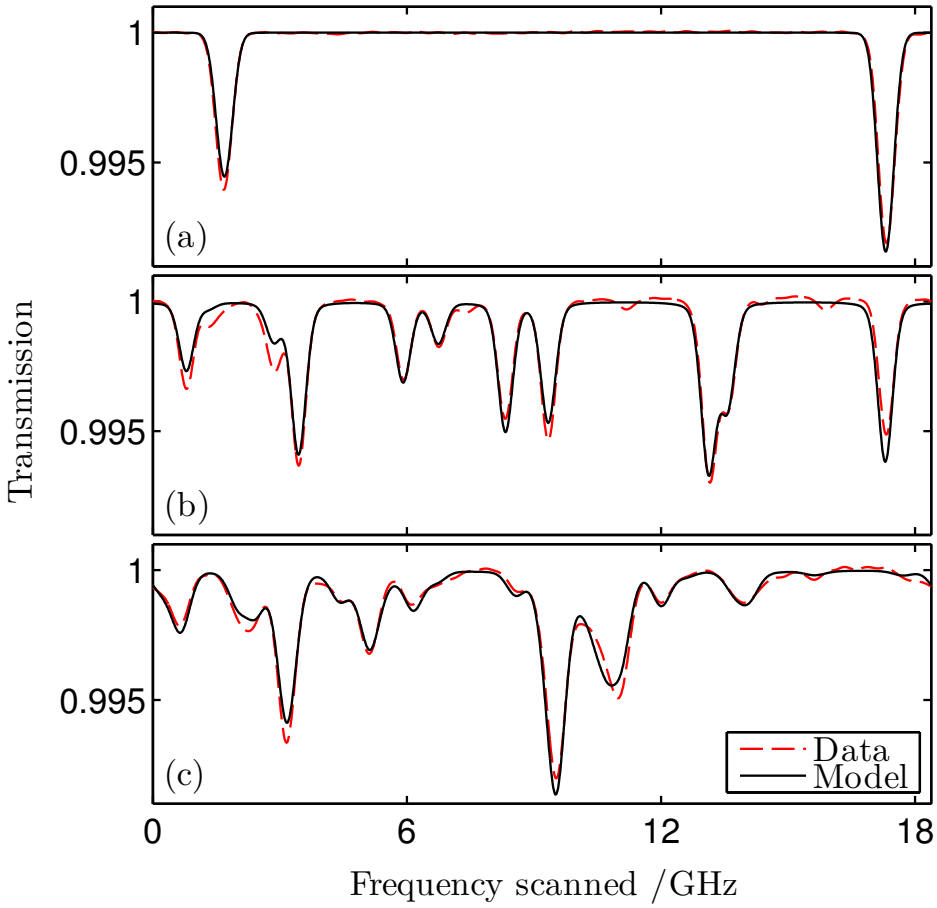


**Figure 5.6:** Experimental MUMAS spectra of **(a)** 1.41 mbar CO, **(b)** 1.80 mbar $N_2O$, and **(c)** 8.76 mbar $C_2H_2$. The dotted red lines indicate experimental data and the solid black lines the temperature- and pressure-dependent modelled fit to the data, from which concentrations of the species may be derived.

a survey of the line positions and strengths of $C_2H_2$ absorption transitions was carried out over a wide region spanning the area probed here. An external cavity diode laser was used to record ∼30 overlapping TDLAS spectra of a low-pressure sample of $C_2H_2$ in a White cell. The strongest absorption features were fitted with a Voigt profile to obtain an estimate of their position and strength using a sample of CO in a different, single-pass cell as a wavelength reference. This work is reported in Appendix A. With the resultant, more complete, spectral database it was possible to successfully fit the

measured spectrum with only small differences between the model and data. In the case of all three species examined here the fits to the multiple transitions present in the MUMAS spectra provide a method to unambiguously identify the presence of each species.

**Spectral coverage**

The wide spectral coverage achieved and large number of transitions probed by the MUMAS technique can be illustrated in a more familiar fashion by plotting the molecular absorptions that contribute to the MUMAS spectra in Figure 5.6 in their true spectral positions, as tabulated in the HITRAN database or, for the case of $C_2H_2$, from TDLAS measurements. The MUMAS signature essentially consists of a superposition of a family of individual single-mode scans, each taken across a frequency range corresponding to the interval between adjacent laser modes. Figure 5.7 shows the transitions detected in the three MUMAS spectra in Figure 5.6 plotted on a wavelength scale and broadened to account for their temperature- and pressure-dependent linewidths using partial pressures derived from the fits to the data in Figure 5.6. In effect Figure 5.7(a), (b) and (c) show the modelled single-mode laser spectra equivalent to the MUMAS spectra in Figure 5.6(a), (b) and (c). The density of spectral lines leads to frequent overlap and thus not every transition is individually resolved in the MUMAS signature but their presence is inferred from the best fit to the data. The large number of lines recorded in this spectral range for $C_2H_2$ is largely responsible for the apparent background absorption in Figure 5.6(c).

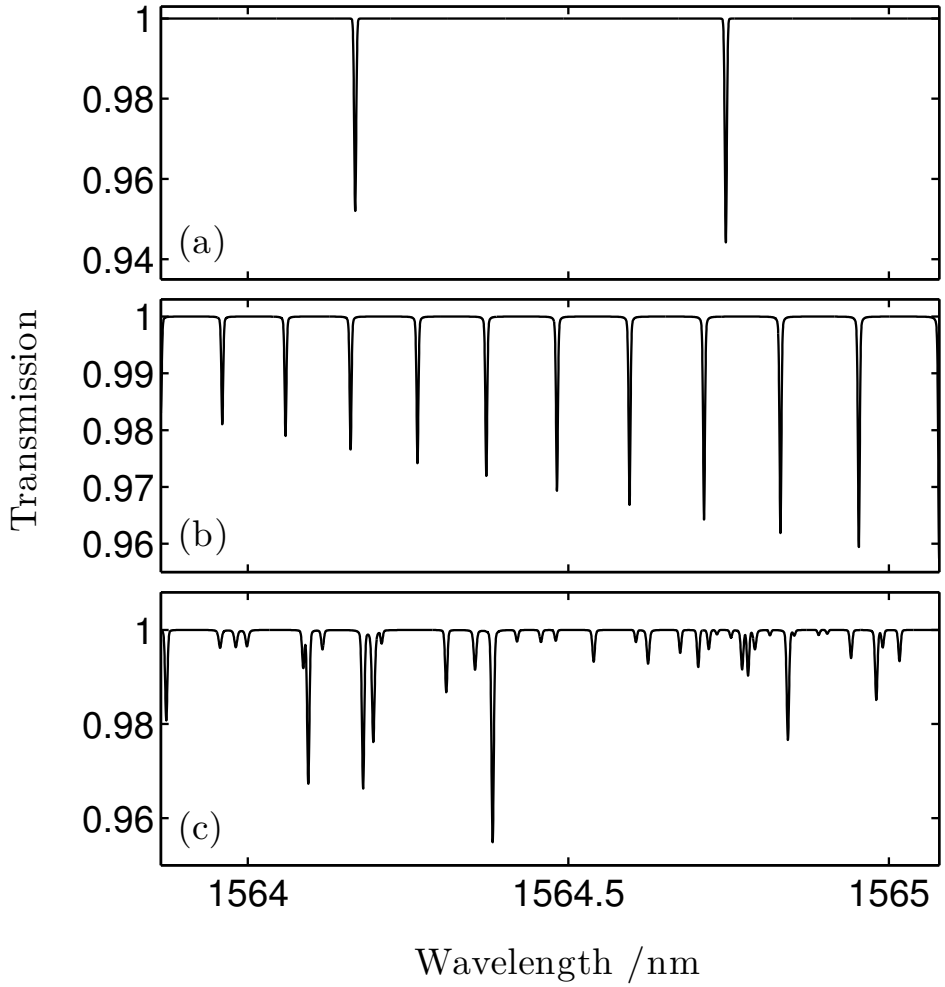


**Figure 5.7:** Modelled spectra of the transitions that comprise the MUMAS spectrum in Figure 5.6, illustrating the broad spectral coverage of the MUMAS technique and the large number of transitions probed. The transitions detected in the MUMAS spectra of CO, $N_2O$ and $C_2H_2$ are shown in **(a)**, **(b)** and **(c)**, respectively. Each spectral feature is modelled using line strengths, spectral positions, and broadening coefficients obtained from the HITRAN database, or from TDLAS measurements, and partial pressures from the fitted MUMAS spectrum in Figure 5.6. The density of lines in the spectrum of $C_2H_2$ in **(c)** is largely responsible for the apparently non-zero background to the MUMAS spectra in Figure 5.6(c).

### 5.4.2 Multi-species MUMAS

#### Multi-species detection

Once the operation of the experimental apparatus had been verified by successful single-species detection, focus moved to the detection of multiple species from within a gas mixture. Mixtures containing CO, $N_2$ and $C_2H_2$ were created in the gas cell with differing component ratios and total pressures. These samples were interrogated with the multi-mode laser and the resultant spectra processed and fitted by allowing the partial pressure of each component to vary. Again, this data was recorded by averaging 20 scans at 3 Hz repetition rate and narrow features were assured by operating at a sufficiently low pressure to minimise collisional broadening. Figure 5.8 shows the MUMAS spectrum of such a gas mixture; in this sample the partial pressures as measured by the capacitance manometer were: 0.64 mbar of CO, 4.47 mbar of $N_2O$ and 6.86 mbar of $C_2H_2$.

It can be seen that the fitted MUMAS model reproduces the measured spectrum well with only small discrepancies evident. All the features in this modelled MUMAS signature are identifiable as arising from one of the three species present, thus this technique provides a method to selectively detect the presence of multiple species in a gas sample using a single measurement. This is illustrated in the lower panels of Figure 5.8 which indicate the assignment of absorption features to individual transitions arising from one of the three species present; each molecular transition that has been used to produce the modelled fit is plotted as a line with height given by the reduction in transmission it contributes to the overall modelled spectrum. MUMAS achieves this selective detection ability due to the unique and characteristic absorption pattern produced by the interaction of a multi-mode laser with multiple transitions occurring at precisely known frequencies.

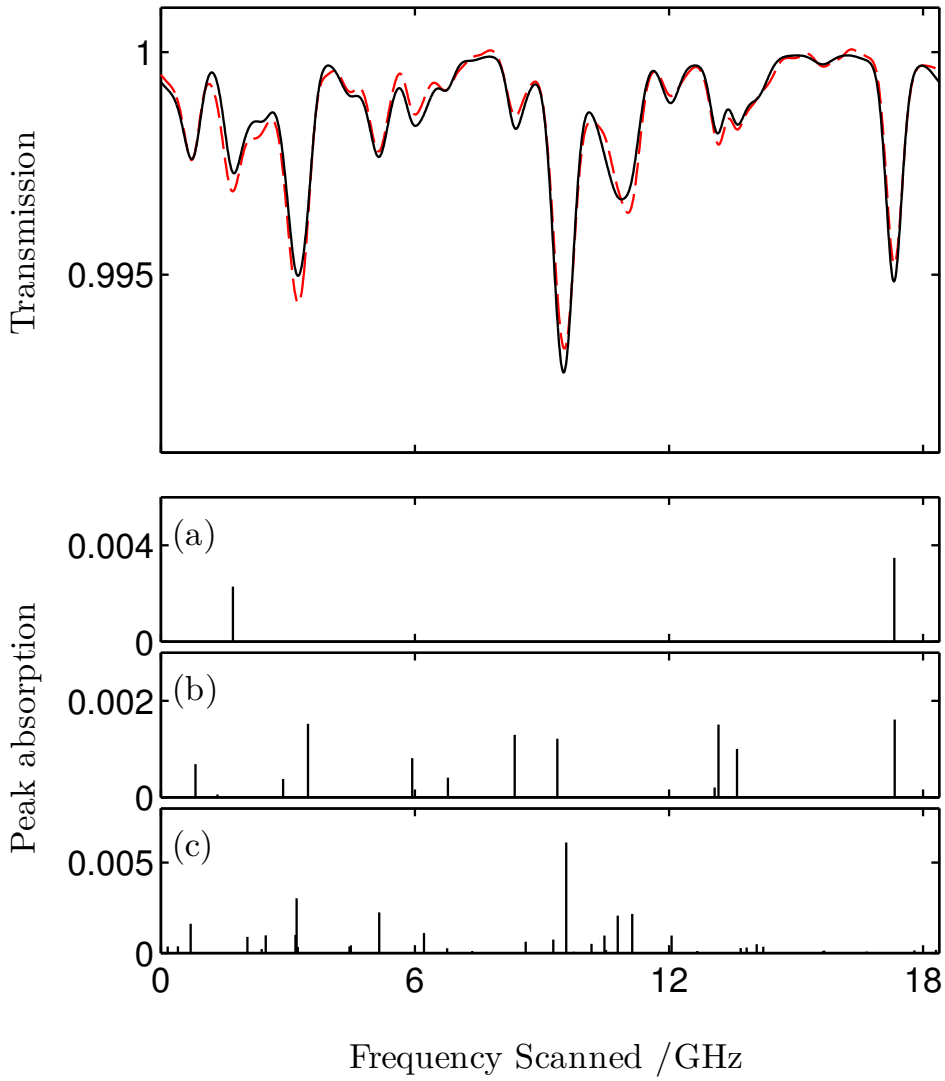


**Figure 5.8:** Experimental MUMAS spectra of a mixture of three species – 0.64 mbar of CO, 4.47 mbar of $N_2O$ and 6.86 mbar of $C_2H_2$. In the top panel the experimental data (dashed red line) is plotted with the best fit of the model (solid black line). This single measurement allows identification of the three component species from the pattern of their transitions. This is illustrated in the lower 3 panels where the contribution of **(a)** CO, **(b)** $N_2O$, and **(c)** $C_2H_2$ to the total MUMAS spectrum are identified.

**Composition measurements**

The best-fit of the modelled spectrum to the data is produced by allowing the partial pressure of each gas to vary independently, providing a method to determine the absolute number density or partial pressure of the species directly from a recorded MUMAS spectrum. The MUMAS model produces an expected absolute transmission profile of a sample and so it was originally hoped that an absolute composition measurement could be performed. In practice, however, this has not been the case, suggesting that a calibration procedure may be necessary. An attempt at such a calibration for all three species measured here is shown in Figure 5.9. For each mixture the fitted pressure of each component is plotted against the partial pressure of that component as measured by a capacitance manometer. From this it is observed that for all three components the fitted pressure varied as a linear function of the measured pressure. Therefore a best fit straight line is calculated for each species to give the absolute calibration.

The gradient of these best fit lines is seen to deviate from unity, however, suggesting that the discrepancy arises from uncertainty in a pressure dependent factor in the modelling of the MUMAS spectrum. In the modelling of the multi-species spectra described here the foreign gas broadening parameter for each transition has been assumed to be that for air due to the lack of available information for interactions between the molecules present, however, in practice the true value may be different. As a result the slopes of the best fit lines are either greater or less than 1.0 depending on whether the dominant broadening is more or less effective than air. In general this will be a problem for any arbitrary mix of different gases since the relevant line broadening data will not always be available in the literature, making such calibration procedures a matter of course for absolute composition measurements of low pressure samples with MUMAS. However, in situations where the dominant broadening is by gases such as nitrogen or

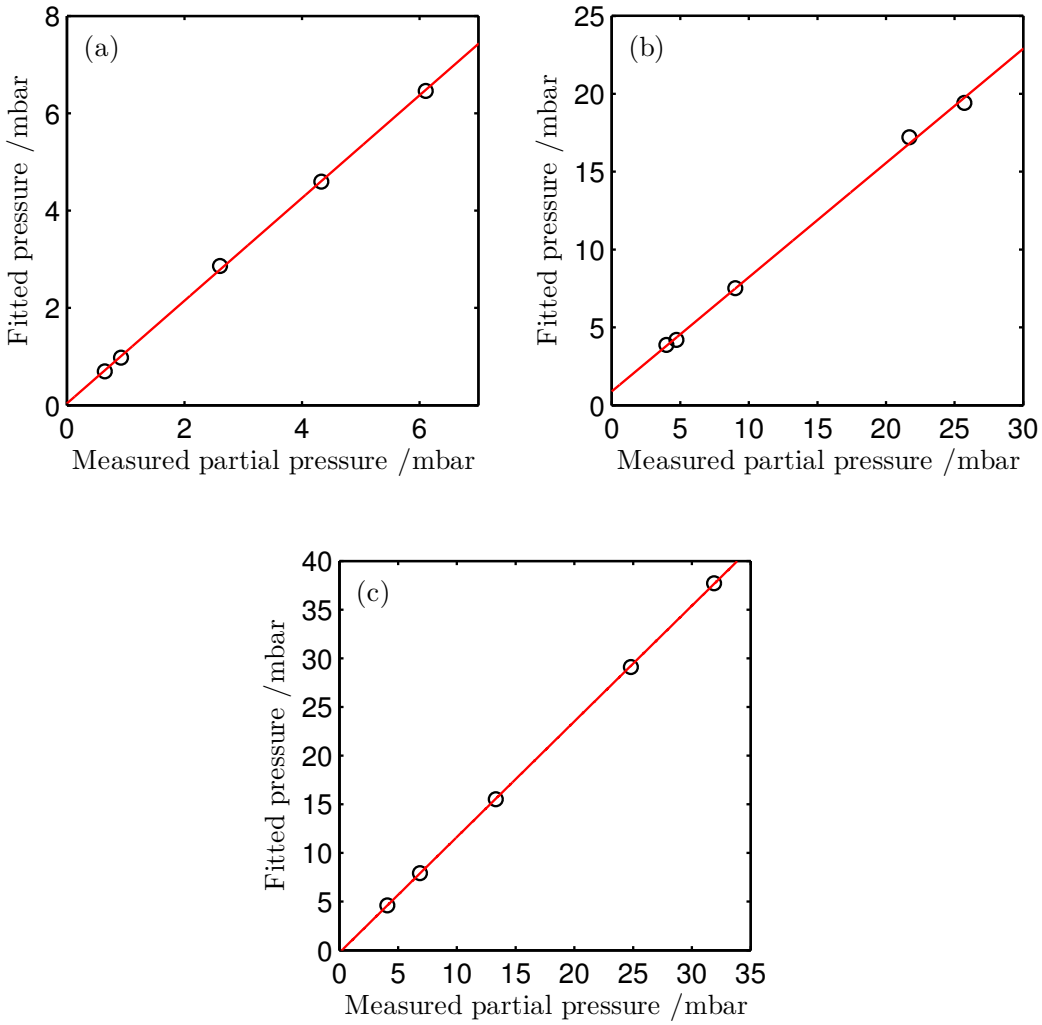


**Figure 5.9:** Quantitative multi-species detection with MUMAS. A comparison between the partial pressure of a mixture component as determined by MUMAS to that measured by a capacitance manometer. Plots are shown for each of the three components – **(a)** CO **(b)** $N_2O$ **(c)** $C_2H_2$ – of 5 different gas samples. The straight lines indicate the linear best-fit to the points for each case and provide a calibration for this MUMAS system.

oxygen, which have known broadening constants and are commonly encountered, this source of uncertainty may not be a major problem. Nonetheless the present data clearly shows the possibility of using MUMAS to perform such measurements, identifying species and measuring their concentrations, using calibration procedures when necessary.

The error that a measurement using this calibration will incur can be estimated by examining the deviation of each data point from the straight line. Any discrepancy may be due to uncertainties in measuring the absolute values of the small absorptions recorded at these low pressures. For the measurements shown here, the mean deviation for each fitted partial pressure from the calibration line has been determined to be 1.7%, 1.9% and 0.2% for CO, $N_2O$ and $C_2H_2$, respectively. Thus partial pressures of each gas in the mixture could be inferred from MUMAS data with an experimental uncertainty of better than 2%.

**Selectivity of detection**

The ability to distinguish differing partial pressures of a specific component in a mixture was further investigated by recording MUMAS data in a mixture containing variable amounts of CO. In order to achieve a low but accurately known initial partial pressure of CO, an accurately measured quantity, of the order of 1.0 mbar, was introduced to an evacuated cell and diluted with $N_2$ added to an accurately measured total pressure of order 20 mbar. Subsequently pumping the cell to a lower pressure, which was measured accurately using the capacitance manometer enabled a lower partial pressure to be reached than would be the case with pure CO. A background gas, containing 13.3 mbar $N_2O$, 11.82 mbar $C_2H_2$ and 2.24 mbar $N_2$, was added to the small amount of CO. Spectra were recorded for this sample and then after the step-wise addition of further CO; the resulting MUMAS spectra for variable amounts of CO are shown in Figure 5.10.

The feature at ∼6 GHz on the scan is due to CO, with a portion of the absorption

causing the "shoulder" on the lower frequency side arising from the background gas. The figure shows MUMAS scans for five different partial pressures of CO: 0.193 mbar, 0.917 mbar, 1.63 mbar, 2.97 mbar and 5.18 mbar. The highest CO concentration is clearly visible as the solid line with the strongest feature at ∼6 GHz. The other lines correspond to successively decreasing concentrations of CO with correspondingly decreasing strengths of this feature with the lowest also shown as a solid line. The inset to the figure shows an expanded view of the spectrum for the lowest concentrations of CO and also a background level for zero CO concentration. Due to the dilution procedure by which the initial CO sample was produced, it was not possible to directly record a MUMAS spectrum of just the "background" species in the absence of CO. Hence this background level, shown as the solid red line is a modelled MUMAS spectrum for zero CO concentration fitted to the data in regions outside the feature at 6 GHz i.e. this represents the best fit MUMAS spectrum to the data if there was no CO present and provides a "baseline" for measurement of the CO concentration.

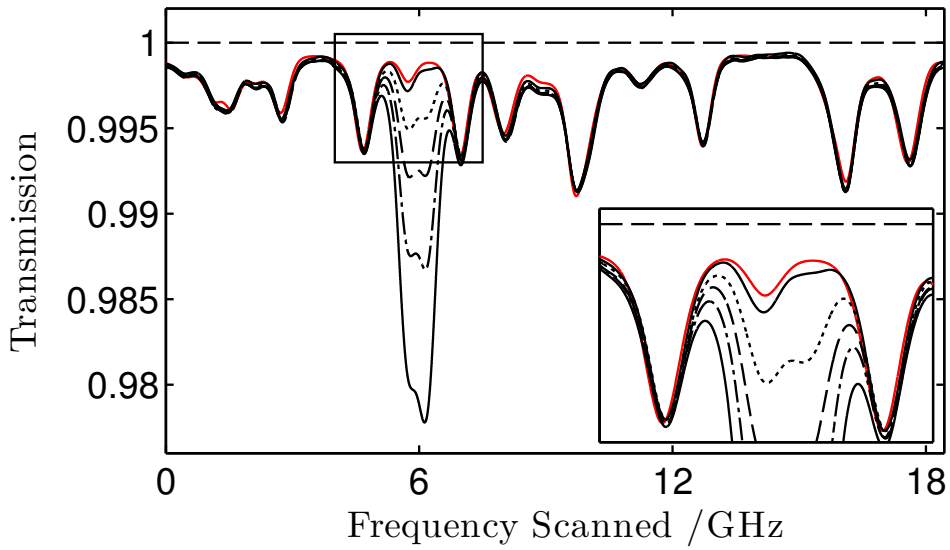


**Figure 5.10:** MUMAS spectra of a gas mixture containing $N_2O$, $C_2H_2$ and $N_2$ with increasing concentrations of CO, for details see text. The horizontal dashed line indicates the zero absorption level. The inset presents an expanded view of the spectra showing the CO absorption feature at the two lowest concentrations: 0.193 mbar (thick solid line) and 0.917 mbar (dotted line). The background absorption in the absence of CO is indicated by the thin solid red line (see text). *n.b.* The shape of the spectra in this figure are different to those plotted in Figures 5.6 and 5.8 due to a change in the laser comb envelope shape and central frequency.

## 5.5 Conclusions

This chapter has reported the first application of multi-mode absorption spectroscopy to multi-species detection. A multi-mode laser and simple spectroscopic equipment has been used to simultaneously detect multiple transitions from three molecular species. A modelled spectral fit allowed the partial pressures of three components of a mixture to be determined with an uncertainty less than $\pm 2$ %.

To carry out this work an experimental spectrometer was constructed to acquire MUMAS traces at a wavelength of around 1565 nm. The parameters of the multi-mode laser comb were determined to a high level of precision through a combination of direct measurement and by means of inference from recorded interferograms and spectra. As part of this, a new method to determine the comb mode spacing through analysis of an interferogram with a Fabry-Perot etalon was developed. Fitting software has been written for this work, and used in conjuction with pre-existing fitting functions to allow analysis of MUMAS spectra.

Initially, pure samples of CO, $N_2O$ and $C_2H_2$ were probed. Spectra recorded with these samples allowed unambiguous identification of these species through the assignment of multiple transitions and served to verify the operation of the experimental MUMAS spectrometer.

Multi-species detection was demonstrated with mixtures comprising the same three molecular species. The MUMAS technique allowed not only the simultaneous identification of these three species but also the selective and quantitative measurement of concentration of the components of a mixture and hence the overall mixture composition.

# Chapter 6

# Mid-IR MUMAS

## 6.1 Overview

This chapter reports the first application of MUMAS to spectroscopy in the mid-IR spectral region, allowing access to the stronger transitions found at these wavelengths. This demonstration was achieved through the construction and application of a QPM-DFG system to mix the output of the Er/Yb multi-mode laser with the single mode output of a Nd:YAG laser operating at 1064 nm, thus producing a mid-IR laser comb around 3.3 $\mu$m. Multi-mode absorption spectroscopy of methane and ammonia was carried out to test the utility of this mid-IR multi-mode source for MUMAS measurements, and also to determine the feasibility of performing MUMAS at these longer wavelengths.

## 6.2 Motivation

The mid-infrared spectral region (mid-IR) – typically defined as wavelengths between 2.5 and 25 $\mu$m – is an attractive target for trace gas detection due to the wealth of strong spectral lines occurring there. These lines arise from fundamental vibrational transitions, and consequently the large transition dipole moment integral between the

ground state and the upper state gives these absorptions far larger absorption cross-sections than the overtone and combination bands found at shorter wavelengths. Thus, a measurable reduction in the intensity of transmitted light can be produced from very small concentrations of absorber molecules, lending high sensitivity to absorption spectroscopy.

The spectral region around 3 $\mu$m is of particular interest as the fundamental X-H stretching modes are found here. This allows a wide range of molecules to be selectively and sensitively detected due to the ubiquity of hydrogen-containing functional groups such as C–H, N–H and O–H. In addition the spectral region 2.9 — 5.3 $\mu$m is referred to as the first atmospheric sensing window due to the lack of interfering transitions from atmospheric absorbers, allowing unimpeded detection of trace species [103]. It was therefore decided to carry out MUMAS in the mid-IR to access stronger transitions, with particular interest in detecting hydrocarbons using spectral lines found in the 3 – 4 $\mu$m region.

Despite the attraction of the mid-IR region for spectroscopic gas detection, development in this field has been restricted due to a lack of suitable radiation sources. Spectroscopic gas detection requires radiation that has suitable properties, such as narrow linewidth, wide tunability, good beam quality, and a suitable power output. In addition if a gas sensor is being developed with intentions of deployment as a field instrument then the source must also be robust, compact, and able to operate unattended for long periods of time.

While mid-IR radiation suitable for spectroscopy can be produced by several different sources, few of these lend themselves to use in a deployed sensor [104, 105]. Gas lasers, such as those operating on $CO_2$ or CO transitions can produce mid-IR radiation with high output power, enabling sensitive techniques such as photo-acoustic spectroscopy to be employed, but they are typically large and have limited continuous tunability. Diode lasers based on group IV-VI semiconductors have been used for lab-based spectroscopy

for many years but suffer from limited output power (at most a few mW), poor reliability, and require cryogenic cooling, making them unsuitable for use in the field (for example [106]).

The first demonstration of a quantum cascade laser (QCL) in 1994 [107] and the subsequent rapid development of these devices has opened a new era in mid-IR spectroscopy [108–110]. QCLs are now extremely versatile radiation sources, capable of room-temperature continuous wave (CW) operation [111] at wavelengths spanning the majority of the mid-IR ($\sim$4 — 20 $\mu$m). The semiconductor fabrication of QCLs also allows the use of mature side-mode suppression schemes developed for near-IR diode lasers (*e.g.* integrated grating structures and external cavity configurations) to produce reliable, single-mode, narrow linewidth lasers. Such devices have found widespread applications in spectroscopy using a variety of detection schemes [108, 109, 112–114], and the small size and robust construction of QCLs has made them suitable for use in deployed trace gas sensors [106, 115–119]. However, the tuning range of QCLs limits the applicability of any particular device to a small wavelength region and these devices typically suffer from poor beam quality. In addition, the shortest wavelengths achievable with QCLs are limited by the height of the conduction band offset between the heterostructure materials, a fundamental property of the semiconductors used for construction [104]. In the case of the semiconductors currently used, this limits the shortest emission wavelength to around 3.4 $\mu$m, precluding access to a large portion of the hydrogen stretching bands. Recent developments, including the advent of interband cascade lasers (ICLs) look to improve on this limitation [120].

Non-linear parametric frequency conversion of near-IR sources provides an alternative and more established method to produce mid-IR radiation. These methods allow radiation to be produced that inherits the high spectral quality from the well developed and convenient near-IR lasers used to provide the input. The more recent realisation of quasi-

phase matching (QPM) using engineered materials such as periodically-poled lithium niobate (PPLN), has now led to high-efficiency, and thus practicable generation of mid-IR radiation [105]. The controlled and reproducible manner in which these materials can now be manufactured has made these sources relevant for spectroscopy [103]. A particular advantage of this method of light generation is the ability to produce radiation throughout the 2.5 — 5 $\mu$m region, allowing access to the fundamental hydrogen stretching modes around 3 $\mu$m that are difficult to target with current QCL technology.

Non-linear mid-IR sources are typically separated into two classes, typically referred to as difference frequency generation systems (DFG) and optical parametric oscillators (OPOs), where OPO refers to the case when the non-linear process occurs within a resonant cavity, enhancing the efficiency, and DFG refers to the single-pass process. Both methods share the advantages of being stable, coherent sources of mid-IR radiation with good spectral quality [105]. Continuous wave OPOs typically produce high power radiation with wide tunability, but do so at the expense of a complex and sensitive design, and relatively broad linewidth, reducing their utility for applied trace gas sensing.

DFG systems maintain the potential for wide tunability using simpler and more compact equipment, albeit with the trade off of reduced output power (typically $\mu$W compared to mW—W for OPOs). When implemented with compact diode or solid-state pump and signal lasers, DFG systems have the potential to be used as relatively compact, high quality mid-IR sources for spectroscopy, shown by the wide variety of applications [121–126]. The recent development of fibre-coupled, waveguide PPLN has further improved the efficiency and simplicity of DFG sources, making them more attractive for spectroscopy [127–129].

Having reviewed the options for mid-IR radiation sources, it was decided that quantum well lasers (*i.e.* QCLs or ICLs) and DFG would be the two most fruitful avenues to explore to produce a mid-IR laser comb suitable for high-sensitivity MUMAS. Direct

comb generation with a quantum well laser source would have the advantage of producing a compact spectroscopic system but it was unclear whether the output of these sources would meet the requirements for MUMAS laid out in Section 3.4. These sources are usually optimised for single-mode operation and so a less common, Fabry-Perot device would be required which would need extensive testing and characterisation to verify performance. DFG comb generation, mixing the output of a single-mode laser with the multi-mode comb produced by the Er/Yb laser has the advantage of adopting the characteristics of the Er/Yb laser produced for near-IR MUMAS in Chapter 4. In addition, when mixed with the fundamental output of a single-mode YAG laser ($\lambda =$ 1064 nm) this would produce a multi-mode laser comb at a wavelength close to 3.3 $\mu$m, allowing access to the strong hydrocarbon vibrational transitions in this region.

It was therefore decided to develop a QPM-DFG system to allow MUMAS to be performed in the mid-IR. This demonstration of principle prepares the ground for MUMAS with future mid-IR sources. The development process, and the subsequent mid-IR MUMAS spectroscopy is described in this chapter. Future work, discussed in Chapter 7, will focus on testing the feasibility of QCLs and ICLs for mid-IR multi-mode comb generation.

## 6.3 Non-linear optics

DFG is a second order non-linear optical process. The underlying non-linear optics will now be introduced and used to explain this method of mid-IR generation.

When light passes through a dielectric medium, a response is induced in the atoms that make up that material. At a microscopic level this consists of a perturbation to the electron density distribution of individual atoms, driven by the electric field of the radiation, leading to an instantaneous separation of charges and therefore an induced

dipole moment. When this effect is viewed in a macroscopic sample the dipole moment per unit volume is termed the induced polarisation, which, for low field strengths, is found to be proportional to the electric field strength of the radiation (Equation 6.1). In this regime the induced dipole present in the medium is found to oscillate at the same frequency as the driving field, and the magnitude of the response of the medium is described by a single constant, the susceptibility of the medium, $\chi^{(1)}$, which describes the ability of dipoles within the sample to respond to the electric field. This linear susceptibility gives rise to linear optics and effects such as reflection and refraction.

$$P(\mathrm{t}) = \epsilon_0 \, \chi^{(1)} \, E(\mathrm{t}) \tag{6.1}$$

At higher field intensities, the response of a dielectric medium is more complex and the induced dipole moment saturates, no longer simply following the driving field. This situation, which typically can be generated only by the intensity of laser radiation, requires a more generalised form of Equation 6.1 to describe the induced polarisation. In this case the polarisation induced in a medium by an electro-magnetic wave is better described by a power series, given as:

$$\begin{aligned} P(\mathrm{t}) &= \epsilon_0 \left[ \chi^{(1)} \, E(\mathrm{t}) + \chi^{(2)} \, E(\mathrm{t})^2 + \chi^{(3)} \, E(\mathrm{t})^3 + ... \right] \\ &= P(\mathrm{t})^{(1)} + P(\mathrm{t})^{(2)} + P(\mathrm{t})^{(3)} + ... \end{aligned} \tag{6.2}$$

where $\chi^{(n)}$ are the $n$-th order susceptibilities of the medium, and $E(\mathrm{t})$ the time-dependent electric field [130]. This series can be seen as describing the first order polarisation, $P(\mathrm{t})^{(1)}$, that gives rise to familiar linear optical effects, and then the higher order, non-linear polarisation terms ( $P(\mathrm{t})^{(\mathrm{NL})} = P(\mathrm{t})^{(2)} + P(\mathrm{t})^{(3)} + ...$) that give rise to non-linear optical phenomena. The non-linear polarisation terms allow frequency components not present

in the driving field to arise in the induced polarisation.

The importance of the induced polarisation to a description of DFG is due to the ability of a time-varying polarisation to act as a source of new components of the electromagnetic field. This can be understood by reverting to the microscopic view of the polarisation – atomic dipoles driven by the light field. As these charges are accelerated by the driving field, electromagnetic radiation is emitted. By invoking Maxwell's equations in a non-magnetic material, without free charges or currents, a wave equation can be used to describe the parts of this process arising due to non-linear polarisation [130]:

$$\nabla^2 E - \frac{n^2}{c^2}\frac{\partial^2 E}{\partial t^2} = \frac{4\pi}{c^2}\frac{\partial^2 P^{(\mathrm{NL})}}{\partial t^2}\,. \tag{6.3}$$

where $n$ is the refractive index and $c$ the speed of light in vacuum.

### 6.3.1 Second order non-linear processes

The physical processes that arise as a result of the higher order terms in Equation 6.2 can be considered separately. This chapter focuses on a particular second order non-linear process, difference frequency generation (DFG), that is used to generate mid-infrared radiation for use in spectroscopy. DFG optically mixes incident radiation to produce an output wave with frequency given by the difference between the the two input frequencies. Therefore, the second-order response of a medium to a light field comprising two distinct frequency components is now considered.

A physical solution to the wave equation for an optical wave of a single frequency propagating along $z$ in an isotropic and homogeneous medium is given by

$$\begin{aligned} E(z,t) &= E_0 \cos(kz - \omega t) \\ &= A\, e^{i(kz-\omega t)} + A^*\, e^{-i(kz-\omega t)} \end{aligned} \tag{6.4}$$

where $A = E_0/2$ and $E_0$ is the amplitude of the electric field, $k = (n\omega/c)$ the propagation wavevector and $\omega$ the angular frequency. Therefore an optical field containing two distinct frequencies can be represented by the sum of two such terms:

$$E(z,t) = E_1\, e^{i\omega_1 t} + E_2\, e^{i\omega_2 t} + c.c.\,. \tag{6.5}$$

with

$$E_q = A_q e^{ik_q z}, \quad q = 1, 2. \tag{6.6}$$

When an intense field comprising two frequency components is incident on an optical medium a non-linear polarisation is induced in accordance with Equation 6.2. The second-order term is given by [130]:

$$\begin{aligned} P^{(2)}(\omega) &= \epsilon_0 \chi^{(2)} E^2(\omega) \qquad (6.7)\\ &= \epsilon_0 \chi^{(2)} \Big[ E_1^2 e^{-2i\omega_1 t} + E_2^2 e^{-2i\omega_2 t} + c.c. \qquad \text{(SHG)}\\ &\quad + 2E_1 E_2 e^{-i(\omega_1+\omega_2)t} + c.c. \qquad \text{(SFG)}\\ &\quad + 2E_1 E_2^* e^{-i(\omega_1-\omega_2)t} + c.c. \qquad \text{(DFG)}\\ &\quad + 2\left(E_1 E_1^* + E_2 E_2^*\right) \Big]. \qquad \text{(OR)} \end{aligned}$$

from which it can be seen that, in addition to a component with no frequency dependence, new components of the non-linear polarisation arise at four different frequencies ($2\omega_1$, $2\omega_2$, $(\omega_1 + \omega_2)$ and $(\omega_1 - \omega_2)$), each with the potential to generate radiation. These new frequencies are linked to distinct physical processes, named second harmonic generation (SHG), sum frequency generation (SFG) and difference frequency generation (DFG). The last component, named optical rectification (OR), corresponds to creating a static field within the medium.

Typically, radiation will only be produced with appreciable intensity at one frequency, due to an additional *phase-matching* condition (discussed in Section 6.3.3) that can be satisfied only for one component of the non-linear polarisation. In practice the phase matching condition is used to maximise production of the desired frequency and suppress others.

### 6.3.2 Difference frequency generation

Difference frequency generation (DFG) is a non-linear process arising from the second-order polarisation term, that can occur when two intense input fields are brought together in a suitable crystal. It is of particular interest to spectroscopists due to its use in generating coherent, narrow linewidth radiation in the mid-IR – a region traditionally difficult to reach with laser sources.

DFG occurs when a light field containing two frequency components, termed the *pump* and *signal* waves (having frequencies $\omega_p$ and $\omega_s$ respectively) is incident on a medium with non-zero second-order susceptibility*, $\chi^{(2)}$ (Figure 6.1(a)). As can be seen from the photon energy level description in Figure 6.1(b) the DFG process corresponds to the absorption of a high energy photon from the pump beam, promoting an atom into a virtual energy level. This state then decays in a two-photon emission process that is stimulated by the presence of the $\omega_s$ field, producing photons of frequency $\omega_s$ and $\omega_i$, amplifying the signal field and generating radiation at the idler frequency. The generated wave, termed the *idler* is produced at a frequency corresponding to the difference between the frequencies of the incident waves *i.e.* $\omega_i = \omega_p - \omega_s$.

The intensity of the idler wave produced by the DFG process can be calculated through consideration of the coupling of the three waves involved in the generation. If a low-loss non-linear medium is considered, onto which the pump and signal plane waves

*only possible for crystals that have a structure with no spatial inversion symmetry

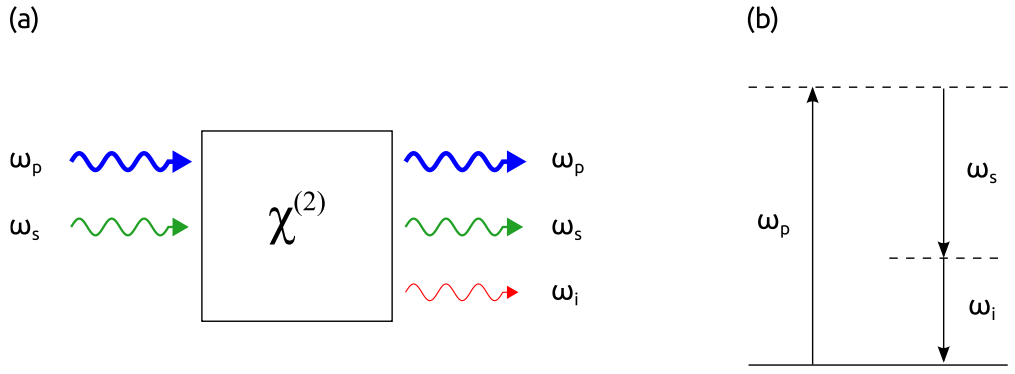


**Figure 6.1:** The DFG process. **(a)** Schematic diagram of the interaction. **(b)** Energy-level description.

are incident, propagating in the $+z$ direction, the non-linear source term at the idler frequency can be written:

$$P_i(z,t) = 4d_{eff}A_pA_s^*e^{i[(k_p-k_s)z-\omega_i t]} + c.c. \tag{6.8}$$

where $d_{eff}$ is the non-linear susceptibility tensor chosen for the interaction, a property of the medium and the interaction geometry, and $A_p$, $A_s$ the amplitude of the pump and signal fields. This polarisation will produce a plane wave at the idler frequency, which can be represented by

$$E_i(z,t) = A_i(z)e^{i(k_iz-\omega_i t)} + c.c.\,. \tag{6.9}$$

If Equations 6.8 and 6.9 are then substituted into the wave equation (given in Equation 6.3), under the conditions of slowly varying amplitude and an undepleted pump wave ($A_p$ being constant), the growth of the idler wave along the $z$-axis is found to be

$$\frac{dA_i}{dz} = \frac{8\pi\, i\, d_{eff}\omega_i^2}{k_i\, c^2}\, A_p\, A_s^*\, e^{i\Delta kz} \tag{6.10}$$

where

$$\Delta k = k_p - k_s - k_i \tag{6.11}$$

is known as the *wavevector mismatch* parameter. It is then possible to calculate the idler field amplitude present at the exit plane of a crystal of length, $L$, by integrating this expression from $z = 0$ to $z = L$. By defining the intensity of this wave as the magnitude of the time-averaged Poynting vector:

$$I_q = \frac{n_q\, c}{2\pi}|A_q|^2, \quad q = p, s, i \tag{6.12}$$

it is then possible to obtain an expression for the intensity of idler radiation expected to be produced in a particular nonlinear crystal, given by

$$I_i = \frac{512\,\pi^5\, d_{eff}^2}{n_p\, n_s\, n_i\, \lambda_i^2 c}\, I_p I_s\, L^2\, \mathrm{sinc}^2\left(\frac{\Delta k L}{2}\right) \tag{6.13}$$

where $\mathrm{sinc}(x) = \sin(x)/x$. This expression describes the generated idler intensity as being dependent upon the intensity of the incident pump and signal fields, but also upon the wavevector mismatch parameter with a $\mathrm{sinc}^2(\Delta k L/2)$ dependence, corresponding to a phase requirement for the DFG process, which is described further in the next section.

### 6.3.3 The phase matching condition

In common with other non-linear processes like second harmonic generation (SHG), the efficiency of idler generation in DFG is critically dependent on a "phase matching condition". Conceptually, this amounts to ensuring that the idler radiation produced maintains a fixed phase relationship with the input fields as it propagates through the medium, allowing energy to be efficiently coupled into the idler field. From the microscopic viewpoint, the phase matching condition corresponds to the collective behaviour of the

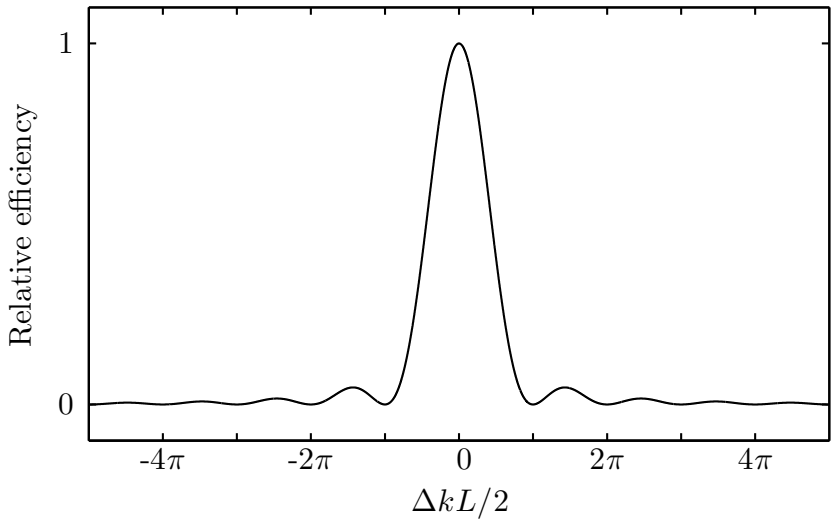


**Figure 6.2:** The dependence of DFG conversion efficiency on the phase mismatch parameter, $\Delta k$.

individual atomic dipoles making up the medium – only a perfectly phased array of oscillating dipoles will lead to each individual contribution to the idler field adding constructively along the beam propagation axis.

To achieve perfect phase matching the value of the wavevector mismatch parameter $\Delta k$ must equal zero. In this situation the amplitude of the idler field would be expected to grow linearly with $L$, the length of the interaction in the medium, or equivalently the intensity increases with $L^2$. Deviations from perfectly phased array behaviour, *i.e.* $\Delta k \neq 0$, result in dramatic reductions in the efficiency of idler generation, as is illustrated in Figure 6.2, which shows a sinc function.

Unfortunately, the desired phase matching condition is difficult to achieve in practice. Chromatic dispersion in the medium leads to a frequency dependence of the phase velocity, causing the three frequency components of the light field to accumulate a relative phase shift as they propagate along the interaction axis. Once a phase shift of $\pi$ has occurred, energy will start to flow from the idler field back into the pump field. Accumulated phase

shifts of $2\pi$ over the interaction length, $L$, lead to complete destructive interference of the idler wave – these points are apparent as minima in Figure 6.2. The distance required to generate a $\pi$-shift is defined as the coherence length, $L_c = \pi/\Delta k$.

Most optical materials exhibit normal dispersion, meaning that the refractive index is an increasing function of frequency. This would suggest that the phase matching condition can never be achieved, as for $\Delta k$ to equal zero, the expression

$$n_p\omega_p = n_s\omega_s + n_i\omega_i \tag{6.14}$$

must hold true, which seemingly cannot be the case as the left side will always be larger due to the combination of

$$\omega_p = \omega_s + \omega_i \quad \text{and} \quad n_p > n_s, n_i\,. \tag{6.15}$$

To circumvent this apparent problem the dispersion properties of the medium must be carefully managed. One method of doing so that has been used extensively is to exploit the birefringence innate to optically anisotropic materials. *Birefringent phase matching* (BPM) aligns the polarisation of the incident waves so as to take advantage of the differing optical indices experienced by waves that are polarised parallel or perpendicular to a certain axis of the crystal. Fine control of the refractive indices at the three frequencies present is obtained by careful tuning of crystal temperature (non-critical phase matching) or incidence angle (critical phase matching).

A more modern solution to the problem called *quasi phase matching* uses an engineered material, in which the structure of the crystal is periodically modified. This scheme ensures that the contribution to the idler field accumulated over each coherence length ($L_c$) does not cancel with that generated over the preceeding $L_c$. One widely used

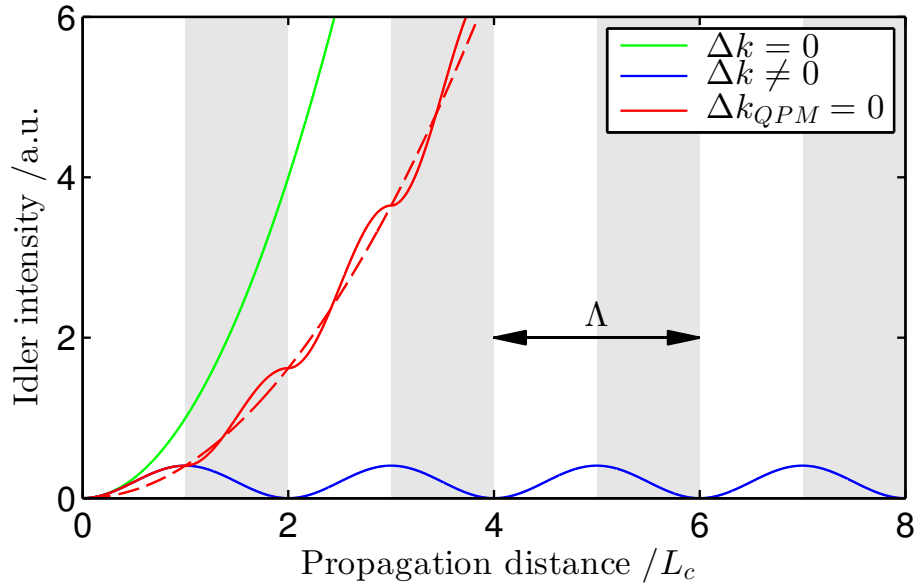


**Figure 6.3:** The growth in the intensity of DFG idler radiation with propagation distance through a non-linear medium for different phase matching regimes. First order quasi phase matching (red) is compared to the case of perfect phase matching (green) and a large wavevector mismatch (blue). It can be seen that QPM produces monotonic growth but at a slower rate than experienced in the $\Delta k = 0$ case. The poling period used for QPM is marked.

method to achieve this is the periodic poling of ferroelectric materials such as lithium niobate ($LiNbO_3$). Periodically poled lithium niobate (PPLN) is commonly produced by applying high voltages to photolithographically patterned electrodes on the crystal surface. The resultant spatially structured electric field can be used to flip the alignment of the permanent electric polarisation inherent to the material, and with it the orientation of $\chi^{(2)}$.

With care a material can be produced which is characterised by regions with the second order non-linear polarisation alternating between $+\chi^{(2)}$ and $-\chi^{(2)}$. If the period of these modulations, $\Lambda$, is set to be equal to twice the coherence length then just as a relative phase shift of $\pi$ has accumulated between the idler and driving fields (at $z = L_c$) the sign of $\chi^{(2)}$ is flipped leading to re-phasing (which is complete at $z = 2L_c$). This

results in continual energy flow into the idler field and therefore monotonic growth of the idler intensity through the crystal. *

In this scheme, the value of the wavevector mismatch parameter, $\Delta k$, corresponding to optimum idler generation is found to be shifted to negative values. If the periodic poling is described by a spatial "wavevector", defined

$$k_g = \frac{2\pi}{\Lambda} \tag{6.16}$$

then a new phase mismatch parameter can be defined

$$\Delta k_{QPM} = k_p - k_s - k_i - k_g \tag{6.17}$$

$$= \Delta k - k_g \tag{6.18}$$

so that maximal conversion efficiency again occurs for $\Delta k_{QPM} = 0$. The efficency of idler production using QPM shows the same sinc squared behaviour for deviations from $\Delta k_{QPM} = 0$ as is seen in the BPM case and that was plotted in Figure 6.2.

Figure 6.3 illustrates the evolution of idler intensity along the propagation axis under different phase matching regimes. The rate of idler growth in the QPM interaction is compared to the cases of perfect phase matching, and a large wavevector mismatch. In the case of perfect phase matching the idler intensity exhibits quadratic growth *i.e.* the field amplitude shows a linear dependence on $L$. In the mismatched case the idler intensity is seen to oscillate close to zero, illustrating the flow of energy backwards and forwards between the light fields, the result of cycles of constructive and destructive interference. The QPM interaction is also characterised by oscillations, however, in this

*The described process is first order QPM. It is also possible to carry out QPM by reversing $\chi^{(2)}$ with a different period, for example third-order QPM sets $\Lambda = 3L_c$. These higher-order QPM schemes have a reduced efficiency compared to the 1$^{st}$ order process – due to non-continual idler growth – but have other advantages such as the reduced manufacturing difficulty of structured materials with larger domain sizes.

case the intensity oscillates around an underlying trend of quadratic growth due to the constant constructive interference with the driving non-linear polarisation component.

Due to the non-perfect phase matching experienced at propagation distances other than $z = 2mL_c$ ($m = 1, 2, 3...$) the idler intensity produced for first order QPM is reduced to $(2/\pi)^2$ of the value expected in the $\Delta k = 0$ case [131]. Therefore it may seem that QPM is liable to exhibit a lower conversion efficiency than that which may be obtainable in birefringent phase matching. However, the freedom to align the polarisation of the input beams to the crystal axis with the greatest non-linear coefficient, and the lack of walk-off inherent to this non-critical (co-linear) process often provides a greater efficiency to QPM than an equivalent BPM process. In addition quasi phase matching can be achieved for virtually any wavelengths of light for which a suitable non-linear material can be obtained rather than relying on finding the conditions needed to make $\Delta k = 0$ for BPM.

When QPM is carried out experimentally, it is prohibitive to obtain PPLN crystals with poling periods tuned to achieve phase matching for each different wavelength DFG process. Therefore PPLN crystals are often supplied containing multiple tracks, each poled with a different period. To achieve phase matching for a DFG process with any particular input wavelengths the available poling period giving the best phase matching is chosen, and the temperature of the crystal is tuned so as to modify the optical index of the crystal, thus maximising the efficiency.

### 6.3.4 DFG with focused Gaussian beams

The above discussion of the DFG process has assumed that all interacting waves are behaving as plane waves *i.e.* waves characterised by parallel phase-fronts of infinite transverse extent. In practice, the radiation involved in DFG is likely to be in the form of narrow laser beams, with Gaussian transverse intensity distributions. When such beams

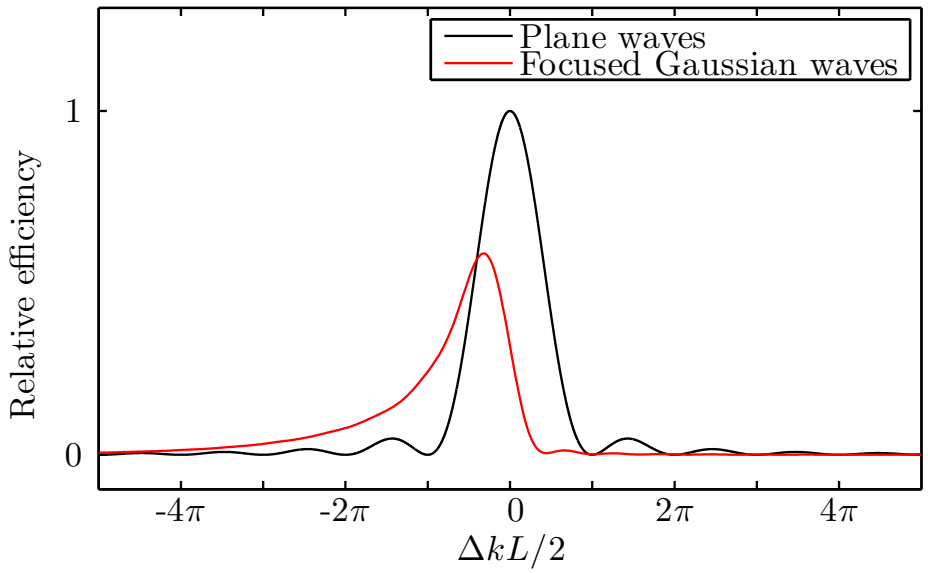


**Figure 6.4:** The dependence of DFG conversion efficiency on the phase matching condition for plane waves and focused Gaussian waves.

are focused – as is required in practical DFG due to the intensity dependence of the process – the wavefronts exhibit curvature.

Such behaviour results in a modification of the optimum phase to maximise DFG efficiency [132–134]. The perfect $\mathrm{sinc}^2$ dependence of efficiency on $\Delta k_{QPM}$ that is expected in the plane wave case is replaced by an asymmetric function, which is strongly broadened and the maximum efficiency is reduced. It is seen that the optimum phase matching condition is shifted from $\Delta kL/2 = 0$ to negative values. Figure 6.4 illustrates this difference in phase dependence for plane and focused Gaussian waves.

## 6.4 Experimental DFG system

### 6.4.1 Design

An experimental DFG system was designed and constructed to produce a mid-IR laser comb for use with MUMAS. This system mixes single-longitudinal-mode radiation from a Nd:YAG laser at 1.064 $\mu$m with a multi-mode laser comb, produced by the Er/Yb:glass laser described in Chapter 4. Independent non-linear interactions between each component of the comb and the single YAG laser frequency transfer the comb to longer wavelengths.

When designing and constructing this DFG system it was important to consider the acceptance bandwidth of the PPLN crystal to ensure that the entire range of frequencies contained in the comb were efficiently converted to mid-IR frequencies. For this reason simulations were carried out to determine a suitable length of non-linear crystal, and this resulted in the use of a short length of PPLN ($L = 20$ mm). Waveguided PPLN, such as that used by [127–129] was considered due to the much higher efficiency of the waveguided DFG process, however, this was not chosen due to bandwidth concerns and availability problems.

The design, construction, and characterisation of the experimental DFG system are described in the section below.

#### Layout

Figure 6.5 illustrates the layout of the experimental DFG system used to produce a mid-IR laser comb. The multi-mode comb is generated by the same Er/Yb:glass laser described in Chapter 4 and used for spectroscopy in Chapter 5. This laser produces a comb centred around 1565 nm, containing 6 — 10 modes, and provided the signal wave for the DFG interaction. The output is optimised for DFG by maximising the output power (to a measured 46 mW) and reducing the spectral bandwidth of the laser comb

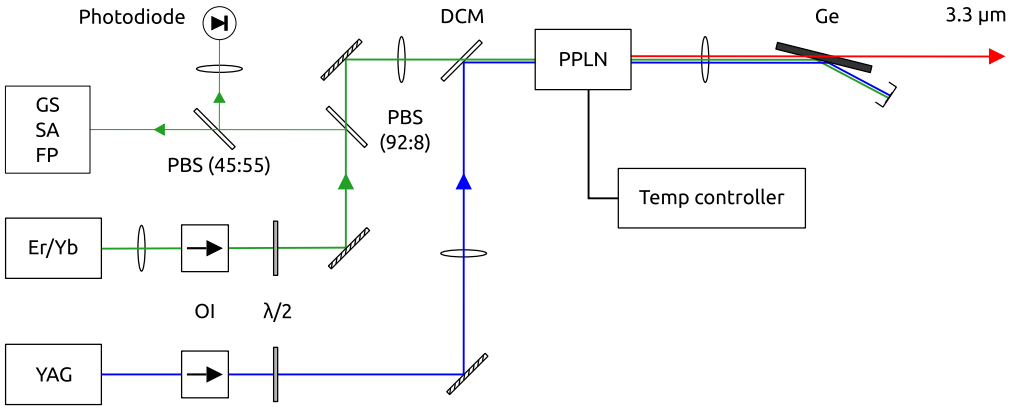


**Figure 6.5:** The experimental design used to produce a mid-IR laser comb. Er/Yb represents the Er/Yb:glass multi-mode laser; YAG, Nd:YAG DPSS laser; GS, grating spectrometer; SA, spectrum analyser; FP, Fabry-Perot etalon; OI, optical isolator; $\lambda/2$, half-wave plate; PBS, pellicle beam splitter (marked with split ratio); DCM, dichroic mirror; PPLN, periodically-poled lithium niobate crystal mounted in oven; Ge, germanium filter mounted at Brewster's angle. Laser beams of different wavelengths are displaced for clarity, in reality all are co-linear. Further details are provided in text.

(to 103 GHz), with the aim of transferring the maximum power into each mid-IR mode. As before, the output of this laser is collimated with a 75 mm AR-coated, plano-convex lens and passed through an optical isolator to reduce the destabilising effects of optical feedback. A fraction of this beam is diverted to monitor power and to allow on-line diagnostics with the same spectrum analyser, grating spectrometer and etalon as used previously and detailed in Chapter 5.

Pump radiation is provided at 1064 nm by a diode-pumped, single-longitudinal mode Nd:YAG laser (CrystaLaser CL1064-500-S), with a linewidth of less than 3 MHz. This laser is also isolated from optical feedback (Thorlabs IO-3D-1064-VLP) and the polarisation axis of both this, and the multi-mode beam are aligned onto the PPLN crystal axis using half-wave plates.

The two input beams are combined with a dichroic mirror and directed into the periodically-poled lithium niobate crystal (Covesion MOPO-20) where the non-linear

interaction occurs. This crystal is of length 20 mm and poling-periods between 28 and 32 $\mu$m are provided in 9 tracks of cross-section 0.5 $\times$ 0.5 mm. A commercial temperature controlled oven with a quoted stability of $\pm 0.1$°C maintains the crystal at the temperature necessary to achieve optimal phase matching. Both input and output facets of the non-linear crystal are anti-reflection coated for all three wavelength ranges present (R <1.5% for 1064 nm, <1% for 1400 — 1800 nm, 3 — 6% for 2600 — 4800 nm).

After the PPLN the three diverging beams are collimated with a plano-convex, AR-coated, $CaF_2$ lens of focal length 100 mm. The unconverted pump and signal light is then separated from the mid-IR idler with a Ge filter. Initially, an AR-coated germanium filter was used (Edmund Optics), however, this was found to introduce a etalon-like modulation onto the the transmitted signal. Therefore this was replaced with an uncoated, large diameter piece of germanium (Crystran) held at Brewster's angle and aligned with the idler polarisation to minimise surface reflections, and hence reduce optical interference. Due to to the high optical index of germanium a custom mount was required to achieve this steep angle ($\sim 76°$).

### Mode matching

The pump and signal beams are both focused into the PPLN with AR-coated plano-convex lenses, the focal lengths of which were carefully chosen to optimise performance.

The maximum efficiency and bandwidth of DFG carried out with focused Gaussian beams is dependent on the wavevector mismatch parameter, $\Delta k_{QPM}$, but also on a focusing parameter, $\zeta$, defined:

$$\zeta = L/b \tag{6.19}$$

where $b$ is the confocal parameter of the focused Gaussian beams [133]. The highest theoretical non-linear conversion efficiency occurs for a value of $\zeta_{opt} = 2.84$ [132, 133],

however, values of $\zeta$ closer to 1 are often used in practice as this slower focus reduces the sensitivity of the alignment required between pump and signal beams. This condition applies to both input beams ($b_p = b_s$).

It is possible to calculate the dependence of DFG conversion efficiency on wavevector mismatch and focusing parameter using a theoretical focusing function provided by Chu and Broyer [135] and generalised by Borri *et.al.* [134]. This focusing function, $h$, is defined

$$h\left(\zeta,\sigma,\mu,\alpha,l\right) = \frac{e^{-\frac{\alpha l}{2}}}{4\zeta} \times \int_{-\zeta}^{\zeta} d\tau \int_{-\zeta}^{\zeta} d\tau' \, e^{-i\sigma(\tau-\tau')+\frac{\alpha l}{4\zeta}(\tau-\tau')} \times \frac{1}{1+\tau\tau'-i\frac{1+\mu^2}{1-\mu^2}\left(\tau-\tau'\right)} \tag{6.20}$$

where $\zeta$ is the previously defined focusing parameter, $\alpha$ the absorption coefficient for the non-linear medium, and $b$ the confocal parameter for both input beams. A slightly modified phase mismatch parameter, $\sigma$, is defined

$$\sigma = \pi b\left(\frac{n_p}{\lambda_p} - \frac{n_s}{\lambda_s} - \frac{n_i}{\lambda_i} - \frac{1}{\Lambda}\right) = -\frac{b}{2}\Delta k_{QPM} \tag{6.21}$$

where $\lambda_x$ and $n_x$ are the wavelength and refractive index corresponding to each frequency component of the light fields respectively, and $\Lambda$ is the poling period of the engineered material used for QPM. According to this model the power conversion efficiency of the DFG process is given by

$$\frac{P_i}{P_p\,P_p} = \frac{32\pi^2 d_{eff}^2\, l}{\epsilon_0 c n_i \lambda_i^2\left(n_s\lambda_p + n_p\lambda_s\right)} \times h\left(\zeta,\sigma,\mu,\alpha,l\right) \tag{6.22}$$

where $d_{eff}$ is the effective non-linear coefficient, $l$ the crystal length and $P_x$ the power in each frequency component of the light field. Thus, for a given DFG interaction the dependence of the conversion efficiency on wavevector mismatch and focusing parameter is encapsulated in the focusing function, $h$.

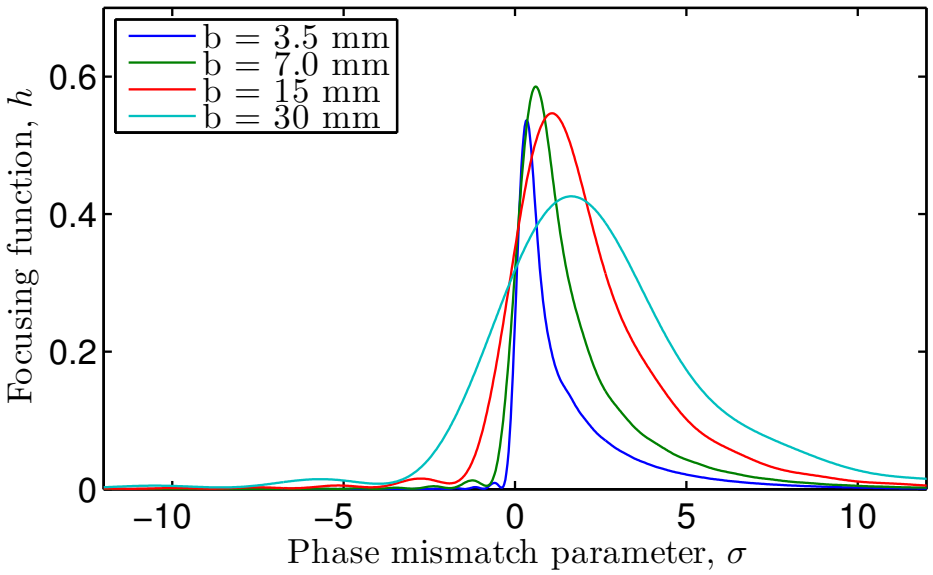


**Figure 6.6:** The dependence of the focusing function on phase mismatch parameter for a range of values of the confocal parameter. Full details are found in the main text.

Simulations were carried out following the method outlined in [136] to aid in the choice of confocal parameter for this system. The value of the focusing function was numerically evaluated over a range of values of $\sigma$ and $\zeta$. From Figure 6.6 it can be seen that the focusing function varies with the mismatch parameter in the expected asymmetric manner. The maximum value of $h$ is found to reduce for values of $\zeta$ both larger and smaller than the optimum value, which for this system with $L = 20$ mm is $b = L/\zeta_{opt} = 7.0$ mm. The wavelength bandwidth of the DFG process – represented here on the $\sigma$ axis – is seen to increase with higher values of $b$.

A value of the confocal parameter of $b = 15$ mm was chosen as giving a good compromise between high peak efficiency and large bandwidth, an important consideration for multi-mode comb generation. In addition, this choice of confocal parameter (and hence $\zeta$) is expected to make the DFG process less sensitive to optical alignment.

Producing focal waists with the desired confocal parameter in the non-linear medium

for both input beams requires careful choice of focusing lens position and strength. Ray matrix calculations were carried out to determine a propagation function describing the path of the beams between the focusing lenses and the centre of the PPLN crystal. Gaussian optics was then used to choose the most suitable focal length and position of the focusing lens for each beam using knowledge of the beam diameters obtained through knife-edge measurements.

### Phase matching

DFG is an intrinsically inefficient process and so to produce appreciable mid-IR radiation from an experimental system – which is important to achieve detection with good signal-to-noise – it is vital to optimise the phase matching parameters. This is achieved through careful choice of poling period and crystal temperature for the case of DFG with pump and signal waves of given input frequencies, using QPM in a PPLN crystal.

The poling period and temperature theoretically expected to give the optimum conversion efficiency were calculated using the focusing function described in [134]. For a chosen poling period of $\Lambda = 30.49$ $\mu$m the optimum temperature was calculated to be $T_{opt} = 101.9$ °C. Calibration measurements then were carried out to verify these predictions and to determine if further optimisation of the temperature would be necessary. To do this the PPLN crystal was translated to align the track with chosen poling period onto the input laser beams. The intensity of the idler radiation was then measured using the Vigo photovoltaic detector while the crystal temperature was varied over a wide temperature range spanning the predicted value.

The resultant measurements are shown in Figure 6.7, which displays the asymmetric sinc function expected for phase-mismatch in a second order non-linear process carried out with focused Gaussian fields. It should be noted that the width of the peak plotted here is wider than the same experiment conducted with a single-mode signal laser, and is

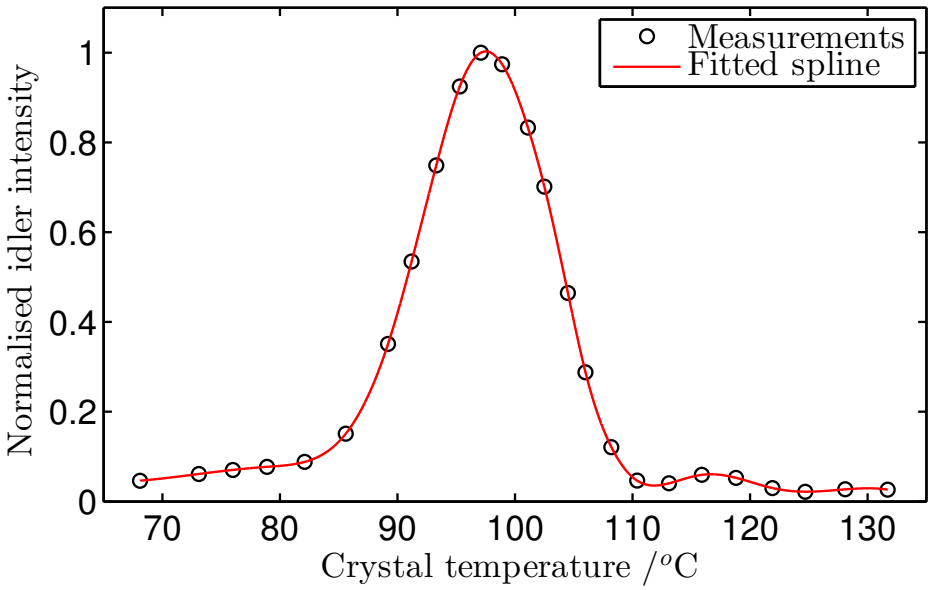


**Figure 6.7:** Experimental temperature tuning curve for this QPM-DFG system. The conversion efficiency of this non-linear process (viewed here as idler intensity) shows the expected asymmetric shape. Optimum idler production was found to occur for T = 98 °C.

expected to be reproduced by the convolution between the temperature tuning curve for a single-mode laser and the envelope function of the multi-mode laser. A spline was fitted to the data to allow interpolation and maximal output power is seen to be produced for a temperature of 98°C. The crystal was held at this optimal temperature for the remainder of the measurements. The difference between the measured and predicted values of $T_{opt}$ is thought to be due to inaccuracies in measuring the PPLN temperature and uncertainties in the specified poling period. It is noted that a deviation of less than 0.1% in the reported value of $\Lambda$ would account for this discrepancy.

### 6.4.2 Performance

#### Conversion efficiency

The conversion efficiency of an experimental DFG process can be calculated through comparison of the power contained in the input beams and in the mid-IR radiation produced. For this system the generated idler power was estimated using a HgCdTe photovoltaic detector with a stated responsivity of $1.9 \times 10^5 \pm 20\%$ V W$^{-1}$ for a 1 M$\Omega$ termination. A value of $P_i = 2.1 \pm 20\%$ $\mu$W was obtained. Using this value, and the power of the pump and signal beams, measured at the input facet of the PPLN as $P_p = 260$ mW and $P_s = 42$ mW respectively, the conversion efficiency of the non-linear process can be calculated as follows

$$\eta = \frac{P_i}{P_p P_s L_{PPLN}} \times 100 \tag{6.23}$$

in which $L_{PPLN}$ is the length of the PPLN crystal, in this case 20 mm. This gives a conversion efficiency for this system of $\eta = 9.6 \times 10^{-3}$ % W$^{-1}$ cm$^{-1}$.

This calculated efficiency is approximately four times lower than those obtained in a selection of recent DFG studies, such as those reviewed in Chapter 4 of Ciaffoni [136]. It is believed that this deficiency is partly due to the fundamental differences inherent to achieving efficient idler production across the entire bandwidth of the multi-mode comb.

#### Bandwidth

The bandwidth for this experimental DFG system was measured by substituting a single-mode DFB diode laser for the Er/Yb multi-mode laser. This allowed the conversion efficiency to be probed at discrete points with a narrow linewidth source, avoiding the complications of multi-point measurements with the multi-mode comb. Unfortunately

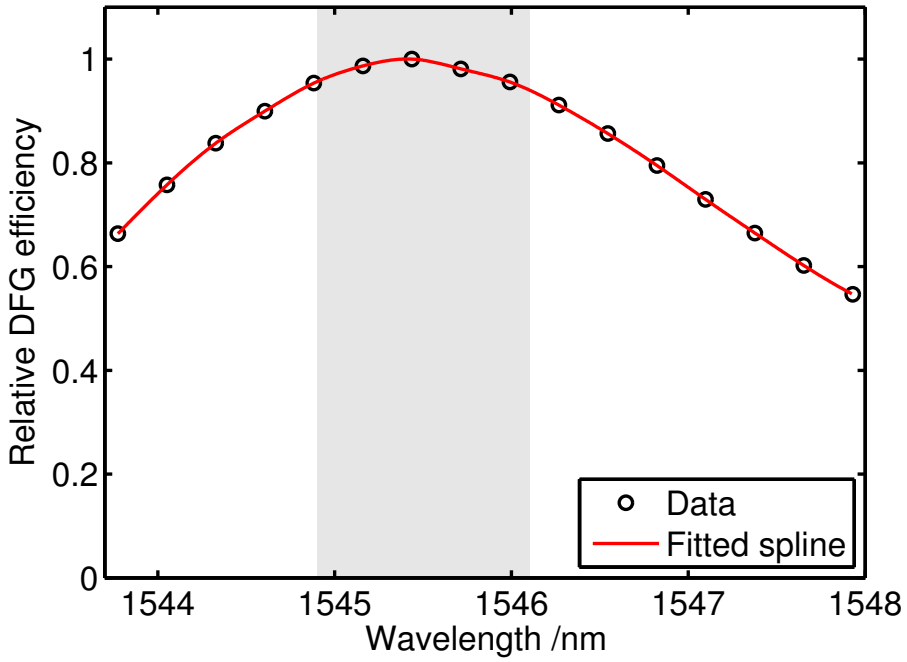


**Figure 6.8:** The bandwidth of the DFG process as measured by varying the frequency of the idler wave provided by a single-mode diode laser. The shaded area indicates the approximate bandwidth of the multi-mode laser used for spectroscopy in this chapter, over which there is <6% difference in conversion efficiency.

the available diode (3S Photonics 1905 LMI) operated around 1545 nm, 20 nm shorter in wavelength than the Er/Yb laser, however, the response of the PPLN in this region is expected to be comparable once the crystal temperature has been re-optimised.

To perform the measurements the diode laser was tuned in steps over a wavelength range of ∼4 nm by varying its temperature, and at each point the wavelength measured with a spectrum analyser (Bristol Instruments 721-B IR). The power of mid-IR radiation generated by DFG was measured with a thermo-electrically cooled HgCdTe photovoltaic detector (Vigo systems PVI-2TE-4). The intensity of the signal beam was also monitored by directing a small fraction onto a InGaAs photodiode (Thorlabs DET-410), and this signal was used to normalise the measured idler signal, hence producing a relative measure

of the efficiency of the DFG process as a function of wavelength.

The results of these measurements are shown in Figure 6.8, from which it can be seen that efficient idler generation is maintained across a broad spectral region; indeed the relative efficiency was not seen to drop below half the peak value over the range examined here, which was limited by the tuning range of the diode laser used for measurements. The shaded region marked on Figure 6.8 indicates the approximate spectral width of the multi-mode comb produced by the Er/Yb laser used in this chapter, and over this region there is <6% variation in measured efficiency. These results suggest that this system is more than adequate to produce a mid-IR laser comb for MUMAS, and further, that the shape of the output comb is expected to closely match that of the input comb, with only a small reduction in power of outlying modes due to non-optimal phase matching conditions.

**Generation of a mid-IR comb**

To confirm the experimental DFG system produced a mid-IR comb in the expected manner the frequency spectrum of a static multi-mode comb entering the PPLN was compared to the comb produced by the DFG process. To do this spectra of both beams were recorded using the same spectrum analyser (the Bristol Instruments 721-B IR). This process was aided by the simplicity of using a single spectrum analyser with the capability to record spectra at both widely separated wavelengths (1.5 $\mu$m and 3.3 $\mu$m), however, the large difference in power contained in the two beams necessitated sequential, rather than simultaneous, recording of the spectral information.

First, the mid-IR idler beam was carefully aligned into the spectrum analyser and a spectrum recorded as the average of 100 individual spectra, to aid the signal to noise ratio. This was necessary due to the extremely low power contained in the idler beam. Then, the output of the YAG laser was blocked and the germanium filter removed, to allow the

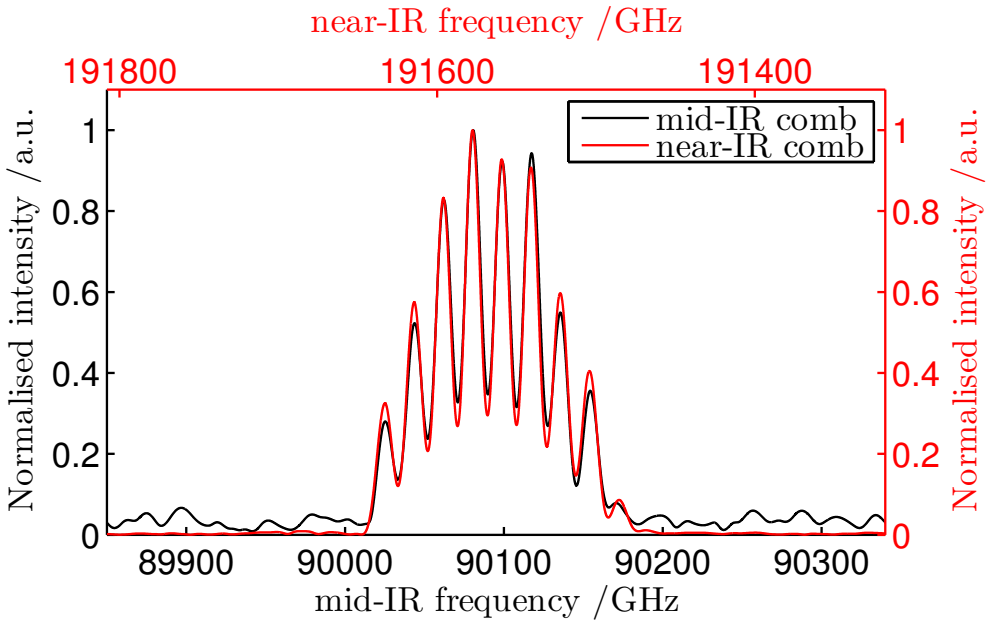


**Figure 6.9:** Measured spectra of the laser comb in the near-IR (prior to conversion) and in the mid-IR (post-conversion).

NIR radiation to continue to the spectrum analyser. A spectrum of the ∼46 mW signal beam was recorded in a single scan after attenuation to an instrument-safe power level.

The two spectra are plotted in Figure 6.9, with the near-IR spectrum shown as a red line and the mid-IR as a black line. In this figure the two frequency scales are linked by $\nu_i = \nu_p - \nu_s$, and therefore the value of the YAG laser frequency ($\nu_p = 281658$ GHz, or wavelength, $\lambda_p = 1064.38$ nm) can be determined to high accuracy by overlaying the two combs. It should be noted that two frequency scales run in opposite directions to account for the "mirroring" of the mid-IR comb relative to the input comb that results from the DFG process.

It can be seen from Figure 6.9 that, as expected, the DFG process produces a mid-IR comb that very closely resembles the input comb – all nine modes have been shifted to the mid-IR with their spacing and relative intensity maintained to a good degree. There

is a small reduction in power of the outlying modes of the mid-IR comb compared to the near-IR comb as is expected from the bandwidth of this DFG system (see Figure 6.8).

## 6.5 Experimental apparatus and procedure

Having constructed and tested a mid-IR multi-mode source proof-of-principle measurements were carried out to demonstrate the ability of this system to perform MUMAS measurements. Spectroscopy was performed with samples of ammonia and methane, both separately and mixed together to test the ability of DFG-MUMAS to perform quantitative measurements of mixture composition.

### 6.5.1 Apparatus

The experimental apparatus used for the experiments reported in this chapter is shown in Figure 6.10. This system uses the mid-IR laser comb produced by the DFG system described in Section 6.4 to record the MUMAS spectra of low pressure gas samples in a single-pass absorption cell.

The incoming mid-IR radiation can be directed in one of two directions using a mirror mounted on a translation stage. With the mirror removed from the beam path the radiation is coupled into a spectrum analyser (Bristol Instruments 721B-IR) to allow measurement of the properties of the laser comb. Alternatively, the beam can be intercepted and directed towards the gas cell to allow spectroscopy to be performed. In this case the beam is split into *reference* and *signal* channels using a pellicle beam splitter (Thorlabs BP145B4, spilt ratio 45:55). The signal beam is passed through a 80 cm stainless-steel absorption cell fitted with angled $CaF_2$ windows. Both beams are then focused with $CaF_2$ lenses (Thorlabs La5042-E, f=75 mm) onto thermo-electrically cooled HgCdTe photovoltaic detectors (Vigo Systems PVI-2TE-4), and the resultant

time-varying intensity signals recorded using a data acquisition system (Handyscope HS4).

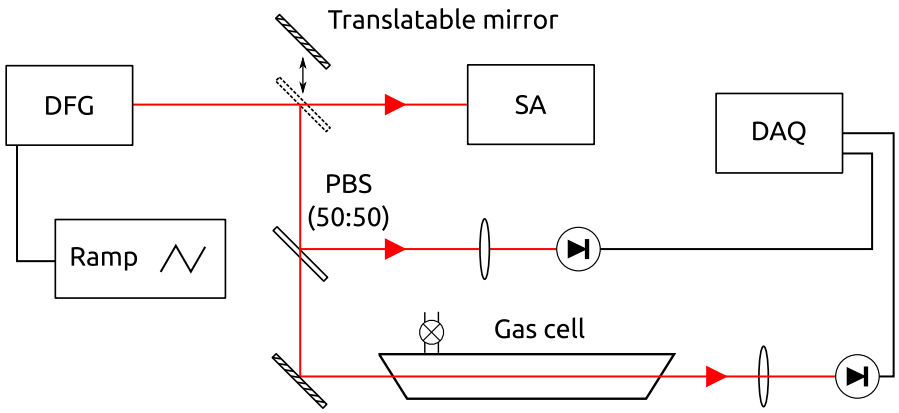


**Figure 6.10:** The experimental system used to perform mid-IR MUMAS spectroscopy. DFG represents the difference frequency generation system shown in Figure 6.5; SA, spectrum analyser; PBS, pellicle beam splitter (marked with split ratio); DAQ, data acquisition system. Further details are provided in text.

For the experiments described in this chapter transmission spectra were recorded at approximately 1 Hz as the laser modes were alternately scanned up and down in frequency. This scan was effected by scanning the cavity length of the Er/Yb laser in a similar manner as to that described in Chapter 5. A voltage ramp, generated by a function generator (Agilent 33500B), was amplified and applied to the intra-cavity piezo-electric transducer stack. The scanning of the near-IR laser comb is then transferred into the mid-IR by the DFG process.

### 6.5.2 Filling procedure

Gas samples for spectroscopy were mixed in the measurement cell. The composition of each sample – and the total pressure – was measured during the filling process with a capacitance manometer with a measurement range 0 — 132 mbar (Setra 730, quoted accuracy 0.25% down to a pressure of 0.025 mbar). Before carrying out measurements the

gas cell was flushed with nitrogen and evacuated with a rotary vacuum pump (Edwards E2M5) to a base pressure of $\sim$ 1 mbar. Due to difficulties in admitting small enough volumes of gas to the cell a larger amount of gas was added and then partially evacuated to achieve the desired pressure. Samples for the two different species were mixed in a slightly different manner due to the different strength of absorption lines.

To prepare samples for ammonia spectroscopy, an amount ($\sim$ 30 mbar) of ammonia was admitted to the gas cell then evacuated in a stepwise manner allowing spectra to be recorded at different pressures. To produce methane samples, $CH_4$ ($\sim$ 1 mbar) was first admitted to the gas cell and then diluted in nitrogen to a concentration of $\sim$ 2.5%. This mixture was then evacuated in a stepwise manner to produce the desired samples.

Owing to difficulties in obtaining cylinders of suitable methane and ammonia, samples were mixed from quantities held in low pressure tanks that had been filled from high-purity commercial cylinders.

### 6.5.3 Processing of data

For this work mid-IR MUMAS transmission spectra were recorded at $\sim$1 Hz as the ratio between signals from the signal and reference beams recorded on photovoltaic detectors. Approximately 60 spectra were recorded for each gas sample and it was desired to average a number of sequential spectra together in order to reduce the impact of noise and experimental fluctuations. Unfortunately, a small amount of unwanted jitter was detected in the scanning behaviour, leading to consecutive spectra displaying a small relative shift along the time scale. Therefore, in contrast to the method employed in Chapter 5, each individual transmission measurement was processed separately, before later being aligned to allow averaging.

The processing of spectra involved several steps. Each transmission spectrum was first projected onto a linear "frequency scanned" scale using information provided by a

Fabry-Perot etalon (as described in Section 5.2.3). A small proportion of spectra were found to contain a large amount of transient noise, thought to be caused by electronic effects, and these were detected and excluded from further analysis, leaving $\sim 55$ spectra for each sample. A Fourier low-pass frequency filter was then applied to the data to attenuate high frequency laser and detector noise.

Sets of spectra taken under each set of conditions were aligned to one another to mitigate the effects of jitter using a cross-correlation procedure. Stable baseline fluctuations, such as those caused by weak optical interference from stray beam path etalons, were removed from each spectrum by dividing the transmission signal by a signal representative of the transmission of the empty gas cell. This background transmission signal was determined by processing a set of spectra recorded from an empty gas cell, and then averaging the set and applying a smoothing filter to further attenuate noise. Finally, a section of each processed spectrum corresponding to a scan of one mode spacing was selected using knowledge of the laser mode spacing.

This procedure produced a set of $\sim 55$ processed, aligned, and background corrected spectra for each gas sample. The method by which these are averaged is discussed in Section 6.6.1.

### 6.5.4 Determination of comb parameters

Before data fitting could occur it was necessary to accurately determine the parameters describing the mid-IR laser comb. The nature of the DFG process ensures that the comb produced in the mid-IR closely represents the input near-IR comb (see Figure 6.9), thus allowing characterisation of the comb properties to occur at near-IR wavelengths. The properties of the Er/Yb multi-mode laser had been accurately determined for previous work (Section 5.3.1), and the values of mode spacing and mode linewidth remained unchanged. The properties of the envelope function describing the multi-mode comb

| Parameter | Value |
|---|---|
| $\Delta\nu_{space}$ | 18.38 GHz |
| $\Delta\nu_{width}$ | 8 MHz |
| $\nu_{centre}$ | 90069 GHz |
| $\Delta\nu_{env}$ | 103 GHz |
| $c$ | 0.11 |

**Table 6.1:** Values of the parameters describing the multi-mode laser used in this chapter.

had changed from previous work and so these had to be re-measured. Estimates were made using the Bristol Instruments spectrum analyser (by measuring a spectrum taken at 1.5 $\mu$m), and these optimised by fitting spectral data taken under known conditions (at 3.3 $\mu$m), in the same manner as described previously. The final comb parameters, used for fitting spectra presented in this chapter, are listed in Table 6.1.

## 6.6 Results and discussion

### 6.6.1 Ammonia measurements

Mid-IR MUMAS spectra were first recorded of ammonia. This molecule was chosen due to the presence of strong but widely separated absorption transitions in the wavelength region covered by the DFG source, which it was hoped would lead to a distinctive and not overly congested MUMAS spectrum. MUMAS spectra were recorded from a series of samples of pure ammonia at differing pressures. For each gas sample MUMAS spectra were recorded and individually processed as described in Section 6.5.3, resulting in approximately 55 spectra for each sample.

The processed experimental spectra contain random noise and baseline fluctuations, thought to be the result of laser and detector noise, and laser mode fluctuations. Therefore, to allow a good fit between this experimental data and the MUMAS model it was

beneficial to average a number of sequential spectra together. One approach to do this is to average all spectra recorded for a sample. Figure 6.11 shows a experimental spectrum of 7.17 mbar of ammonia treated in such a manner, and then fitted with the MUMAS model by allowing the partial pressure of ammonia to vary. Therefore this measurement represents an integration time of approximately one minute.

This spectrum is modelled using spectral information from the HITRAN database. The modelled MUMAS spectrum – shown in black – contains 4 main transitions, all from the third harmonic of the ammonia umbrella mode ($3\nu_2$). These transitions are of strength, $S \approx 10^{-23}$ cm$^{-1}$/(molecule $\times$ cm$^{-2}$). Additional underlying absorptions are also present from this and other vibrational bands. In total 10 transitions were included in the modelled spectrum. This results in a simple MUMAS spectrum with an obvious zero absorption level due to the sparsity of transitions, aiding the fitting process.

It can be seen that the modelled spectrum (in black) closely reproduces the experimental spectrum (red). Small discrepancies between the two traces are evident, particularly on the baseline, which may be the result of un-tabulated weak absorptions (arising from ammonia or a contaminating species) or uncorrected laser power fluctuations. However, as these absorption features are small and separated from the fitted features they are not expected to have a strong effect on the model fit. The sharp features observed around 2 GHz on the "Frequency scanned" scale, appear to be consistent across all spectra and are believed to be the result of a laser effect, possibly an unexpected mode fluctuation. These small discrepancies do not, however, prevent a good fit of the model to the data.

### Signal averaging

It was decided to average sequential spectra to reduce the effect of noise on the quality of the recorded spectra, and hence on concentration extracted from the modelled fit. Figure 6.12 shows 3 spectra, averaged over a different number of laser scans ($k$), illustrating

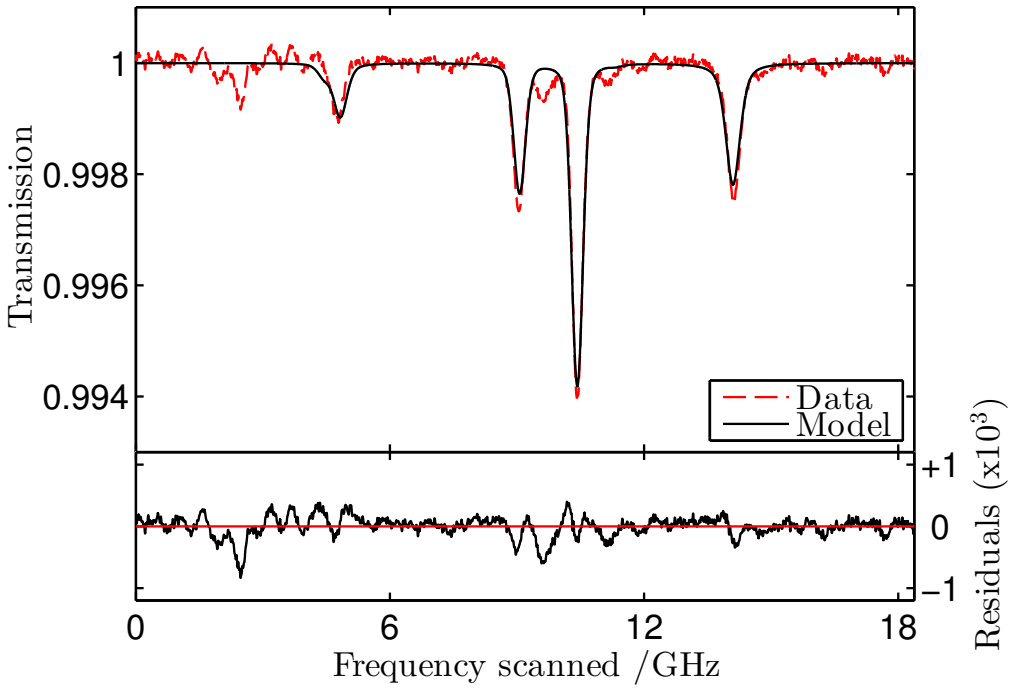


**Figure 6.11:** An example Mid-IR MUMAS spectrum of ammonia, in this case of a sample containing 7.17 mbar of ammonia.

the reduction in noise achieved by signal averaging.

The temporal resolution achievable with a measuring instrument is important to some applications, and therefore, it may not always be desirable to integrate over long time periods to reduce the uncertainty associated with a concentration measurement. In this situation the trade-off between taking more averages to improve spectral quality, and keeping the integration time to a minimum becomes important.

An analysis was performed in order to investigate this relationship for the experimental system used here. To do this, the processed spectra for a single gas sample were first grouped into sets of size $k$, and the spectra within a set averaged. These averaged spectra were then individually fitted with the MUMAS model, by allowing the partial pressure of $NH_3$ ($P_{NH_3}$) to vary using the non-linear least squares fitting algorithm described

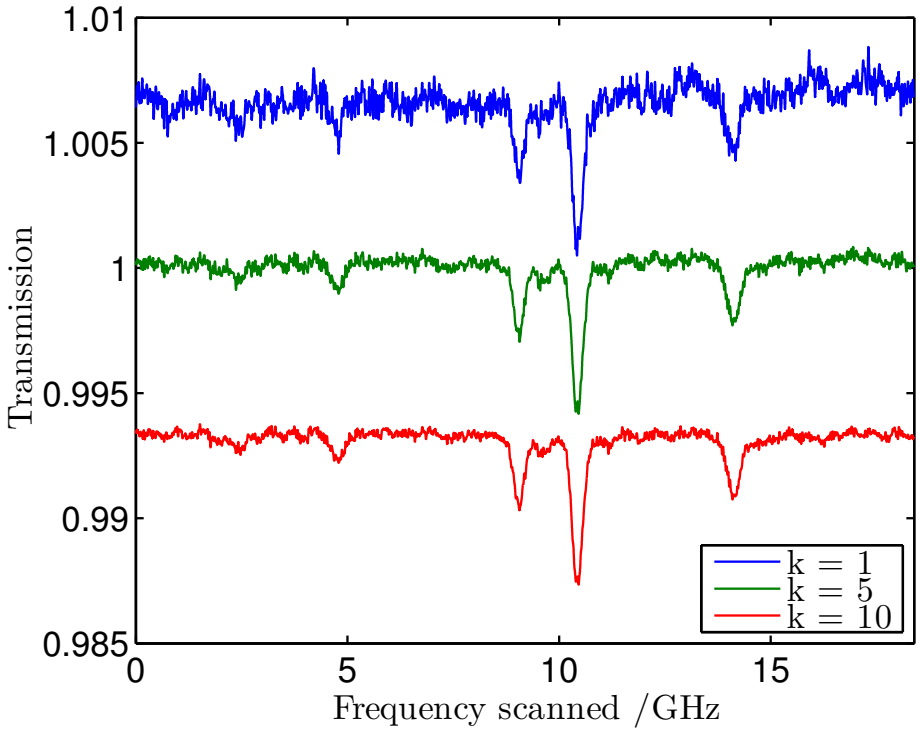


**Figure 6.12:** The effect of averaging on the spectra recorded with this DFG-MUMAS system. Spectra recorded from the same gas sample are shown, after being averaged over $k = 1$, 5, and 10 scans. The upper and lower traces have been offset for clarity.

in Section 5.3.2. The mean and standard deviation was then calculated for the best-fit values of $P_{NH_3}$ obtained from fitting the averaged spectra. This process was carried out for values of $k$ between 1 and 20.

Figure 6.13 displays the results of this analysis. It can be seen that the standard deviation of the set of partial pressure measurements reduces as the number of spectra averaged together ($k$) is increased. This reduction in measurement uncertainty occurs rapidly at first but delivers diminishing returns at large $k$. The same analysis was repeated for spectra recorded from 8 other gas samples, and in all cases a similar trend was observed. For these measurements an averaging span of 5 was chosen as presenting a good compromise between measurement time and measurement uncertainty.

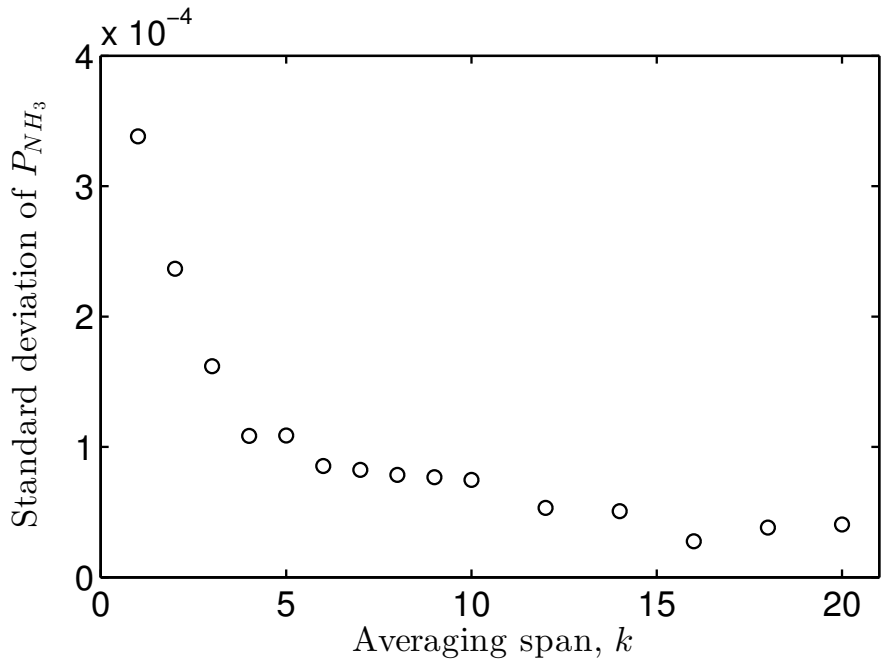


**Figure 6.13:** The variation in standard deviation with number of spectra averaged together. The observed trend is of a reduction in uncertainty with increasing values of the averaging span, $k$. The data shown here, obtained from measurements of a sample of 7.17 mbar $NH_3$ are typical for the other samples measured here.

Having chosen a value of the averaging span, $k$, it is possible to examine the variation of measurement uncertainty with partial pressure of ammonia using the coefficient of variance (the standard deviation of a set of measurements normalised by the mean value for that set). Figure 6.14 shows this for the 9 gas samples measured here. The observed trend is for a relatively constant uncertainty of around 3% for partial pressures greater than 5 mbar. Below this pressure the uncertainty rapidly increases to a value of 20% for the lowest pressure (1.00 mbar). The shape of the graph suggests that different noise sources may be dominant in these two regimes, and illustrates the challenging nature of making measurements at low partial pressure.

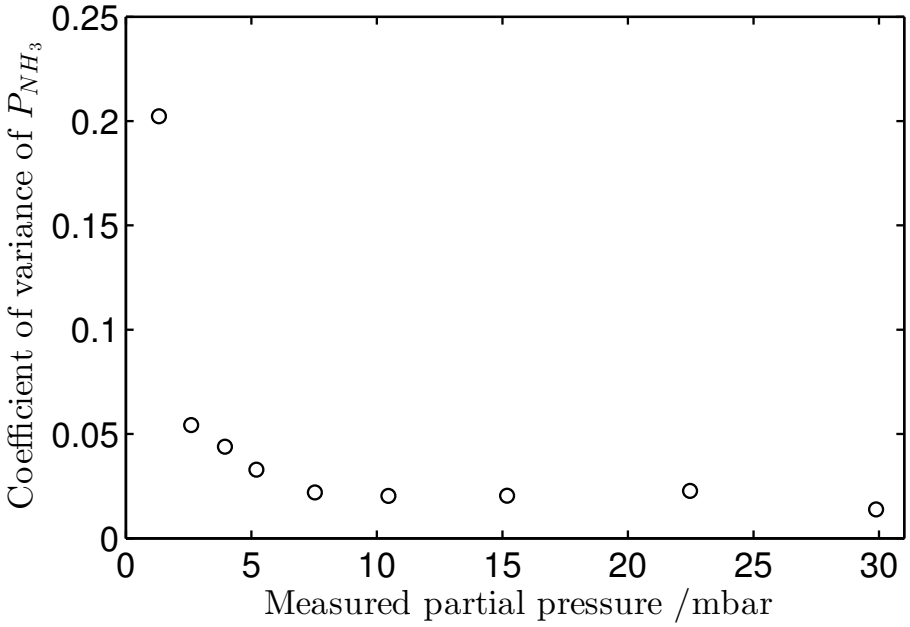


**Figure 6.14:** This coefficient of variance plot shows the variation in measurement uncertainty with measured partial pressure of $NH_3$. The data plotted here are for an averaging span, $k$, of 5.

### Quantitative detection

The ability of this MUMAS system to perform quantitative gas detection was assessed in a similar manner to that employed for the near-IR spectrometer in the previous chapter. The values of the partial pressure of ammonia determined through fitting the MUMAS spectra have been compared to those measured by a capacitance pressure gauge during the preparation of the sample. The values for the fitted partial pressure correspond to the mean of the fitted values of $P_{NH_3}$ for an averaging span of 5.

The results are plotted in Figure 6.15, from which it can be seen that these measurements closely follow a linear trend, indicating that the mid-IR MUMAS measurement provides a good measure of partial pressure. Error bars are displayed on each data point to provide a representation of the likely uncertainty associated with each measurement. The horizontal bars indicate the uncertainty in the partial pressure of ammonia present

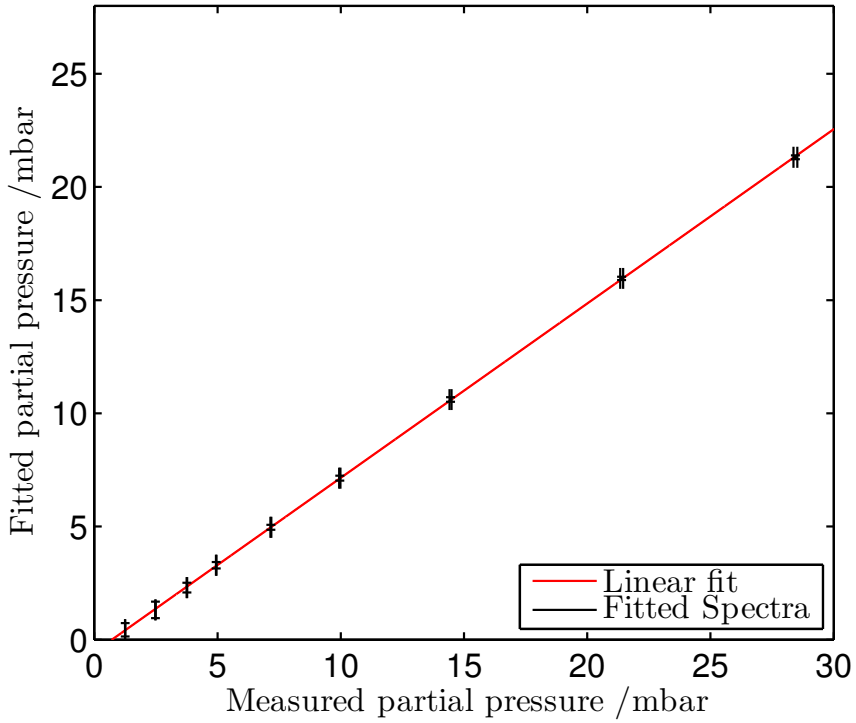


**Figure 6.15:** A comparison between the partial pressure of $NH_3$ as determined by MUMAS to that measured during the filling procedure with a capacitance pressure gauge. The fitted linear trend line is given by the equation $y = 0.77x - 0.55$.

in each sample. These sample composition uncertainties take into account the multiple measurements of pressure undertaken with the capacitance pressure gauge to prepare each sample using the procedure described in Section 6.5.2 (each with associated accuracy $\pm 0.25$ %). The vertical error bars correspond to an uncertainty range of $\pm\sigma$, the standard deviation of the set of fitted partial pressures.

The data points have been fitted with a linear trend, the gradient of which is 0.77. A gradient of unity was expected for this trend due to the absolute nature of the MUMAS modelling process. It is thought that this discrepancy may be the result of a leak in the ammonia vessel that allowed a small amount of air to enter during storage, diluting the gas. This would lead to there being less $NH_3$ in the cell than expected from pressure

measurements. Data taken on previous occasions, shortly after the ammonia container had been filled, showed less of a discrepancy.

In addition the fitted trend line intercepts the y-axis at a negative value (approximately $-0.53$ mbar). Further investigation has suggested that this may be the result of uncertainties in determining the true zero-absorption baseline for the spectra analysed here. In the spectral region analysed there are absorptions due to water transitions. The propagation pathlength of the signal beam in laboratory air was 22 cm longer than the reference beam, meaning that these absorptions do not contribute equally to both arms and thus do not completely cancel out. Consequently, broad $H_2O$ absorption lines underlie the ammonia absorptions analysed here and when combined with other loss effects such as scattering and absorption from the cell windows, and weak etalon fringes, the zero absorption baseline is difficult to determine.

To understand the impact of the water absorptions, a MUMAS spectrum is now examined before the application of the normal baseline correction (*i.e.* prior to division by an empty gas cell spectrum). Figure 6.16(a) shows an experimental spectrum recorded from a sample containing 2.32 mbar of ammonia. The modelled contributions of water (at atmospheric pressure, over a pathlength of 22 cm) and ammonia (for the sample conditions) to this MUMAS spectrum are shown in Figure 6.16(b). The partial pressure of water was determined as 25 mbar through a fit to the spectrum of the empty cell, which corresponds to a relative humidity of $\sim 78\%$ – within the expected range for the day the measurements were taken. The combination of these modelled components are shown in Figure 6.16(a) overlying the experimental data. It should be noted that the absolute transmission scale of the experimental data is not known without applying the normal baseline correction. Therefore, the data shown in this figure has been shifted vertically to best overlie the combined model spectrum. The residual between the data and combined model is plotted in Figure 6.16(c).

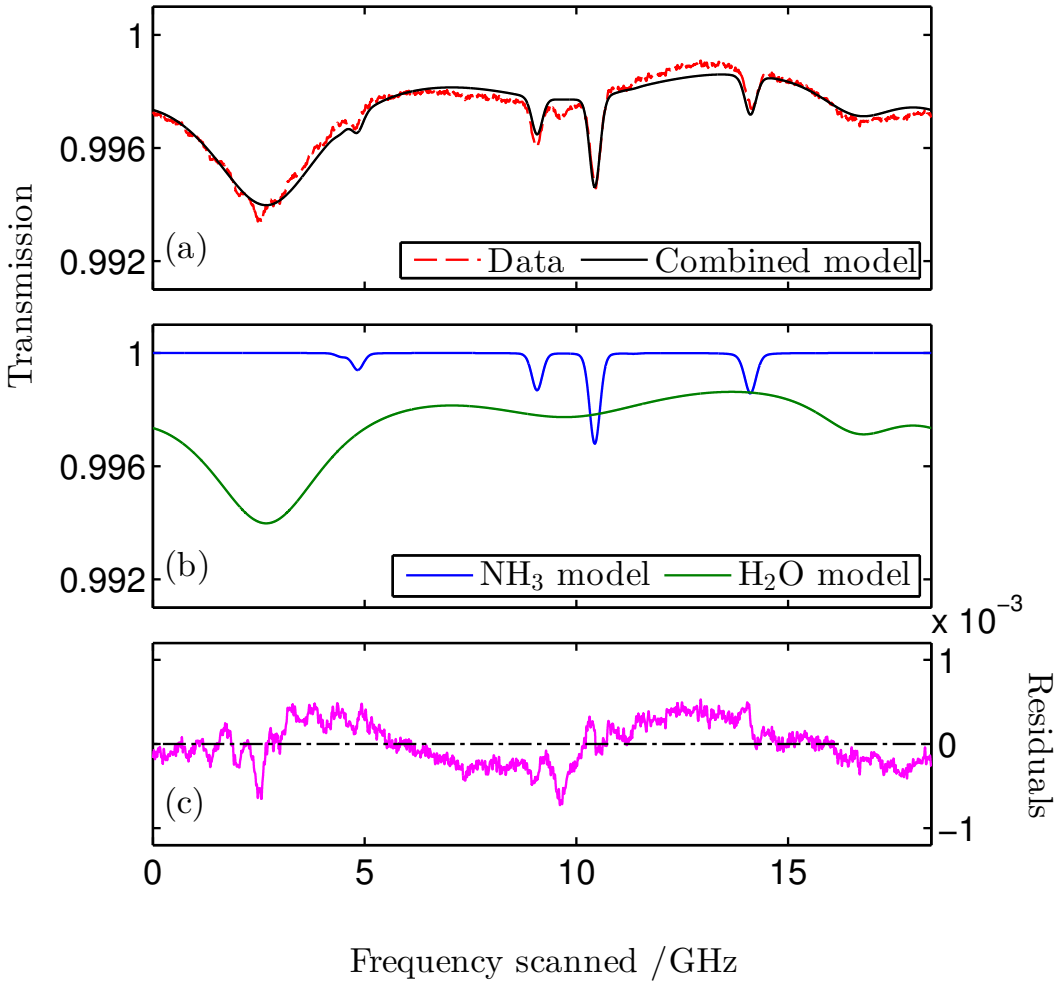


**Figure 6.16:** To investigate baseline offset effects, experimental data is shown prior to the normal baseline correction. **(a)** A spectrum recorded from a sample containing 2.32 mbar of $NH_3$ is shown overlying a modelled spectrum. The simulation accounts for absorption due to low pressure ammonia and atmospheric pressure water vapour. **(b)** The water and ammonia components of the modelled spectrum. **(c)** The residual between the modelled and experimental spectra shown in the top panel. For more details see the main text.

This figure illustrates that while the majority of the large baseline offset present in this data is caused by water absorptions, this cannot completely account for the shape of the baseline. The remaining effect has an oscillatory form and it therefore appears to be the result of etalon interferences in the signal beam path, possibly resulting from the cell windows. Overall, the baseline position and shape is expected to result from a combination of these interference and atmospheric absorption effects. It is suggested that the negative y-intercept observed in Figure 6.15 may be the result of a small variation in either of these contributions during the experiment, the relative magnitude of which are currently not quantified.

In general, baseline determination is a difficulty commonly encountered in absorption spectroscopy. Spectrometers aiming for quantitative detection often perform baseline correction at frequent intervals using a non-absorbing gas referred to as "zero air" (for example [137]). This system would benefit from such a method, and recording the baseline absorption at similar pressure to that of the ammonia samples would reduce the impact of etalon oscillations. This could be carried out with a sample of"zero-air" or a similar non-absorbing gas, and should be repeated on a regular basis (*i.e.* between each spectrum). In the case of spectra that contain widely spaced absorption features, separated by non-absorbing regions it may be possible to gain the same benefits by analytically fitting a baseline to regions free of absorptions.

### 6.6.2 Methane measurements

Mid-IR MUMAS spectra were also recorded of methane. In contrast to the ammonia spectrum, the methane spectrum contains many densely packed transitions arising from a large number of different overlapping vibrational bands. In the spectral window probed by this multi-mode source there are in excess of 3000 transitions listed in the HITRAN database.

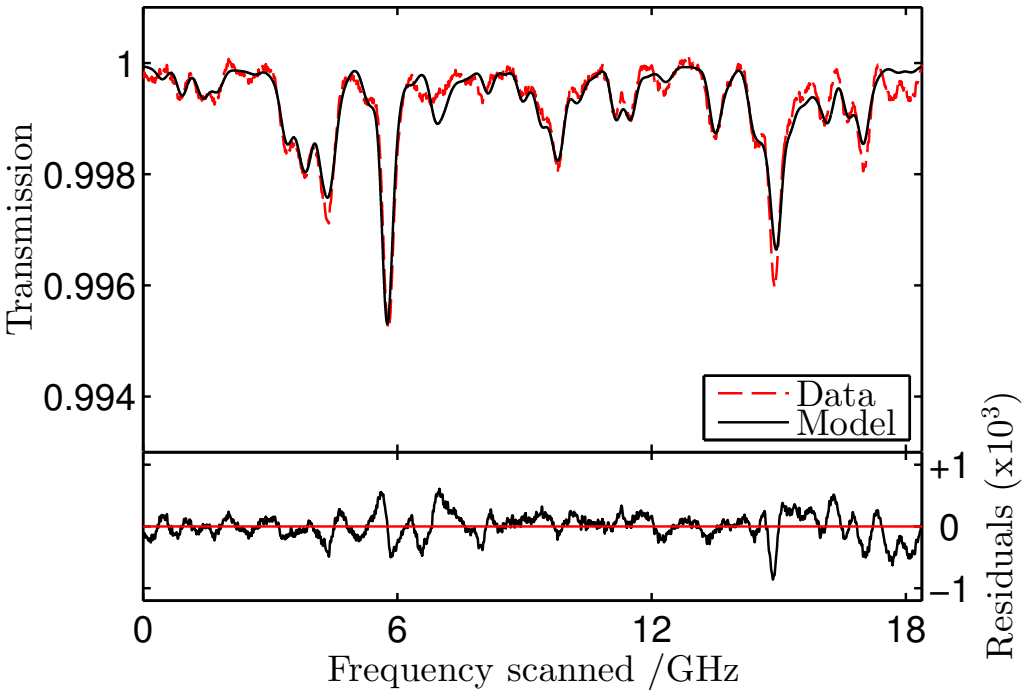


**Figure 6.17:** An example MUMAS spectrum of methane (average of ∼ 55 laser scans) measured for a sample containing 0.128 mbar of $CH_4$ diluted in $N_2$ to a total pressure of 3.99 mbar (shown in red). A fitted modelled spectrum is plotted as a solid black line.

The mid-IR MUMAS spectrum of $CH_4$ – an example of which is shown as a red dashed line in Figure 6.17 – is consequently complex and contains many overlapping absorption features. Overlying this is shown the fitted modelled spectrum (plotted as a black solid line), which was generated by considering the interaction between the laser comb and the strongest ∼450 methane transitions*. The absorption lines contributing the strongest absorption features to the MUMAS spectrum arise from transitions of the Q branch of the $\nu_3$ fundamental (a triply degenerate stretch) of both $^{12}CH_4$ and $^{13}CH_4$, and were of strength $S \approx 10^{-21}$ cm$^{-1}$/(molecule × cm$^{-2}$).

Despite the large number of methane transitions found in this spectral region, and thus

*These lines were selected by removing those with line strength less than $\frac{1}{1000}^{\text{th}}$ the strength of the strongest present in the modelling window.

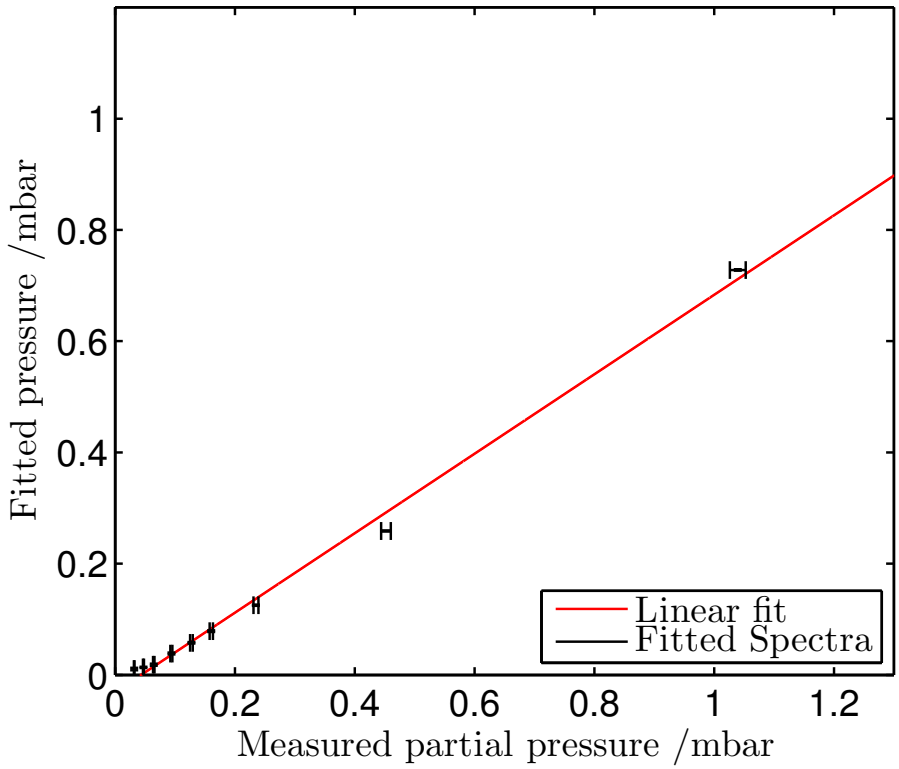


**Figure 6.18:** A comparison between the partial pressure of $CH_4$ as determined by MUMAS and that measured during the filling procedure with a capacitance pressure gauge. The fitted linear trend line is given by the equation $y = 0.71x - 0.031$.

the complexity of the modelling process, the model shows a good fit to the experimental spectrum. Again, small deviations occur between the modelled and experimental data, observed particularly as differences in peak and base line transmission.

Following the same method presented in Section 6.6.1 for ammonia, an averaging span of $k = 5$ was again chosen as presenting the best averaging span for this dataset. Therefore, sets of spectra averaged over 5 laser scans were used to determine the ability of MUMAS to perform quantitative measurements of the partial pressure of methane ($P_{CH_4}$).

Figure 6.18 shows the partial pressure of methane – as determined from the fit to the

MUMAS data – compared to the values measured using a capacitance pressure gauge during the filling process. The horizontal error bars in this figure correspond to the uncertainty in sample composition (again calculated through consideration of the filling procedure) and the vertical error bars to the uncertainty in fitted partial pressure, with the range indicated corresponding to $\pm\sigma$, the standard deviation of the set of fitted partial pressures.

The data points in this figure lie near to a fitted linear trend. In common with the ammonia data, however, this trend line has a gradient less than unity and a non-zero y-intercept. Again in this case the vertical offset of the fitted trend is thought to arise from difficulties in determining the zero-absorption baseline of the spectra. The scatter about the linear trend, indicative of reduced measurement accuracy, is also thought to be caused by this effect, and reflects the greater difficulties in determining the zero-absorption level for these spectra compared to ammonia due to the larger number of transitions present. The small vertical uncertainty range associated with each point in this dataset is thought to be a result of the large number of absorption features present in the spectrum, which allows a precise fit to be obtained despite the presence of random noise.

The low gradient of the fitted trend is again thought to reflect the purity of the gas used for measurements. The methane used for sample preparation was stored in low pressure reservoirs prior to sample generation, in a similar manner to the ammonia used in the previous section. In order to avoid these problems in future, more controlled gas reservoirs will be employed.

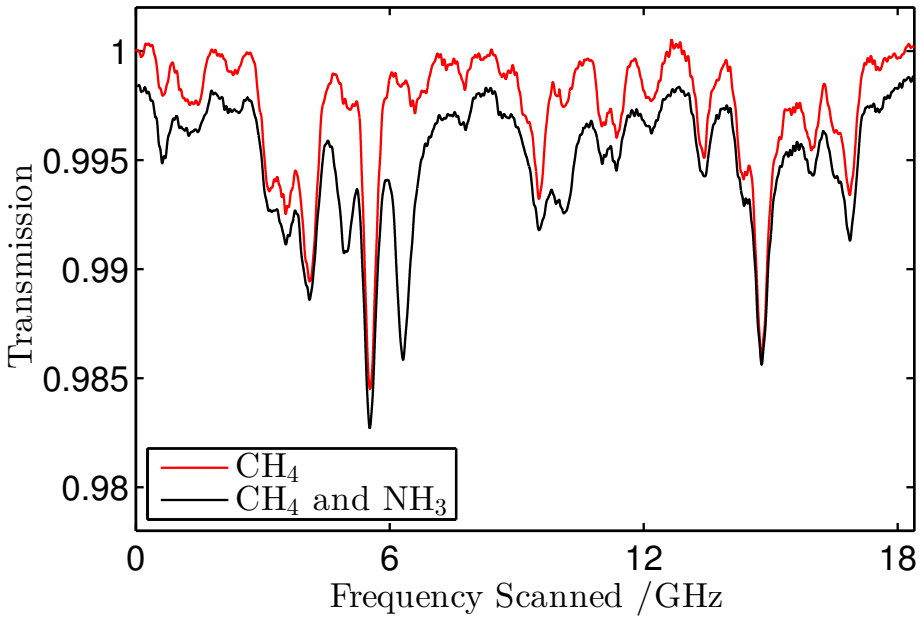


**Figure 6.19:** An example mid-IR multi-species MUMAS spectrum. The spectrum shown in red was recorded from a sample containing 0.72 mbar of methane (diluted in nitrogen). Shown in black is the spectrum from from this same sample after the addition of 27.4 mbar of ammonia.

### 6.6.3 Multi-species detection

The capability of this DFG-MUMAS system for multi-species detection was also confirmed. Figure 6.19 shows a spectrum recorded from a sample containing 0.72 mbar of methane (diluted in nitrogen), and also that from this same sample after the addition of 27.4 mbar of ammonia. As expected, the spectrum recorded by this MUMAS system shows absorption features arising from transitions in both species. In this case the strongest ammonia transitions occur away from the strong methane transitions, aiding clarity. Given the scope of this project – to check the feasibility of performing MUMAS at mid-IR wavelengths, further analysis was not performed.

## 6.7 Conclusions

Previous demonstrations of MUMAS have taken place in the visible and near-IR spectral regions. This chapter has reported the first application of MUMAS to gas detection in the mid-infrared region. This work was carried out to test the feasibility of sensitive gas sensing using MUMAS at these wavelengths, thus preparing the ground for future mid-IR gas sensing with non-linear sources or quantum well devices. In this work proof-of-principle spectra were measured of two molecular species.

The chapter started by considering the options for producing mid-infrared radiation. The chosen system used quasi-phase-matched difference frequency generation to transfer the well characterised multi-mode output of the previously developed Er/Yb laser to longer wavelengths. The theory behind DFG and experimental considerations for efficient radiation production have been discussed.

The design of the QPM-DFG system was reported. This required careful consideration for the properties needed to produce a suitable mid-IR laser comb. The performance of this system was then characterised and compared to theoretical predictions. The system was found to transfer an input comb to the mid-IR while maintaining the spectral properties of that comb. In particular, over a bandwidth $\sim 160$ GHz – the total width of the Er/Yb laser comb – the relative conversion efficiency was found to vary by less that 6%, thus maintaining the properties of the comb.

An experimental spectrometer was constructed to perform spectroscopy around 3.3 $\mu$m using the multi-mode radiation produced by this source. MUMAS spectra were recorded of samples containing ammonia and methane, both individually and together as components in a mixture. Analysis of these spectra determined that MUMAS can be used at mid-IR wavelengths for quantitative gas sensing.

# Chapter 7

# Future work

## 7.1 Overview

This chapter discusses the future direction of the MUMAS project. Two key areas are identified as being important for the application of MUMAS to gas sensing, and the potential for development in each considered.

## 7.2 Sensitivity

The sensitivity achievable with a spectrometer or other optical sensor is a key metric of that system. For a given application a gas sensor needs to detect the species of interest over a particular range of compositions. Trace gas analysis, such as that required to detect low concentration pollutants in the atmosphere or to perform medical diagnostics by means of breath analysis directly requires high sensitivity measurements. In other situations, where higher concentration species are being detected, a high sensitivity technique allows for a short measurement pathlength to be used. This has the benefit of making for a compact gas sensor but also of reducing the complexity of the system through swapping the multi-pass gas cells often used with near-IR diode lasers for short

pathlength, *in-situ* measurements.

The development of a QPM-DFG mid-IR multi-mode source described in the last chapter was motivated by a desire to achieve greater sensitivity by probing the stronger fundamental vibrational transitions found at these longer wavelengths. To determine whether the future direction of the MUMAS project should involve further investigation of mid-infrared sources it is useful to ascertain whether the move to mid-infrared wavelengths provided a useful improvement to the sensitivity of the technique. While the mid-IR system probed stronger transitions ($S \approx 10^{-21}$ cm$^{-1}$/(molecule $\times$ cm$^{-2}$) for $CH_4$) than the near-IR system ($S \approx 10^{-23}$ cm$^{-1}$/(molecule $\times$ cm$^{-2}$) for CO) it was unclear whether this would translate into a large improvement in sensitivity due to the larger scope for noise in the complex and low power DFG multi-mode source. Therefore, a quantitative estimate of the minimum detection limit was made for each system to allow comparison.

To obtain this estimate, the signal to noise ratio (S/N) was calculated for each member of two sets of spectra. The first set of spectra is shown in Figure 5.10 and consists of five spectra recorded with the the near-IR spectrometer described in Chapter 5. These measurements were made with samples containing varying partial pressures of CO (0.193 — 5.18 mbar) with a fixed background pressure of $N_2O$, $C_2H_2$ and $N_2$. This dataset thus allowed estimation of the sensitivity of this system to detecting carbon monoxide, the species with the strongest transitions of the three examined here. The second set of spectra used is described in Section 6.6.2 and consists of nine spectra recorded with the mid-IR spectrometer described in Chapter 6. These spectra were recorded of samples of methane diluted in nitrogen, with $CH_4$ partial pressures in the range 0.032 — 1.04 mbar. Methane was chosen for this comparison as it provided the strongest transitions in this region. All the spectra used were the result of averaging 20 laser scans.

In both cases a value for the S/N was calculated for each spectrum. To do this the peak absorption value for the strongest absorption feature present was measured and

used to quantify the signal. It is conventional to obtain a noise estimate for spectroscopic measurements such as these by taking the standard deviation of the noisy signal observed in absorption-free regions of the spectra [138]. This was not possible in this case as the congested nature of the methane spectra resulted in there being almost no regions free of absorption. Therefore, in the case of both sets of spectra the noise estimate was obtained by taking the standard deviation of data recorded in an empty gas cell. This trace was recorded after all other measurements had been taken, and was corrected for baseline drifts in the same manner as the spectra – by ratioing with a different empty cell trace (recorded at the beginning of the experiment). It is suggested that in both MUMAS systems baseline drifts provide a significant contribution to the effects that degrade the S/N and this method allows the effect of these slow changes to be included in the analysis.

Figures 7.1 and 7.2 show the results of this analysis for CO and $CH_4$ respectively. In both cases the estimation of S/N shows a good linear trend with partial pressure of absorber, the gradient of which describes the sensitivity of these systems. Both trend lines also show a small vertical offset from the origin – a deviation from the expected behaviour. It is believed that this offset is the result of uncertainty in determining the true zero-absorption level. Therefore, solely the gradient was used for the comparison.

The minimum detection limit of these systems was defined as the partial pressure of absorber resulting in a S/N value of unity. By using the gradient of the trend lines shown in Figures 7.1 and 7.2 this was determined to be 0.080 mbar for the near-IR system and 5.4 $\mu$bar for the mid-IR system. When normalised for the differing pathlengths – 16 m in a White cell for CO, and 0.8 m in a single-pass cell for $CH_4$ – the values obtained were 1.3 mbar $m^{-1}$ and 4.3 $\mu$bar $m^{-1}$ respectively. This gives a sensitivity for the mid-IR measurement of $\sim$300 times greater than the near-IR measurement. In fact, this improvement is approximately 3 times greater than would be expected from the increase in transition strength alone. It is believed that the additional improvements

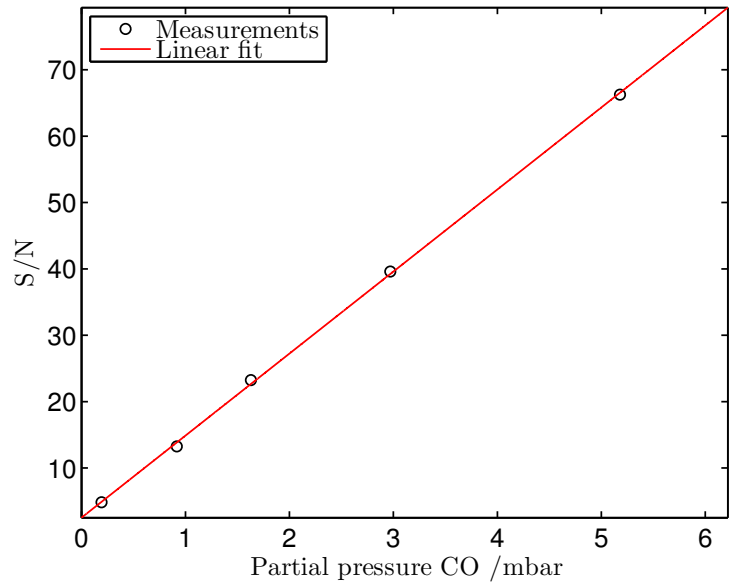


**Figure 7.1:** To estimate the sensitivity of near-IR MUMAS the signal to noise ratio (S/N) was calculated for spectra recorded of samples containing a range of partial pressures of carbon monoxide. The fitted linear trend line is given by the equation $y = 12.4x + 2.50$.

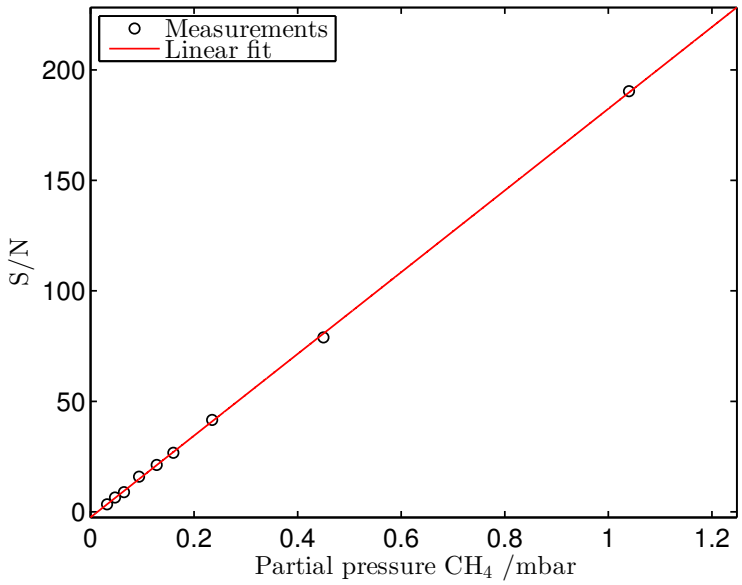


**Figure 7.2:** To estimate the sensitivity of mid-IR MUMAS the signal to noise ratio (S/N) was calculated for spectra recorded of samples containing a range of partial pressures of methane. The fitted linear trend line is given by the equation $y = 185x - 2.55$.

in the signal to noise ratio are the result of the attention paid to noise reduction in the DFG-MUMAS system and the slightly reduced bandwidth of the comb used in this system.

The sensitivity improvement obtained here by shifting the multi-mode comb to these longer wavelengths clearly demonstrates the potential for mid-IR MUMAS. Therefore, it is suggested that future development work should focus in this region, and should involve both incremental improvements to the DFG-MUMAS system and the testing of novel laser sources for use with MUMAS.

Several improvements could be made to the DFG system. Firstly, modifications to the Er/Yb laser, leading to improvements in tunability would result in large increases in the applicability of this DFG-MUMAS spectrometer by allowing wider choice in the spectral region probed. In the case of methane this would achieve large sensitivity improvements over the results shown here as much stronger transitions are positioned a short spectral distance away. Shifting the central wavelength of the mid-IR comb to shorter wavelengths by $\sim 10$ nm – which would require tuning the Er/Yb laser to longer wavelengths by less than 2.5 nm – would lead to interaction with transitions approximately 100 times stronger ($S = 10^{-19}$ cm$^{-1}$/(molecule $\times$ cm$^{-2}$)) than those probed here, achieving a proportional sensitivity improvement. Secondly, improvements to the non-linear mixing system could further improve the sensitivity of this experimental spectrometer. In particular, increasing the output power would reduce the impact of detector noise on the spectra. This could be achieved either through improving the conversion efficiency of the frequency generation process or by increasing the power contained in the incident beams. Taken together these changes would result in a flexible mid-IR multi-mode source with the potential for high sensitivity detection.

It is also suggested that there is great scope for the use of quantum well lasers as radiation sources for MUMAS. Fabry-Perot quantum cascade lasers (QCLs) and interband

cascade lasers (ICLs) optimised for multi-mode operation typically produce a broad spectral output covering tens or hundreds of nanometers. Such a device coupled with a narrow-bandpass interference filter has the potential to be a high power, widely tunable and extremely compact multi-mode source. These devices have the additional benefit of responding to high modulation frequencies, allowing the use of sensitivity enhancement techniques such as WMS to further lower the detection limit of the measurement. Inter-band cascade lasers similar to those described in [120] are currently under investigation for use with MUMAS.

## 7.3 Extension to atmospheric pressure

The MUMAS measurements reported in this thesis have been confined to low pressures samples. This restriction has been imposed by the need to limit the merging of spectral lines in the MUMAS spectra which would make these features less easily distinguishable. While there are some applications for gas sensing at reduced pressures, for example in low-pressure plasma reactors [119], there are far more applications that require atmospheric pressure sensing. In some situations this requirement can be side-stepped through the use of extractive sampling and measurement at reduced pressure, however, this greatly increases the complexity of the sensor. In other situations, where a rapid time-response is required or where the composition of the sample may be affected by sampling, this is not possible. In particular, a gas sensor that combines the ability to record spectra at atmospheric pressure, with high sensitivity, and thus allows detection to be performed over a short, atmospheric beam path is highly attractive. For these reasons it is desirable to attempt to extend the MUMAS measurements reported here to atmospheric pressures.

Atmospheric pressure MUMAS has previously been achieved by detecting widely spaced electronic oxygen transitions around 760 nm with a diode laser with 50 GHz

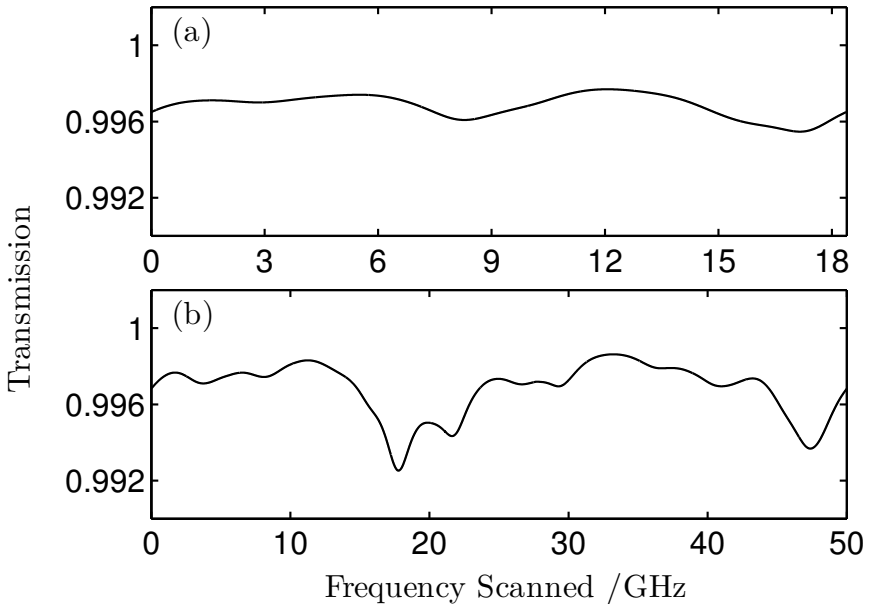


**Figure 7.3:** An illustration of the effect of mode spacing on the form of atmospheric pressure MUMAS spectra. Both plots show a modelled MUMAS spectrum of 0.25 mbar of methane buffered to atmospheric pressure with air. **(a)** shows the spectrum as modelled for a source with the properties of the DFG system used in Chapter 6. **(b)** shows the spectrum for the same source but with the mode spacing changed to 50 GHz.

mode spacing [6]. The mode spacing of a MUMAS system has a strong impact on the maximum total pressure at which spectra can be recorded: narrow mode spacings lead to wide and overlapping spectral features in the manner described in Section 3.4. The mode spacing of the Er/Yb laser used for the measurements reported here was restricted to less than 20 GHz by design limitations.

Figure 7.3 illustrates the effect of mode spacing on atmospheric pressure MUMAS spectra. In Figure 7.3(a) a modelled spectrum is shown that represents a measurement of methane, recorded at atmospheric pressure with the DFG system described in the previous chapter – it can be seen that all absorption features have been merged together. If a MUMAS spectrum is recorded of the same sample with the same radiation source but with the mode spacing of the laser comb increased from 18.39 GHz to 50 GHz far less blurring of spectral features occurs, as can be seen in Figure 7.3(b). In this case

a characteristic spectrum is produced, in which absorptions resulting from groups of spectral lines can be observed. This simple comparison illustrates the importance of multi-mode sources with larger mode spacings for atmospheric pressure MUMAS. The density of spectral lines probed also has an impact on the quality of MUMAS spectra. In general, additional gains in this area can be achieved with a widely tuneable laser through the choice of less congested spectral regions.

It is therefore suggested development work should be directed to producing multi-mode sources with wider mode spacings, thus allowing gas sensing at atmospheric pressures. Slightly wider mode spacing could be produced with the Er/Yb laser through design changes – and mode spacings of up to 33 GHz have already been realised, as shown in Figure 4.12 – however, physical limitations on cavity length would ultimately limit this value to $\sim 50$ GHz. Fabry-Perot semiconductor lasers such as ICLs have a monolithic construction and would be able to exceed this limit. When coupled with interference filters these devices would have the additional benefit of wide tunability allowing the targeting of sparse spectral regions.

## 7.4 Summary

This chapter has discussed two areas in which to focus future MUMAS research. The sensitivity of the measurements reported in this thesis has been discussed, and the benefits of performing spectroscopy at mid-infrared wavelengths have been assessed. From this analysis it is suggested that future work should focus on performing MUMAS at these longer wavelengths. The ability of MUMAS to perform atmospheric pressure measurements – an important property for deployed gas sensors – has also been explored. It has been seen that multi-mode sources with wider mode spacing would be necessary to achieve this outcome. Such devices thus present an additional development target.

# Chapter 8

# Conclusions

This thesis has reported work on a recently developed form of absorption spectroscopy – multi-mode absorption spectroscopy – that has the potential to be a useful addition to the array of optical gas sensing techniques currently in use. This thesis has described three main achievements: the development of a simple, robust and high performance multi-mode source for use with MUMAS, the first demonstration of multi-species detection using MUMAS, and the first extension of the MUMAS technique to mid-IR wavelengths.

## 8.1 Laser development

A multi-mode laser has been developed, that provides a high quality radiation source for MUMAS. This system, based on erbium-ion doped phosphate glass is a development of an earlier design produced for MUMAS. This improved laser was used to provide the comb of laser modes used for all experiments reported in this thesis.

The extensive design and prototyping process undertaken to produce this laser has been discussed. This process started by identifying the key properties required of a multi-mode laser source optimised for use with MUMAS. Areas where the existing design

fell short of these were identified and development undertaken to improve the laser system. The stages of this process have been discussed in detail in terms of the improvements required, the theoretical aspects of the laser design determined these properties, and the changes that were made.

Ultimately, this development work was brought together into a single laser design that met or exceeded the initial specifications. The final laser produced a comb of $\sim 10$ modes covering a bandwidth of approximately 180 GHz. The mode linewidth was determined to be less than 10 MHz, approximately 100 times narrower than the previous design, and fine enough not to impact on the resolution of recorded spectra, even of low pressure gas samples. The laser comb was centred around 1565 nm allowing access to a region rich in molecular overtone and combination bands. It was possible to scan the laser modes over a frequency range corresponding to far more than one mode spacing, allowing MUMAS spectra to be recorded. Finally, the simple, robust design produced a comb that was temporally stable – both when static and scanned – and also provided the flexibility to produce devices with customised properties. This laser thus provides a high-quality multi-mode source for use with MUMAS.

## 8.2 Multi-species detection

Multi-species detection has been demonstrated with MUMAS for the first time. While MUMAS has previously been used to measure multiple absorption features arising from transitions in a single molecule, this work comes closer to illustrating the full potential of MUMAS for gas sensing. The ability to perform multi-species detection with a single laser and a simple detection scheme compares favourably with other gas sensing techniques.

An experimental spectrometer was constructed to acquire MUMAS traces at wavelengths around 1565 nm using the Er/Yb multimode laser described elsewhere in this

thesis. Before this could be applied to quantitative gas sensing the properties of the laser had to be accurately determined to allow modelling of experimental data. This was carried out through a combination of direct measurement and inference from recorded spectra and interferograms. In particular, a new method was developed to estimate the mode spacing of the laser – the most sensitive parameter in the model – through analysis of an interferogram produced with a Fabry-Perot etalon. New fitting software was also written to aid in the determination of laser properties and analysis of gas spectra.

Spectra were recorded of three molecular species – CO, $N_2O$ and $C_2H_2$ – both as pure samples and as components of a mixture. A modelled spectral fit was then used to determine sample composition. Multi-species detection was carried out by recording spectra of mixed samples of the three species. Analysis allowed not just simultaneous identification of these three species, but also quantitative analysis of the mixture composition through measurement of the concentrations of mixture components with an uncertainty better than 2%.

## 8.3 Mid-infrared MUMAS

MUMAS has been carried out at mid-infrared wavelengths for the first time. This work demonstrates the feasibility of mid-IR MUMAS, and thus opens the door to gas detection using the rich crop of strong spectral lines that occur in this region. Spectroscopy in the mid-IR will thus both allow access to transitions from a wide range of molecules and enhance the sensitivity of gas detection with MUMAS by targeting strong, fundamental vibrational transitions.

A quasi-phase matched difference frequency generation system was designed and constructed to transfer the multi-mode comb produced by the Er/Yb laser to longer wavelengths. This system mixed a set of laser modes centred at 1565 nm with the output

of a single-mode Nd:YAG laser operating at its fundamental wavelength of 1064 nm to produce a multi-mode laser comb at 3.33 $\mu$m. The system was found to faithfully transfer the spectral properties of the input comb to longer wavelengths with minimal distortion. In particular, over a bandwidth of $\sim$ 160 GHz – the total width of the Er/Yb laser comb used for this work – the relative conversion efficiency was found to vary by less than 6%.

An experimental spectrometer was constructed to allow proof-of-principle spectroscopic measurements. Mid-IR MUMAS spectra were recorded of ammonia and methane, both individually and together as components in a mixture. Analysis of these spectra determined that MUMAS can be used at mid-IR wavelengths for quantitative gas sensing. A minimum detection level for this system was determined to be 4.3 $\mu$bar m$^{-1}$ for $CH_4$, a sensitivity increase of 300 over similar measurements performed in the near-IR. This result indicates the potential for gas sensing with MUMAS in the mid-IR.

## 8.4 Overall conclusions

MUMAS provides a viable method for multi-transition measurement whilst using a single laser and a simple detection scheme. When applied to multi-species detection this allows simultaneous measurements of multiple mixture components to be made in a simple manner. The MUMAS technique thus presents a useful addition to the array of optical gas sensing techniques currently in use. In addition, when carried out with a suitable radiation source, MUMAS is able to use the strong fundamental vibrational transitions found at mid-infrared wavelengths to realise gains in sensitivity.

# Appendix A

# Acetylene line position measurements

This appendix describes a survey of the acetylene spectrum in the 1560 — 1570 nm region, carried out to provide transition data for fitting MUMAS spectra.

During the near-IR MUMAS work reported in Chapter 5 it was discovered that the tabulation of acetylene transitions around 1565 nm in the HITRAN database did not allow adequate modelling of recorded MUMAS spectra. Upon further investigation it was determined that the database was incomplete in this region.

To obtain reliable spectral information a survey of the line positions and strengths of $C_2H_2$ was carried out over a wide region spanning the area probed by MUMAS. An external cavity diode laser (Sacher Lion) was used to record 28 overlapping TDLAS spectra of a low-pressure sample of $C_2H_2$ in a White cell. The spectra were linearised in frequency using information from a Fabry-Perot etalon and each was then placed upon an absolute frequency scale using spectra recorded simultaneously from a sample of CO in a different, single-pass cell, as a wavelength reference.

The strongest observed absorption features in each spectrum were fitted with Voigt

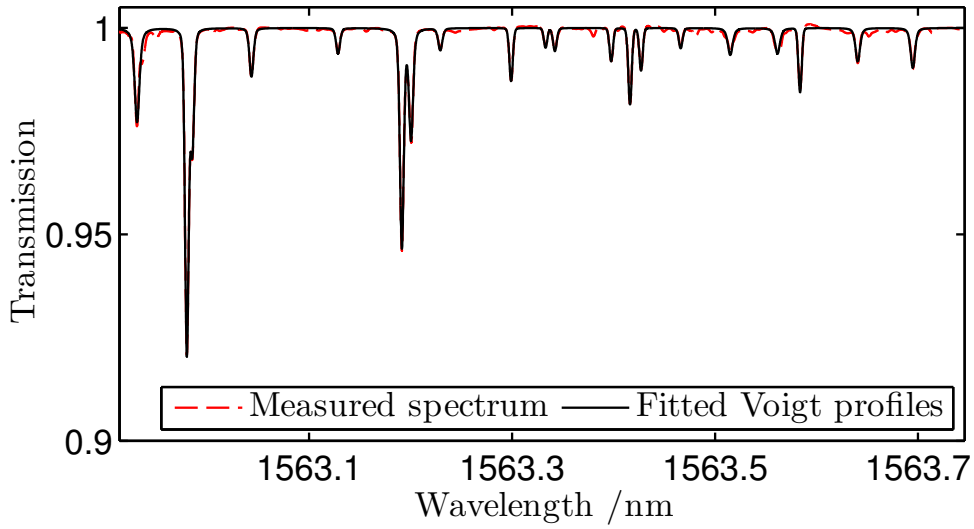


**Figure A.1:** An example single mode TDLAS spectrum recorded in this work (red, dashed). The solid black line represents the combined Voigt fits to the 20 strongest absorption features.

profiles to obtain an estimate of their central wavelength and line strength, Figure A.1 illustrates this for a single spectrum. The Gaussian component of these Voigt functions was set to the value calculated for Doppler broadening (using equation 2.8), allowing an estimate of the collisional self-broadening parameter to also be made. To allow the modelling of non-pure samples *i.e.* those containing $C_2H_2$ mixed with other gases, it was necessary to make an estimate of the collisional air-broadening parameter. This was done for each line by simply setting this value to one half of that estimated for the self-broadening parameter. This method is consistent with the transitions listed in the HITRAN database for acetylene in this region, for which this ratio falls between 0.50 and 0.57 in all cases.

In total, 265 spectral lines were identified, compared to 126 lines in the HITRAN database for the same region, although additional weaker lines were present in the measured spectra but not characterised. In general, the non-tabulated lines identified in

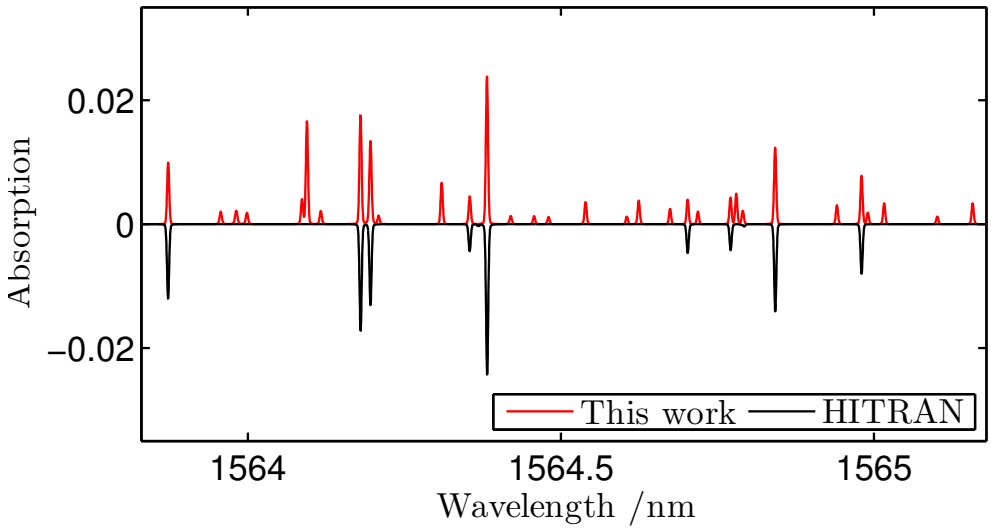


**Figure A.2:** An illustration of the additional transitions measured in this work. Modelled spectra of the region probed by the MUMAS comb for 5 mbar of $C_2H_2$ using the data compiled here and the HITRAN database. HITRAN data is plotted with negative absorption for clarity.

this survey were of relatively weak line strength, however, this was not entirely the case with some additional strong lines being discovered.

Figure A.2 shows modelled spectra for the region probed by the multi-mode laser used in Chapter 5. This plot shows additional transitions discovered in this survey, and thus illustrates the necessity of performing these measurements to provide a more complete set of transitions for the fitting of MUMAS spectra. Figure A.3 shows the wavelength and line strength of all the transitions identified in this survey with all transitions listed in the HITRAN database in the region for comparison.

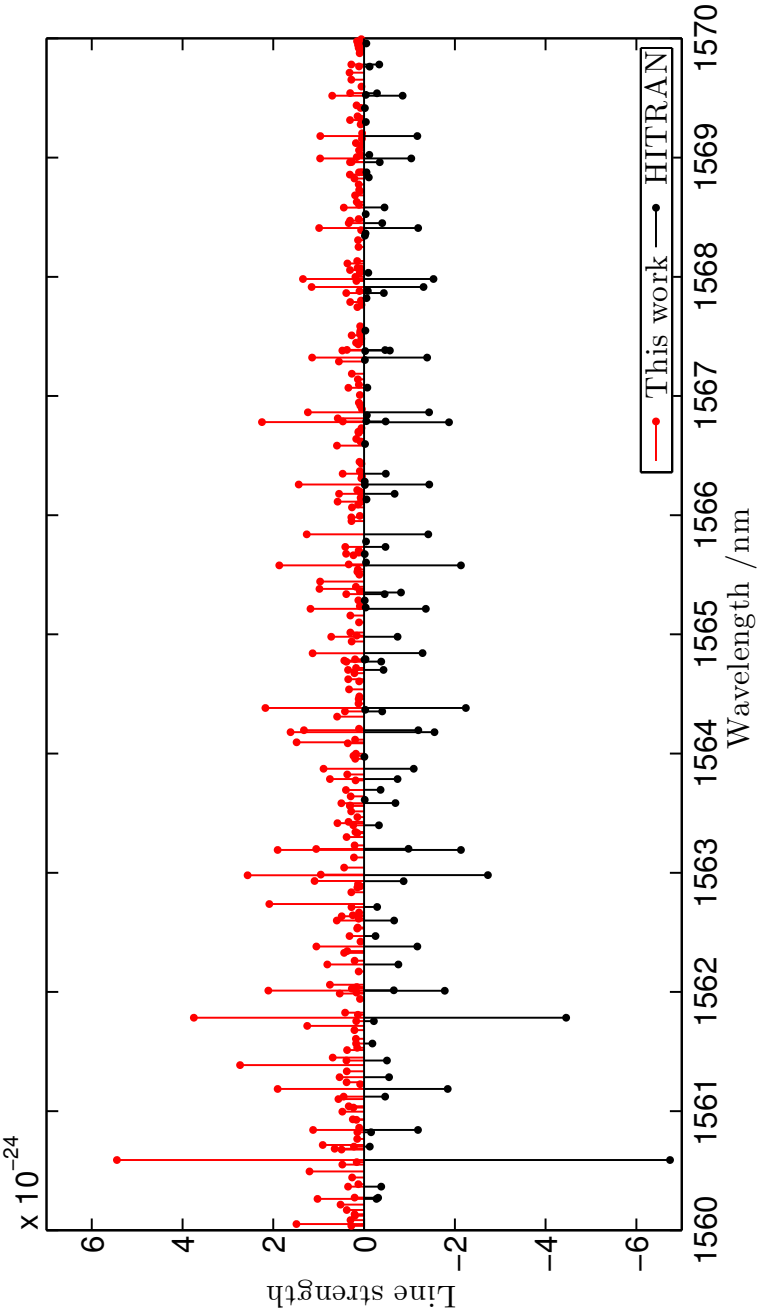


**Figure A.3:** The line strengths and line centres of all 265 transitions identified in these measurements. The transitions listed in the HITRAN database are also shown for comparison and plotted with negative line strengths for clarity.

# Bibliography


[1] S. Solomon, D. Qin and M. Manning. *Climate change 2007-the physical science basis: Working group I contribution to the fourth assessment report of the IPCC*. Vol. 4. Cambridge University Press, 2007.

[2] I Linnerud, P Kaspersen and T Jaeger. "Gas monitoring in the process industry using diode laser spectroscopy". *Applied Physics B: Lasers and Optics* 305 (1998), pp. 297–305.

[3] J. Hodgkinson and R. P. Tatam. "Optical gas sensing: a review". *Measurement Science and Technology* 24.1 (Jan. 2013), p. 012004. DOI: 10.1088/0957-0233/24/1/012004.

[4] F. Di Francesco, R. Fuoco, M. Trivella and A. Ceccarini. "Breath analysis: trends in techniques and clinical applications". *Microchemical Journal* 79.1-2 (Jan. 2005), pp. 405–410. DOI: 10.1016/j.microc.2004.10.008.

[5] P Werle. "A review of recent advances in semiconductor laser based gas monitors". *Spectrochimica Acta Part A: Molecular and Biomolecular Spectroscopy* 54.2 (Feb. 1998), pp. 197–236. DOI: 10.1016/S1386-1425(97)00227-8.

[6] Y Arita and P Ewart. "Multi-mode absorption spectroscopy". *Optics Communications* 281.9 (Jan. 2008), pp. 2561–2566. DOI: 10.1016/j.optcom.2007.12.096.

[7] Y. Arita, R. Stevens and P. Ewart. "Multi-mode absorption spectroscopy of oxygen for measurement of concentration, temperature and pressure". *Applied Physics B: Lasers and Optics* 90.2 (Jan. 2008), pp. 205–211. DOI: 10.1007/s00340-007-2917-y.

[8] Y. Arita and P. Ewart. "Infra-red multi-mode absorption spectroscopy of acetylene using an Er/Yb:glass micro-laser." *Optics express* 16.7 (Mar. 2008), pp. 4437–42.

[9] M. L. Hamilton, G. A. D. Ritchie, Y. Arita and P. Ewart. "Multi-mode absorption spectroscopy, MUMAS, using wavelength modulation and cavity enhancement techniques". *Applied Physics B* 100.3 (May 2010), pp. 665–673. DOI: 10.1007/s00340-010-4040-8.

[10] J. H. Northern, A. W. J. Thompson, M. L. Hamilton and P. Ewart. "Multi-species detection using multi-mode absorption spectroscopy (MUMAS)". *Applied Physics B* (Mar. 2013). DOI: 10.1007/s00340-013-5382-9.

[11] H. I. Schiff, G. I. Mackay and J Bechara. "The use of tunable diode laser absorption spectroscopy for atmospheric measurements". *Research on chemical intermediates* 20.3-5 (1994), pp. 525–556.

[12] R. P. Wayne. *Chemistry of atmospheres*. 2nd. Jan. 1993.

[13] H. Bovensmann, M. Buchwitz, J. P. Burrows, M. Reuter, T. Krings, K. Gerilowski, O. Schneising, J. Heymann, A. Tretner and J. Erzinger. "A remote sensing technique for global monitoring of power plant $CO_2$ emissions from space and related applications". *Atmospheric Measurement Techniques* 3.4 (July 2010), pp. 781–811. DOI: 10.5194/amt-3-781-2010.

[14] J. C. Atherton and R. C. Spiller. "The urea breath test for Helicobacter pylori." *Gut* 35.6 (June 1994), pp. 723–5.

[15] W. Cao and Y. Duan. "Current Status of Methods and Techniques for Breath Analysis". *Critical Reviews in Analytical Chemistry* 37.1 (Apr. 2007), pp. 3–13. DOI: 10.1080/10408340600976499.

[16] D. Smith and P. Spanel. "The challenge of breath analysis for clinical diagnosis and therapeutic monitoring." *The Analyst* 132.5 (May 2007), pp. 390–6. DOI: 10.1039/b700542n.

[17] B. Cummings, M. L. Hamilton, L. Ciaffoni, T. R. Pragnell, R. Peverall, G. a. D. Ritchie, G. Hancock and P. a. Robbins. "Laser-based absorption spectroscopy as a technique for rapid in-line analysis of respired gas concentrations of O2 and CO2." *Journal of applied physiology (Bethesda, Md. : 1985)* 111.1 (July 2011), pp. 303–7. DOI: 10.1152/japplphysiol.00119.2011.

[18] H. Teichert, T. Fernholz and V. Ebert. "Simultaneous in situ measurement of CO, $H_2O$, and gas temperatures in a full-sized coal-fired power plant by near-infrared diode lasers." *Applied optics* 42.12 (Apr. 2003), pp. 2043–51.

[19] K. Kohse-Höinghaus, R. S. Barlow, M. Aldén and J. Wolfrum. "Combustion at the focus: laser diagnostics and control". *Proceedings of the Combustion Institute* 30.1 (Jan. 2005), pp. 89–123. DOI: 10.1016/j.proci.2004.08.274.

[20] S. Wagner, B. T. Fisher, J. W. Fleming and V. Ebert. "TDLAS-based in situ measurement of absolute acetylene concentrations in laminar 2D diffusion flames". *Proceedings of the Combustion Institute* 32.1 (Jan. 2009), pp. 839–846. DOI: 10.1016/j.proci.2008.05.087.

[21] D. Brassington. "Tunable diode laser absorption spectroscopy for the measurement of atmospheric species". In: *Spectroscopy in Environmental Science*. Ed. by R. Clark and R. Hester. Vol. 24. John Wiley  Sons, 1995. Chap. 3, pp. 85–145.

[22] J. M. Hollas. *High resolution spectroscopy*. J. Wiley, 1998.

[23] W. Demtröder. *Laser spectroscopy.* 4th. Vol. 2. Springer, 2008.

[24] R. N. Hall, G. E. Fenner, J. D. Kingsley, T. J. Soltys and R. O. Carlson. "Coherent Light Emission From GaAs Junctions". *Phys. Rev. Lett.* 9.9 (Nov. 1962), pp. 366–368. DOI: 10.1103/PhysRevLett.9.366.

[25] M. G. Allen. "Diode laser absorption sensors for gas-dynamic and combustion flows." *Measurement science technology* 9.4 (Apr. 1998), pp. 545–62.

[26] K. Krzempek, R. Lewicki, L. Nähle, M. Fischer, J. Koeth, S. Belahsene, Y. Rouillard, L. Worschech and F. K. Tittel. "Continuous wave, distributed feedback diode laser based sensor for trace-gas detection of ethane". *Applied Physics B* 106.2 (Jan. 2012), pp. 251–255. DOI: 10.1007/s00340-011-4857-9.

[27] P. Werle, F. Slemr, K. Maurer, R. Kormann, R. Mücke and B. Jänker. "Near- and mid-infrared laser-optical sensors for gas analysis". *Optics and Lasers in Engineering* 37.2-3 (Feb. 2002), pp. 101–114. DOI: 10.1016/S0143-8166(01)00092-6.

[28] M. Mazurenka, A. J. Orr-Ewing, R. Peverall and G. A. D. Ritchie. "Cavity ring-down and cavity enhanced spectroscopy using diode lasers". *Annual Reports Section "C" (Physical Chemistry)* 101 (2005), p. 100. DOI: 10.1039/b408909j.

[29] P. A. Martin. "Near-infrared diode laser spectroscopy in chemical process and environmental air monitoring". *Chemical Society Reviews* 31.4 (June 2002), pp. 201–210. DOI: 10.1039/b003936p.

[30] Y. He, R. Kan, F. Englich, W. Liu and B. Orr. "Simultaneous multi-laser, multi-species trace-level sensing of gas mixtures by rapidly swept continuous-wave cavity-ringdown spectroscopy". *Optics Express* 18.19 (2010), pp. 20059–20071.

[31] R. K. Hanson. "Applications of quantitative laser sensors to kinetics, propulsion and practical energy systems". *Proceedings of the Combustion Institute* 33.1 (2011), pp. 1–40. DOI: 10.1016/j.proci.2010.09.007.

[32] Y. Gérard, R. Holdsworth and P. Martin. "Multispecies in situ monitoring of a static internal combustion engine by near-infrared diode laser sensors". *Applied optics* 46.19 (2007), pp. 3937–3945.

[33] N. Docquier and S. Candel. "Combustion control and sensors: a review". *Progress in Energy and Combustion Science* 28.2 (Jan. 2002), pp. 107–150. DOI: 10.1016/S0360-1285(01)00009-0.

[34] G. Gao, B. Chen and T. Cai. "Simultaneous detection of CO and $CO_2$ at elevated temperatures using tunable diode laser absorption spectroscopy near 1570 nm". *Optics and Spectroscopy* 114.3 (Mar. 2013), pp. 340–346. DOI: 10.1134/S0030400X13030120.

[35] B. L. Upschulte, D. M. Sonnenfroh and M. G. Allen. "Measurements of CO, $CO_2$, OH and $H_2O$ in room temperature and combustion gases using a broadly current-tuned multi-section InGaAsP diode laser". *Applied optics* 38.9 (1999), pp. 1506–1512.

[36] W. Miekisch, J. K. Schubert and G. F. E. Noeldge-Schomburg. "Diagnostic potential of breath analysis–focus on volatile organic compounds." *Clinica chimica acta; international journal of clinical chemistry* 347.1-2 (Sept. 2004), pp. 25–39. DOI: 10.1016/j.cccn.2004.04.023.

[37] M. Luong, R. Zhang, C. Schulz and V. Sick. "Toluene laser-induced fluorescence for in-cylinder temperature imaging in internal combustion engines". *Applied Physics B* 91.3-4 (Apr. 2008), pp. 669–675. DOI: 10.1007/s00340-008-2995-5.

[38] B. Williams, M. Edwards, R. Stone, J. Williams and P. Ewart. "High precision in-cylinder gas thermometry using Laser Induced Gratings: Quantitative measurement of evaporative cooling with gasoline/alcohol blends in a GDI optical engine". *Combustion and Flame* (Aug. 2013). DOI: 10.1016/j.combustflame.2013.07.018.

[39] T. Meyer, S. Roy, R. Lucht and J. Gord. "Dual-pump dual-broadband CARS for exhaust-gas temperature and $CO_2$ – $O_2$ – $N_2$ mole-fraction measurements in model gas-turbine combustors". *Combustion and Flame* 142.1-2 (July 2005), pp. 52–61. DOI: 10.1016/j.combustflame.2005.02.007.

[40] D. Baer, R. Hanson, M. Newfield and N Gopaul. "Multiplexed diode-laser sensor system for simultaneous $H_2O$, $O_2$, and temperature measurements". *Optics letters* 19.22 (1994), pp. 1900–1902.

[41] L. A. Kranendonk, R. Huber, J. G. Fujimoto and S. T. Sanders. "Wavelength-agile $H_2O$ absorption spectrometer for thermometry of general combustion gases". *Proceedings of the Combustion Institute* 31.1 (Jan. 2007), pp. 783–790. DOI: 10.1016/j.proci.2006.08.003.

[42] A. Arnold. "A simple extended-cavity diode laser". *Review of Scientific Instruments* 69 (1998), pp. 1236–1239.

[43] C. J. Hawthorn, K. P. Weber and R. E. Scholten. "Littrow configuration tunable external cavity diode laser with fixed direction output beam". *Review of Scientific Instruments* 72.12 (2001), p. 4477. DOI: 10.1063/1.1419217.

[44] S. E. Park, T. Y. Kwon, E.-J. Shin and H. S. Lee. "A compact extended-cavity diode laser with a littman configuration". *IEEE Transactions on Instrumentation and Measurement* 52.2 (Apr. 2003), pp. 280–283. DOI: 10.1109/TIM.2003.809912.

[45] Y. Arita. "Multi-mode Absorption Spectroscopy". DPhil Thesis. University of Oxford, 2008.

[46] S. Sanders, D. Mattison, J. Jeffries and R. K. Hanson. "Sensors for high-pressure, harsh combustion environments using wavelength-agile diode lasers". *Proceedings of the Combustion Institute* 29 (2002), pp. 2661–2667.

[47] D. B. Oh, M. E. Paige and D. S. Bomse. "Frequency Modulation Multiplexing for Simultaneous Detection of Multiple Gases by use of Wavelength Modulation Spectroscopy with Diode Lasers." *Applied optics* 37.12 (Apr. 1998), pp. 2499–501.

[48] A. Liu and X. Zhang. "A review of MEMS external-cavity tunable lasers". *Journal of Micromechanics and Microengineering* 17.1 (Jan. 2007), R1–R13. DOI: 10.1088/0960-1317/17/1/R01.

[49] M. Chacinski, M. Isaksson and R. Schatz. "High-speed direct Modulation of widely tunable MG-Y laser". *IEEE Photonics Technology Letters* 17.6 (June 2005), pp. 1157–1159. DOI: 10.1109/LPT.2005.846489.

[50] V. Jayaraman, Z.-M. Chuang and L. Coldren. "Theory, design, and performance of extended tuning range semiconductor lasers with sampled gratings". *IEEE Journal of Quantum Electronics* 29.6 (June 1993), pp. 1824–1834. DOI: 10.1109/3.234440.

[51] L. Ciaffoni, G. Hancock, P. L. Hurst, M. Kingston, C. E. Langley, R. Peverall, G. A. D. Ritchie and K. E. Whittaker. "Demonstration of a widely tunable digital supermode distributed Bragg reflector laser as a versatile source for near-infrared spectroscopy". *Applied Physics B* 110.2 (Jan. 2012), pp. 139–145. DOI: 10.1007/s00340-011-4869-5.

[52] *Li-cor Biosciences 2009 LI-7500A open path $CO_2/H_2O$ gas analyser.*

[53] W Denzer, M. L. Hamilton, G Hancock, M Islam, C. E. Langley, R Peverall and G. A. D. Ritchie. "Near-infrared broad-band cavity enhanced absorption spectroscopy using a superluminescent light emitting diode." *The Analyst* 134.11 (Nov. 2009), pp. 2220–3. DOI: 10.1039/b916807a.

[54] F. Xu, Z. Lv, Y. G. Zhang, G. Somesfalean and Z. G. Zhang. "Concentration evaluation method using broadband absorption spectroscopy for sulfur dioxide monitoring". *Applied Physics Letters* 88.23 (2006), p. 231109. DOI: 10.1063/1.2211299.

[55] C. Kaminski, R. Watt, A. Elder, J. Frank and J. Hult. "Supercontinuum radiation for applications in chemical sensing and microscopy". *Applied Physics B* 92.3 (Aug. 2008), pp. 367–378. DOI: 10.1007/s00340-008-3132-1.

[56] G Somesfalean, M Sj
"oholm, L Persson, H Gao, T Svensson and S Svanberg. "Temporal correlation scheme for spectroscopic gas analysis using multimode diode lasers". *Applied Physics Letters* 86 (2005), p. 184102.

[57] X. T. Lou, G. Somesfalean, F. Xu, Y. G. Zhang and Z. G. Zhang. "Gas sensing by tunable multimode diode laser using correlation spectroscopy". *Applied Physics B: Lasers and Optics* 93.2-3 (Sept. 2008), pp. 671–676. DOI: 10.1007/s00340-008-3167-3.

[58] X. T. Lou, G Somesfalean, B Chen, Y. G. Zhang, H. S. Wang, Z. G. Zhang, S. H. Wu and Y. K. Qin. "Simultaneous detection of multiple-gas species by correlation spectroscopy using a multimode diode laser". *Optics letters* 35.11 (2010), pp. 1749–1751.

[59] G. Gao, B. Chen and B. Hu. "Carbon Dioxide Measurement Based on Multimode Diode Laser Correlation Spectroscopy Employing Wavelength Modulation Techniques". *Spectroscopy Letters* July (Feb. 2013), p. 130227105156005. DOI: 10.1080/00387010.2013.775462.

[60] S. A. Diddams, L. Hollberg and V. Mbele. "Molecular fingerprinting with the resolved modes of a femtosecond laser frequency comb." *Nature* 445.7128 (Feb. 2007), pp. 627–30. DOI: 10.1038/nature05524.

[61] C. Gohle, B. Stein, A. Schliesser, T. Udem and T. W. Hänsch. "Cavity-enhanced optical frequency comb vernier spectroscopy: application to human breath analysis". 16.4 (June 2007), pp. 6–15.

[62] A. Castrillo, A. Gambetta, D. Gatti, G. Galzerano, P. Laporta, M. Marangoni and L. Gianfrani. "Absolute molecular density determinations by direct referencing of a quantum cascade laser to an optical frequency comb". *Applied Physics B* 110.2 (May 2012), pp. 155–162. DOI: 10.1007/s00340-012-5013-x.

[63] B. Bernhardt, A. Ozawa, P. Jacquet, M. Jacquey, Y. Kobayashi, N. Picque, T. Udem, R. Holzwarth, G. Guelachvili and T. W. Ha. "Cavity-enhanced dual-comb spectroscopy". *Nature Photonics* 4.November 2009 (2010), pp. 2009–2011. DOI: 10.1038/NPHOTON.2009.217.

[64] A. Foltynowicz, T. Ban, P. Masowski, F. Adler and J. Ye. "Quantum-Noise-Limited Optical Frequency Comb Spectroscopy". *Physical Review Letters* 107.23 (Nov. 2011), p. 233002. DOI: 10.1103/PhysRevLett.107.233002.

[65] A. Foltynowicz, P. Masowski, A. J. Fleisher, B. J. Bjork and J. Ye. "Cavity-enhanced optical frequency comb spectroscopy in the mid-infrared application to trace detection of hydrogen peroxide". *Applied Physics B* 110.2 (May 2012), pp. 163–175. DOI: 10.1007/s00340-012-5024-7.

[66] J. Ye and S. T. Cundiff. *Femtosecond optical frequency comb: Principle, Operation and Applications*. Norwell, MA: Kluwer Academic Publishers / Springer, 2005.

[67] W. Oskay, S. A. Diddams, E. Donley, T. Fortier, T. Heavner, L. Hollberg, W. Itano, S. Jefferts, M. Delaney, K. Kim, F. Levi, T. Parker and J. Bergquist.

"Single-Atom Optical Clock with High Accuracy". *Physical Review Letters* 97.2 (July 2006), p. 020801. DOI: 10.1103/PhysRevLett.97.020801.

[68] H. S. Margolis. "Spectroscopic applications of femtosecond optical frequency combs." *Chemical Society reviews* 41.15 (Aug. 2012), pp. 5174–84. DOI: 10.1039/c2cs35163c.

[69] T. Udem, R Holzwarth and T. W. Hänsch. "Optical frequency metrology." *Nature* 416.6877 (Mar. 2002), pp. 233–7. DOI: 10.1038/416233a.

[70] A. Huber, T. Udem, B. Gross, J. Reichert, M. Kourogi, K. Pachucki, M. Weitz and T. W. Hänsch. "Hydrogen-Deuterium 1S-2S Isotope Shift and the Structure of the Deuteron". *Physical Review Letters* 80.3 (Jan. 1998), pp. 468–471. DOI: 10.1103/PhysRevLett.80.468.

[71] M. J. Cich, C. P. McRaven, G. V. Lopez, T. J. Sears, D. Hurtmans and A. W. Mantz. "Temperature-dependent pressure broadened line shape measurements in the $\nu_1 + \nu_3$ band of acetylene using a diode laser referenced to a frequency comb". *Applied Physics B* 109 (Nov. 2011), pp. 373–384. DOI: 10.1007/s00340-011-4829-0.

[72] T. Gherman and D. Romanini. "Mode-locked cavity-enhanced absorption spectroscopy". *Optics Express* 10.19 (2002), pp. 1033–1042. DOI: 10.1364/OE.10.001033.

[73] C. Gohle, B. Stein, A. Schliesser, T. Udem and T. Hänsch. "Frequency Comb Vernier Spectroscopy for Broadband, High-Resolution, High-Sensitivity Absorption and Dispersion Spectra". *Physical Review Letters* 99.26 (Dec. 2007), p. 263902. DOI: 10.1103/PhysRevLett.99.263902.

[74] A. Foltynowicz, P. Masowski, T. Ban, F. Adler, K. C. Cossel, T. C. Briles and J. Ye. "Optical frequency comb spectroscopy". *Faraday Discussions* 150 (2011), p. 23. DOI: 10.1039/c1fd00005e.

[75] A. Schliesser, M. Brehm, F. Keilmann and D. van der Weide. "Frequency-comb infrared spectrometer for rapid, remote chemical sensing." *Optics express* 13.22 (Oct. 2005), pp. 9029–38.

[76] L. S. Rothman, I. E. Gordon, A. Barbe, D. C. Benner, P. F. Bernath, M Birk, V Boudon, L. R. Brown, A. Campargue, J.-P. Champion, K Chance, L. H. Coudert, V Dana, V. M. Devi, S Fally, J.-M. Flaud, R. R. Gamache, A. Goldman, D Jacquemart, I Kleiner, N Lacome, W. J. Lafferty, J.-Y. Mandin, S. T. Massie, S. N. Mikhailenko, C. E. Miller, N Moazzen-Ahmadi, O. V. Naumenko, A. Nikitin, J Orphal, V. I. Perevalov, A. Perrin, A. Predoi-Cross, C. P. Rinsland, M Rotger, M Šimečková, M. Smith, K Sung, S. Tashkun, J Tennyson, R. Toth, A. Vandaele and J Vander Auwera. "The HITRAN 2008 molecular spectroscopic database". *Journal of Quantitative Spectroscopy and Radiative Transfer* 110.9-10 (June 2009), pp. 533–572. DOI: 10.1016/j.jqsrt.2009.02.013.

[77] L. Rothman, I. Gordon, R. Barber, H. Dothe, R. Gamache, A. Goldman, V. Perevalov, S. Tashkun and J. Tennyson. "HITEMP, the high-temperature molecular spectroscopic database". *Journal of Quantitative Spectroscopy and Radiative Transfer* 111.15 (Oct. 2010), pp. 2139–2150. DOI: 10.1016/j.jqsrt.2010.05.001.

[78] E. Whiting. "An empirical approximation to the Voigt profile". *Journal of Quantitative Spectroscopy and Radiative Transfer* (Aug. 1968).

[79] J. Olivero and R. Longbothum. "Empirical fits to the Voigt line width: A brief review". *Journal of Quantitative Spectroscopy and Radiative Transfer* 17 (1977), pp. 233–236.

[80] D. Goldberg. "What every computer scientist should know about floating-point arithmetic". *ACM Computing Surveys (CSUR)* 23.1 (1991).

[81] R. N. Bracewell. *The Fourier Transform and Its Applications*. 2nd. McGraw-Hill New York, 1986.

[82] P Laporta, S Longhi and S Taccheo. "10 kHz-linewidth diode-pumped Er: Yb: glass laser". *Electronics Letters* 22 (1992), pp. 2067–2069.

[83] S. Taccheo, P. Laporta and C. Svelto. "Widely tunable single-frequency erbium-ytterbium phosphate glass laser". *Applied Physics Letters* 68.19 (1996), p. 2621. DOI: 10.1063/1.116201.

[84] G. Sacchi, G. Chiaretti, S. Cecchi, G. Randone, P. Laporta, S. Taccheo, F. Salina and O. Svelto. "Transmission Capabilities of a novel multi-wavelength erbium-ytterbium glass laser source". *Photonics Technology Letters, IEEE* 16.1 (Dec. 1862), pp. 233–263. DOI: 10.1007/BF02727017.

[85] S. Yamashita, K. Hsu and W. Loh. "Miniature erbium:ytterbium fiber Fabry-Perot multiwavelength lasers". *IEEE Journal of Selected Topics in Quantum Electronics* 3.4 (1997), pp. 1058–1064. DOI: 10.1109/2944.649540.

[86] W. Miniscalco. *Rare-Earth-Doped Fiber Lasers and Amplifiers, Revised and Expanded*. Ed. by M. J. Digonnet. New York: Marcel Dekker, 1993.

[87] S Taccheo, P Laporta, S Longhi, O Svelto and C Svelto. "Diode-pumped bulk erbium-ytterbium lasers". *Applied Physics B: Lasers and Optics* 436 (1996), pp. 425–436.

[88] P Laporta, S De Silvestri, V Magni and O Svelto. "Diode-pumped cw bulk Er:Yb:glass laser." *Optics letters* 16.24 (Dec. 1991), pp. 1952–4.

[89] A.E. Siegman. *Lasers*. Sausalito, California: University Science Books, 1986.

[90] F. Song, G. Zhang, M. Shang, H. Tan, J. Yang and F. Meng. "Three-photon phenomena in the upconversion luminescence of erbium-ytterbium-codoped phosphate glass". *Applied Physics Letters* 79.12 (2001), p. 1748. DOI: 10.1063/1.1404996.

[91] O. Svelto. *Principles of lasers*. Springer, 2010.

[92] P Laporta, S Taccheo, S Longhi, O Svelto and C Svelto. "Erbium-ytterbium microlasers: optical properties and lasing characteristics". *Optical Materials* 11.January (1999).

[93] J Myczak, K Kopczyski and Z Mierczyk. "Wavelength tuning in Er , Yb : glass microchip lasers". *Opto-Electronics Review* 17.1 (2009), pp. 84–88. DOI: 10.2478/s11772.

[94] G. C. Valley. "Modeling Cladding-Pumped Er/Yb Fiber Amplifiers". *Optical Fiber Technology* 7.1 (Jan. 2001), pp. 21–44. DOI: 10.1006/ofte.2000.0351.

[95] A. Thompson, H. Northern, B. Williams, M. Hamilton, P. Ewart and J. H. Northern. "Simultaneous detection of CO and $CO_2$ in engine exhaust using multi-mode absorption spectroscopy". *Sensors and Actuators B* (2013). DOI: 10.1016/j.snb.2014.03.060.

[96] W. Braker, A. L. Mossman and C. L. Yaws. *Matheson gas data book*. Matheson East Rutherford, NJ, 1980.

[97] A. Ernst and J. D. Zibrak. "Carbon monoxide poisoning". *New England journal of medicine* 339.22 (1998), pp. 1603–1608.

[98] D. Williams. "The influence of nitrogen oxides on the atmospheric ozone content". *Quarterly Journal of the Royal Meteorological Society* 96.408 (1970), pp. 320–325.

[99] A. R. Ravishankara, J. S. Daniel and R. W. Portmann. "Nitrous oxide ($N_2O$): the dominant ozone-depleting substance emitted in the 21st century." *Science (New York, N.Y.)* 326.5949 (Oct. 2009), pp. 123–5. DOI: 10.1126/science.1176985.

[100] D. J. Wuebbles. "Atmosphere. Nitrous oxide: no laughing matter." *Science (New York, N.Y.)* 326.5949 (Oct. 2009), pp. 56–7. DOI: 10.1126/science.1179571.

[101] E. D. Schulze, S. Luyssaert, P. Ciais, A. Freibauer, I. A. Janssens et al., J. F. Soussana, P. Smith, J. Grace, I. Levin, B. Thiruchittampalam, M. Heimann, A. J. Dolman, R. Valentini, P. Bousquet, P. Peylin, W. Peters, C. Rödenbeck, G. Etiope, N. Vuichard, M. Wattenbach, G. J. Nabuurs, Z. Poussi, J. Nieschulze and J. H. Gash. "Importance of methane and nitrous oxide for Europe's terrestrial greenhouse-gas balance". *Nature Geoscience* 2.12 (Nov. 2009), pp. 842–850. DOI: 10.1038/ngeo686.

[102] W. Press, B. Flannery, S. Teukolsky and W. Vetterling. "Numerical recipes in C: the art of scientific programming". *Section* 10 (1992), pp. 408–412.

[103] F. K. F. Tittel, D. Richter and A. Fried. "Mid-infrared laser applications in spectroscopy". In: *Solid-State Mid-Infrared Laser Sources*. Vol. 516. 7. Springer, 2003, pp. 445–516. DOI: 10.1007/3-540-36491-9_11.

[104] A. Godard. "Infrared (2 — 12 $\mu$m) solid-state laser sources : a review". *Comptes Rendus Physique* 8 (2007), pp. 1100–1128. DOI: 10.1016/j.crhy.2007.09.010.

[105] W Chen, J Cousin, E Poullet, J Burie, D Boucher, X Gao, M Sigrist and F Tittel. "Continuous-wave mid-infrared laser sources based on difference frequency generation". *Comptes Rendus Physique* 8.10 (Dec. 2007), pp. 1129–1150. DOI: 10.1016/j.crhy.2007.09.011.

[106] C Roller, K Namjou, J Jeffers, W Potter, P. J. McCann and J Grego. "Simultaneous NO and $CO_2$ measurement in human breath with a single IV-VI mid-infrared laser." *Optics letters* 27.2 (Jan. 2002), pp. 107–9.

[107] J. Faist, F. Capasso, D. Sivco and C. Sirtori. "Quantum cascade laser". *Science* 1990 (1994), pp. 1–4.

[108] A. Kosterev, G. Wysocki, Y. Bakhirkin, S. So, R. Lewicki, M. Fraser, F. Tittel and R. Curl. "Application of quantum cascade lasers to trace gas analysis". *Applied Physics B* 90.2 (Dec. 2007), pp. 165–176. DOI: 10.1007/s00340-007-2846-9.

[109] R. F. Curl, F. Capasso, C. Gmachl, A. A. Kosterev, B. McManus, R. Lewicki, M. Pusharsky, G. Wysocki and F. K. Tittel. "Quantum cascade lasers in chemical physics". *Chemical Physics Letters* 487.1-3 (Feb. 2010), pp. 1–18. DOI: 10.1016/j.cplett.2009.12.073.

[110] Y. Yao, A. Hoffman and C. Gmachl. "Mid-infrared quantum cascade lasers". *Nature Photonics* 6.June (2012). DOI: 10.1038/NPHOTON.2012.143.

[111] M. Beck, D. Hofstetter, T. Aellen, J. Faist, U. Oesterle, M. Ilegems, E. Gini and H. Melchior. "Continuous wave operation of a mid-infrared semiconductor laser at room temperature." *Science (New York, N.Y.)* 295.5553 (Jan. 2002), pp. 301–5. DOI: 10.1126/science.1066408.

[112] L Hvozdara, N Pennington, M Kraft, M Karlowatz and B Mizaikoff. "Quantum cascade lasers for mid-infrared spectroscopy". *Vibrational Spectroscopy* 30 (2002), pp. 53–58.

[113] L. Dong, R. Lewicki, K. Liu, P. R. Buerki, M. J. Weida and F. K. Tittel. "Ultra-sensitive carbon monoxide detection by using EC-QCL based quartz-enhanced photoacoustic spectroscopy". *Applied Physics B* 107.2 (Mar. 2012), pp. 275–283. DOI: 10.1007/s00340-012-4949-1.

[114] M. Mazurenka, R. Wada, A. Shillings, T. Butler, J. Beames and A. Orr-Ewing. "Fast Fourier transform analysis in cavity ring-down spectroscopy: application to an optical detector for atmospheric $NO_2$". *Applied Physics B* 81.1 (May 2005), pp. 135–141. DOI: 10.1007/s00340-005-1834-1.

[115] X. Chao, J. B. Jeffries and R. K. Hanson. "Wavelength-modulation-spectroscopy for real-time, in situ NO detection in combustion gases with a 5.2 $\mu$m quantum-cascade laser". *Applied Physics B* 106.4 (Nov. 2011), pp. 987–997. DOI: 10.1007/s00340-011-4839-y.

[116] S. M. Cristescu, D. Marchenko, J. Mandon, K. Hebelstrup, G. W. Griffith, L. A. J. Mur and F. J. M. Harren. "Spectroscopic monitoring of NO traces in plants and human breath: applications and perspectives". *Applied Physics B* (May 2012). DOI: 10.1007/s00340-012-5050-5.

[117] W. Ren, A. Farooq, D. F. Davidson and R. K. Hanson. "CO concentration and temperature sensor for combustion gases using quantum-cascade laser absorption near 4.7 $\mu$m". *Applied Physics B* 107.3 (May 2012), pp. 849–860. DOI: 10.1007/s00340-012-5046-1.

[118] J. Vanderover, W. Wang and M. A. Oehlschlaeger. "A carbon monoxide and thermometry sensor based on mid-IR quantum-cascade laser wavelength-modulation absorption spectroscopy". *Applied Physics B* 103.4 (May 2011), pp. 959–966. DOI: 10.1007/s00340-011-4570-8.

[119] S. Welzel, F. Hempel, M. Hübner, N. Lang, P. B. Davies and J. Röpcke. "Quantum cascade laser absorption spectroscopy as a plasma diagnostic tool: an overview." *Sensors (Basel, Switzerland)* 10.7 (Jan. 2010), pp. 6861–900. DOI: 10.3390/s100706861.

[120] I Vurgaftman, W. W. Bewley, C. L. Canedy, C. S. Kim, M Kim, C. D. Merritt, J Abell, J. R. Lindle and J. R. Meyer. "Rebalancing of internally generated carriers for mid-infrared interband cascade lasers with very low power consumption." *Nature communications* 2 (Jan. 2011), p. 585. DOI: 10.1038/ncomms1595.

[121] W. Denzer, G. Hancock, A. Hutchinson, M. Munday, R. Peverall and G. A. D. Ritchie. "Mid-infrared generation and spectroscopy with a PPLN ridge waveguide". *Applied Physics B* 86.3 (Jan. 2007), pp. 437–441. DOI: 10.1007/s00340-006-2570-x.

[122] K. E. Whittaker, L. Ciaffoni, G. Hancock, R. Peverall and G. A. D. Ritchie. "A DFG-based cavity ring-down spectrometer for trace gas sensing in the mid-infrared". *Applied Physics B* (Sept. 2012), pp. 333–343. DOI: 10.1007/s00340-012-5150-2.

[123] M. L. Hamilton, R. Peverall, G. A. D. Ritchie, L. J. Thornton and J. H. Helden. "Wavelength modulation and cavity enhanced absorption spectroscopy using 1.9 $\mu$m radiation produced by difference frequency generation with a MgO doped PPLN crystal". *Applied Physics B* 97.3 (July 2009), pp. 715–722. DOI: 10.1007/s00340-009-3636-3.

[124] L. Ciaffoni, R Grilli, G Hancock, A. J Orr-Ewing, R Peverall and G. A. D. Ritchie. "3.5-$\mu$m high-resolution gas sensing employing a $LiNbO_3$ QPM-DFG waveguide module". *Applied Physics B* 94.3 (Nov. 2008), pp. 517–525. DOI: 10.1007/s00340-008-3291-0.

[125] D. Richter, A. Fried, B. P. Wert, J. G. Walega and F. K. Tittel. "Development of a tunable mid-IR difference frequency laser source for highly sensitive airborne trace gas detection". *Applied Physics B: Lasers and Optics* 75.2-3 (Sept. 2002), pp. 281–288. DOI: 10.1007/s00340-002-0948-y.

[126] J. J. Scherer, J. B. Paul, H. J. Jost and M. L. Fischer. "Mid-IR difference frequency laser-based sensors for ambient $CH_4$, CO, and $N_2O$ monitoring". *Applied Physics B* 110.2 (Nov. 2012), pp. 271–277. DOI: 10.1007/s00340-012-5244-x.

[127] M Asobe, O Tadanaga, T Yanagawa, T Umeki, Y Nishida and H Suzuki. "High-power mid-infrared wavelength generation using difference frequency generation in damage-resistant Zn:$LiNbO_3$ waveguide". *Electronics Letters* 44.4 (2008), pp. 3–5. DOI: 10.1049/el.

[128] D. Richter, P. Weibring, A. Fried, O. Tadanaga, Y. Nishida, M. Asobe, H. Suzuki and J. G. Walega. "High-power, tunable difference frequency generation source for absorption spectroscopy based on a ridge waveguide periodically poled lithium niobate crystal". *Optics Express* 15.2 (Jan. 2007), p. 564. DOI: 10.1364/OE.15.000564.

[129] R. Grilli, L. Ciaffoni and A. J. Orr-ewing. "mid-IR light from a difference frequency generation PPLN waveguide". *Optics Letters* 35.9 (2010), pp. 1383–1385.

[130] R. W. Boyd. *Nonlinear optics*. Academic press, 1992.

[131] M. Fejer, G. Magel, D. Jundt and R. Byer. "Quasi-phase-matched second harmonic generation: tuning and tolerances". *IEEE Journal of Quantum Electronics* 28.11 (1992), pp. 2631–2654. DOI: 10.1109/3.161322.

[132] H. H. Abu-Safe. "Difference frequency mixing of strongly focused Gaussian beams in periodically poled $LiNbO_3$". *Applied Physics Letters* 86.23 (2005), p. 231105. DOI: 10.1063/1.1947886.

[133] G. D. Boyd and D. Kleinman. "Parametric interaction of focused Gaussian light beams". *Journal of Applied Physics* 39.8 (1968), p. 3597. DOI: 10.1063/1.1656831.

[134] S. Borri, P. Cancio, P. De Natale, G. Giusfredi, D. Mazzotti and F. Tamassia. "Power-boosted difference-frequency source for high-resolution infrared spectroscopy". *Applied Physics B: Lasers and Optics* 76.4 (Apr. 2003), pp. 473–477. DOI: 10.1007/s00340-003-1133-7.

[135] M. Broyer and Tran-Ba-Chu. "Intracavity cw difference frequency generation by mixing three photons and using Gaussian laser beams". *J. Physique* 46 (1985), pp. 523–533.

[136] L. Ciaffoni. "Laser Spectroscopy for the Detection of Volatile Sulfur-containing Compounds in Breath". DPhil Thesis. University of Oxford, 2010.

[137] P. Weibring, D. Richter, A. Fried, J. Walega and C. Dyroff. "Ultra-high-precision mid-IR spectrometer II: system description and spectroscopic performance". *Applied Physics B* 85.2-3 (June 2006), pp. 207–218. DOI: 10.1007/s00340-006-2300-4.

[138] P. W. Werle, P Mazzinghi, F D'Amato, M De Rosa, K Maurer and F Slemr. "Signal processing and calibration procedures for in situ diode-laser absorption spectroscopy." *Spectrochimica acta. Part A, Molecular and biomolecular spectroscopy* 60.8-9 (July 2004), pp. 1685–705. DOI: 10.1016/j.saa.2003.10.013.